

Exchange-Coupled Ferri-/Ferromagnetic Composite Nanomagnets

DISSERTATION

submitted in partial fulfillment of the requirements for the degree of

Doktor der Technischen Wissenschaften

by

Ing. Harald Özelt, MSc.

Registration Number 1229247

to the Faculty of Physics
at the Vienna University of Technology

Advisor: Univ.-Doz. Dipl.-Ing. Dr.techn. Thomas Schrefl

The dissertation has been reviewed by:

Univ.-Doz. Dipl.-Ing. Dr. techn.
Thomas Schrefl

Prof. Dan A. Allwood, BSc PhD
MInstP CPhys

Ao.Univ.-Prof. Dipl.-Ing.
Dr.techn. Franz Keplinger

Vienna, 13th November, 2018

Ing. Harald Özelt, MSc.

Erklärung zur Verfassung der Arbeit

Ing. Harald Özelt, MSc.
Konvalinastraße 7 / RH 1, A-3202 Hofstetten

Hiermit erkläre ich, dass ich diese Arbeit selbständig verfasst habe, dass ich die verwendeten Quellen und Hilfsmittel vollständig angegeben habe und dass ich die Stellen der Arbeit – einschließlich Tabellen, Karten und Abbildungen –, die anderen Werken oder dem Internet im Wortlaut oder dem Sinn nach entnommen sind, auf jeden Fall unter Angabe der Quelle als Entlehnung kenntlich gemacht habe.

Wien, 13. November 2018

Harald Özelt

Kurzfassung

Seit der Einführung von magnetischen Festplatten wurde deren Speicherkapazität jedes Jahr drastisch erhöht. In den letzten Jahren stieß die Industrie jedoch an technologische Grenzen, die das jährliche Wachstum der Bitdichte verlangsamen. Mehrere Ansätze wurden vorgeschlagen, um die derzeitigen Beschränkungen zu umgehen. Gegenwärtig arbeitet die Industrie daran, wärmeunterstützte magnetische Aufzeichnung (heat assisted magnetic recording – HAMR) und mikrowellenunterstützte Aufzeichnung (microwave assisted magnetic recording – MAMR) auf den Markt zu bringen, die dem Wachstum der Bitdichte neuen Schub verleihen sollen. Eine darauf folgende Technologie wäre die Aufzeichnung auf bitstrukturierten Medien (bit patterned magnetic recording – BPMR), die mit den derzeit entwickelten Technologien kombiniert werden sollen. Ein aktuelles Problem ist die Reduzierung des magnetischen Volumens pro Bit bei gleichzeitiger Wahrung der thermischen Stabilität und Schreibbarkeit der Bits. Ein möglicher Ansatz dazu sind austauschgekoppelte Verbundmedien mit einem hartmagnetischen Material als thermisch stabile Speicherschicht und einer weichmagnetischen Schicht zur Verringerung des Schreibfeldes. Mögliche Kandidaten für die weiche Schicht sind ferrimagnetische Materialien, da sie abstimmbare magnetische Eigenschaften und eine ungewöhnliche Temperaturabhängigkeit der Magnetisierung aufweisen. Beide Eigenschaften können zur Optimierung des Mediums von Festplatten genutzt werden. In der vorliegenden Arbeit wird ein mikromagnetisches Modell von austauschgekoppelten ferri-/ferromagnetischen Doppelschichten für den Einsatz in bitstrukturierten Medien entwickelt und ausgewertet.

Zunächst wird ein Modell für ferrimagnetische Schichten beschrieben und implementiert. Das Modell wird dann durch den Vergleich von Simulationen mit experimentellen Ergebnissen angepasst. Durch die Einbeziehung von räumlichen Variationen der magnetokristallinen Anisotropie und der anisotropen Vorzugsachse konnten fünf Merkmale, die in experimentell gewonnenen remanenten Domänenstrukturen beobachtet wurden, reproduziert werden. Die Simulation eines $\text{Fe}_{81}\text{Gd}_{19}$ Films mit Vorzugsachse parallel zur Filmnormale zeigte eine Magnetisierungsumkehr durch eine Domänenwandbewegung Richtung Filmebene, die durch Pinningprozesse an räumlichen Inhomogenitäten bestimmt wird.

In einem nächsten Schritt wird das Modell um eine austauschgekoppelte ferroma-

gnetische Schicht erweitert. Die Werte der magnetischen Eigenschaften stammen aus Experimenten, bei denen die hartmagnetische Schicht ferrimagnetisches $\text{Fe}_{81}\text{Tb}_{19}$ ist und die weichmagnetische Schicht ein mehrlagiger $[\text{Co}/\text{Pt}]_{10}$ Film. Die Simulationsergebnisse für ferri-/ferromagnetische Doppelschichten zeigen einen großen Einfluss der Kopplungsstärke an der Grenzfläche zwischen den beiden Schichten auf die Magnetisierungsumkehr. Die Ergebnisse deuten darauf hin, dass im Experiment große Bereiche der Grenzfläche nur schwach gekoppelt sind ($< 1 \text{ mJ}/\text{m}^2$) und nur ein kleiner Teil eine stärkere Kopplung aufweist ($\sim 10 \text{ mJ}/\text{m}^2$). Die gekoppelte weiche Schicht reduziert das gesamte Schaltfeld, indem sie einen Nukleationskeim für die Ummagnetisierung bereitstellt. Mit zunehmendem externen Feld wird die Domänenwand gegen die Grenzfläche gedrückt, bis sie durchbricht und sich seitlich durch den Ferrimagneten bewegt. Die laterale Bewegung wird durch Domänenwandhaften bestimmt, das durch die räumlich inhomogene Verteilung der magnetokristallinen Anisotropiekonstante entsteht.

Schließlich wird das mikromagnetische Modell für ferri-/ferromagnetische Doppelschichten für die magnetischen Inseln in bitstrukturierten Medien angewendet. Die Speicherschicht wird durch $\text{Fe}_{52}\text{Pt}_{48}$ repräsentiert während ferrimagnetisches $\text{Fe}_{74}\text{Gd}_{26}$ als weiche Hilfsschicht wirkt. Kleine Inseldurchmesser zeigen höhere Schaltfelder und breitere Schaltfeldverteilungen. Dieser Effekt kann durch Erhöhung der Kopplungsstärke an der Grenzfläche der Doppelschicht und der Dicke der weichen Schicht reduziert werden. Weitere Berechnungen ergaben, dass durch Zugabe der ferrimagnetischen, weichen Schicht die Standardabweichung der dipolaren Wechselwirkungsfeldverteilung auf 9% des Schaltfeldes der Insel erhöht wird. Eine Berechnungsmethode für eine Medienbitfehlerrate wird vorgestellt. Diese kombiniert den Effekt der Schaltfeldverteilung, der dipolaren Wechselwirkungsfeldverteilung und des Schreibfeldwinkels in einen Parameter. Die gekoppelte ferrimagnetische Schicht senkt die Medienbitfehlerrate signifikant, obwohl mit zunehmender Dicke dieser Schicht das dipolare Feld dominanter wird. Um eine Medienbitfehlerrate von 10^{-6} aufrechtzuerhalten, wird das benötigte Schreibfeld bei einem Winkel von 40° um 7% reduziert, wenn eine 20 nm dicke ferrimagnetische Schicht gekoppelt wird.

Simulationen zeigen, dass während der Fabrikation unerwünscht abgelagertes Material an den Seitenwänden von Bitinseln das Schaltfeld deutlich reduzieren kann. Daher ist es wichtig, diese Ablagerungen bei der Herstellung von bitstrukturierten Medien zu kontrollieren. Das Volumen der Ablagerungen sollte minimiert und über das gesamte Medium so gleichmäßig wie möglich sein, um enge Schaltfeldverteilungen zu gewährleisten. Weitere Simulationen zeigen, dass raue Seitenwände nur vernachlässigbare Auswirkungen auf das Schaltfeld der Inseln haben. Der ungünstigste simulierte Fall einer Insel mit 20 nm Durchmesser und maximale Abweichung von $\pm 5 \text{ nm}$ vom idealen Radius, zeigte eine Standardabweichung von nur 1.7% des idealen Schaltfeldes.

Abstract

Since their introduction the storage capacity of magnetic hard disk drives has increased dramatically every year. However, in recent years the industry hit technological limits slowing down the annual growth of storage density. Several approaches have been suggested to circumvent limitations. The industry is working hard to bring heat assisted magnetic recording (HAMR) and microwave assisted recording (MAMR) to the market, providing a new boost to the areal density growth. One step further in the future is the employment of bit patterned media recording (BPMR) which is expected to be combined with currently developed technologies. The major goal is to decrease the magnetic volume per bit while maintaining thermal stability and writeability of the bits. One possible approach to this problem is exchange coupled composite media with a hard magnetic material as thermally stable storage layer and a soft magnetic layer to lower the writing field of the bits. Possible candidates for the soft layer are ferrimagnetic materials, since they provide tunable magnetic properties and an unusual temperature dependency of the magnetization. Both features could be exploited for optimizing the media of hard disk drives. In this thesis a micromagnetic model of exchange coupled ferri-/ferromagnetic bilayers for use in bit patterned media is developed and evaluated.

First a model for ferrimagnetic films is described and implemented. The model is then adjusted by comparing simulations with experimental results. By incorporating spatial variations of magnetocrystalline anisotropy and anisotropic easy axis, a number of five features observed in experimentally derived remanent domain patterns could be reproduced. The simulation of an $\text{Fe}_{81}\text{Gd}_{19}$ film with out-of-plane anisotropy revealed a magnetization reversal process by the lateral movement of domain walls, governed by pinning processes at spatial inhomogeneities.

Next the model is extended by an exchange coupled ferromagnetic layer. The magnetic properties are taken from experiments, where the hard magnetic layer is ferrimagnetic $\text{Fe}_{81}\text{Tb}_{19}$ and the soft magnetic layer is a $[\text{Co}/\text{Pt}]_{10}$ multilayer. The simulation results for ferri-/ferromagnetic bilayers attribute high importance to the coupling strength at the interface for controlling the magnetization reversal. The results indicate further, that in the experiment large areas were weakly coupled ($< 1 \text{ mJ}/\text{m}^2$) at the interface and only a small portion of the interface exhibits stronger

coupling ($\sim 10 \text{ mJ/m}^2$). The coupled soft layer reduces the overall switching field by providing a nucleation site for the domain wall. With increasing applied field the wall is pushed against the interface until it breaks through and moves laterally through the ferrimagnet. The lateral domain wall movement is governed by pinning, mainly due to spatial changes of the magnetocrystalline anisotropy constant.

The micromagnetic model for ferri-/ferromagnetic bilayers is applied to dots in bit patterned media. The storage layer is represented by $\text{Fe}_{52}\text{Pt}_{48}$ and a ferrimagnetic $\text{Fe}_{74}\text{Gd}_{26}$ acts as soft assisting layer. Smaller bilayer dot diameters show higher switching fields and broader switching field distributions. Both effects can be reduced by increasing the coupling strength at the bilayer's interface and the thickness of the soft layer. Further calculations revealed that by adding the ferrimagnetic soft layer the standard deviation of the dipolar interaction field distribution is increased to 9% of the dot's switching field. A calculation of a medium bit error rate is proposed to combine the effect of switching field distribution, dipolar interaction field distribution and write field angle into a characterizing parameter. Adding the exchange coupled ferrimagnetic layer significantly lowers the media bit error rate, even though with increasing thickness of the ferrimagnetic layer the dipolar interaction field becomes more dominant. While maintaining a media bit error rate of $< 10^{-6}$, the inclusion of a 20 nm thick ferrimagnet reduces the write head field requirement by 7% (with a field angle of 40°).

Simulations reveal that redeposited material at the sidewalls of bit patterned media dots can significantly reduce the switching field of the dots. It is therefore important to control the redeposition during fabrication of bit patterned media by minimizing the volume of redeposited material and make it as uniform as possible across the media to maintain narrow switching field distributions. Further simulations of dots with rough sidewalls show negligible effects on the switching field. The worst simulated case of a dot with 20 nm diameter and maximal deviation of $\pm 5 \text{ nm}$ from the ideal radius showed a standard deviation of only 1.7% of its ideal switching field.

Acknowledgements

Firstly, I want to thank Thomas Schrefl for his guidance, support, motivation, inspiration and for being the great, kind, positive person he is. I am very lucky to call him my boss.

Of course, I also want to thank my colleagues and friends who were there to provide me with motivation and feedback. We had long discussions, cosy barbecues, frequent celebrations, fun weekend trips, beautiful hiking and climbing tours, exhausting skiing trips and generally a good time at the office and at conferences. Thank you, Alexander Kovacs, Markus Gusenbauer, Johann Fischbacher, Simon Bance, Franz Reichel, Lukas Exl, Dieter Süß, Christoph Vogler, Claas Abert, Florian Bruckner, Roman Windl, Christian Huber, Gino Hrkac, Hossein Sepehri-Amin, Hubert Brückl, Thomas Glatzl, Felix Ring, Aleksey Bratukhin, Astrit Shoshi, Herbert Weitensfelder, Kazuya Yokota, Elisabeth Schiefer and Ulrike Lachner.

I would also like to thank the people who have been involved in the project from which this thesis is mainly derived. I thank Manfred Albrecht, Laura Heyderman, Christian Schubert, Birgit Hebler, Phillip Wohlhüter, Eugenie Kirk, Dennis Nissen and Patrick Matthes for great discussions and important feedback and support.

I especially want to thank my wife Rosi and my two girls Hannah and Emma for their patience and love. I thank my friends Martin & Elisabeth and Jens & Elisabeth for continuous beer evenings, extensive discussions, fun weekend trips and very welcome distractions from work in my spare time. I also want to thank my parents Gabi & Karl for their continuous support and providing a quiet space to write this thesis.

I gratefully acknowledge the financial support provided by the Austrian Science Fund (FWF): I821 and by the German Research Foundation (DFG-Grant No. AL 618/17-1) and the Swiss National Science Foundation (SNF Grant No. 200021L_137509) and the Vienna Science and Technology Fund (WWTF Grant No. MA14-044).

In my work I used the following open source and free tools: Paraview [108], Salomé [124], Neper [114], Python [113], Gmsh [39], Gnuplot [157], Inkscape [57], GIMP [43], Octave [29] and $\text{\LaTeX}2_{\epsilon}$ with Texmaker [145].

Contents

1	Introduction	1
1.1	Motivation	1
1.2	Structure of the work	2
2	Theoretical background	4
2.1	Magnetic materials	5
2.1.1	Magnetic moment	5
2.1.2	Ferromagnetism	7
2.1.3	Ferrimagnetism	10
2.1.4	Exchange coupled composites.....	11
2.2	Micromagnetism.....	12
2.2.1	Static micromagnetism	14
2.2.2	Dynamic micromagnetism	19
2.2.3	Finite element calculations	20
2.2.4	Mesh size.....	21
2.3	Magnetization reversal	23
2.3.1	Hysteresis loop	23
2.3.2	The Stoner-Wohlfarth model	24
2.3.3	Magnetic domains and reversal modes.....	26
2.3.4	Domain walls and domain wall pinning.....	29
2.4	Magnetic recording.....	31
2.4.1	Trilemma of magnetic recording	32
2.4.2	Future recording technologies	33
3	Ferrimagnetic films	34
3.1	Micromagnetism for ferrimagnetic thin films	35
3.2	Properties of ferrimagnetic films	37
3.2.1	Fresnel imaging of domain patterns	38
3.2.2	Model for ferrimagnetic films	39
3.2.3	Validation of the ferrimagnetic model	41
3.3	Magnetization reversal and domain wall motion.....	48

3.4	Summary	50
4	Ferri-/ferromagnetic heterostructures	52
4.1	Model for exchange coupled composites.....	53
4.2	Magnetization reversal	56
4.3	Domain wall motion	59
4.3.1	Domain wall pinning.....	60
4.4	Summary	62
5	Exchange coupled bilayers in bit patterned media	64
5.1	Model for ferri-/ferromagnetic bilayer dots.....	66
5.2	Magnetization reversal of bilayer dots	68
5.2.1	Effect of dot diameter	69
5.2.2	Effect of exchange coupling strength at the interface	71
5.2.3	Effect of ferrimagnetic layer thickness.....	75
5.3	Switching field distribution.....	80
5.3.1	Intrinsic switching field distribution.....	82
5.3.2	Dipolar interaction field in bit patterned media	85
5.3.3	Bit error rate of bilayer dot arrays	90
5.4	Further characterization of dots in bit patterned media	97
5.4.1	Switching field reduction by redeposition	97
5.4.2	Effect of dot edge roughness	99
5.5	Read back field of bilayer dots	102
5.6	Summary	104
6	Conclusion and Outlook	107
6.1	Conclusion.....	107
6.2	Outlook.....	108
	List of Figures	109
	List of Tables	111
	List of Symbols	112
	Bibliography	119

Introduction

Contents

1.1	Motivation	1
1.2	Structure of the work	2

1.1 Motivation

While the magnetic recording industry is focusing mainly on two approaches for the next generation of hard disk drives, namely heat assisted magnetic recording (HAMR) and microwave assisted magnetic recording (MAMR), it is vital to already explore possible approaches for what comes afterwards. One technology expected to be feasible to employ within the next 5 to 10 years [7] is bit patterned magnetic recording (BPMR). Although many obstacles remain to bring BPMR to market, huge progress has been made in fabrication schemes in recent years [4]. The BPMR technology is expected to be combined with other new technologies, especially HAMR which is sometimes called heated dot magnetic recording (HDMR). Initial theoretical work for HDMR, promising high areal densities, has already been done [153, 98].

These technologies attempt to address the current limitations, also called the trilemma of magnetic recording. The main goal is to maintain thermal stability of the written bits while preserving the writeability when increasing the areal density. The use of exchange coupled composites (ECC) is one more approach to overcome the current limits and can also be combined with HAMR and HDMR. In ECC materials the thermal stability is provided by the hard magnetic storage layer, while a coupled soft layer lowers the required field to write the bits [141]. Promising candidates for the soft magnetic layer can be found in the group of ferrimagnetic materials. The media design

could heavily benefit from ferrimagnets since their magnetic properties can be tuned by their composition [93]. Moreover, the exceptional dependency of magnetization on the temperature in ferrimagnets could be utilized. At a certain temperature, called the compensation point, a ferrimagnet might show no magnetization, while with increased temperature a magnetization can be measured. This behavior could be used to stabilize bits at room temperature and help the writing process at increased temperature. Compared to HAMR much lower temperatures might be needed.

The aim of this thesis is to establish and validate a micromagnetic model for ferrimagnetic materials and extend the model to incorporate an exchange coupled second layer. With this model the use of ferri-/ferromagnetic exchange coupled dots in BPMR shall be investigated by simulations. The focus here lies on the switching mechanisms of the bilayer dots and the switching field distribution of entire dot arrays. The simulations are done simultaneously alongside experimental work by project partners. The results are regularly shared between the project partners to validate simulations and explain experimental results.

1.2 Structure of the work

Chapter 2 comprises a brief overview of the theory of magnetism and magnetic materials used in this work. The basic concept and energy terms used in finite element micromagnetic simulations are described. The behavior of a magnetic material can be characterized by its magnetization reversal, hence the chapter deals with theoretical models for hysteresis, magnetic domains and domain walls. The last section of the overview chapter gives some background of magnetic recording and describes the trilemma of magnetic recording.

Chapter 3 introduces the micromagnetic model for ferrimagnetic films and shows the comparison of simulation results with experimentally gained remanent domain patterns of ferrimagnetic squares. Then the magnetization reversal and domain wall movement in ferrimagnetic layers are simulated and discussed.

The next step in Chapter 4 is to add an exchange coupled ferromagnetic film. Hence, the micromagnetic model is expanded to incorporate the exchange energy at the interface of the bilayer. The magnetization reversal and domain wall movement within the bilayer structure is explored by simulation and discussed by comparing the results to experimental findings.

In Chapter 5 the model for ferri-/ferromagnetic bilayers is applied to investigate dots in bit patterned media for magnetic recording. First the magnetization reversal of single bilayer dots is explored for different dot diameters, interface coupling strength and layer thickness. Then the switching field distribution and dipolar interaction field of dot arrays are computed. A media bit error rate is defined incorporating the switching field distribution, dipolar interaction field distribution and writing field

angle to characterize the bilayer dot media. Experimental results by project partners raised concerns about the edge roughness of fabricated dots and redeposited material on the dot's sidewalls. The effect of both unintended by-products are inspected by simulations.

Finally, Chapter 6 gives a concluding summary of the findings in this thesis and an outlook of possible next steps.

Theoretical background

Contents

2.1	Magnetic materials	5
2.1.1	Magnetic moment	5
2.1.2	Ferromagnetism	7
2.1.3	Ferrimagnetism	10
2.1.4	Exchange coupled composites	11
2.2	Micromagnetism	12
2.2.1	Static micromagnetism	14
2.2.2	Dynamic micromagnetism	19
2.2.3	Finite element calculations	20
2.2.4	Mesh size	21
2.3	Magnetization reversal	23
2.3.1	Hysteresis loop	23
2.3.2	The Stoner-Wohlfarth model	24
2.3.3	Magnetic domains and reversal modes	26
2.3.4	Domain walls and domain wall pinning	29
2.4	Magnetic recording	31
2.4.1	Trilemma of magnetic recording	32
2.4.2	Future recording technologies	33

This chapter is meant to give a brief overview of the theory of magnetism on which the work described in later chapters relies. It starts with the description of the magnetic moment and introduces ferro- and ferrimagnetism as well as the exchange coupling of magnetic materials in Section 2.1. In Section 2.2 the theory of micromagnetism and its numerical treatment are described. The investigation of a magnet and its properties is best done by observing its magnetization reversal, which is treated in Section 2.3. Finally a possible application for ferri-/ferromagnetic composite magnets is their use as media in magnetic recording, therefore a brief discussion on this topic is given in Section 2.4.

2.1 Magnetic materials

The phenomenon of magnetism has been observed and researched for almost three millennia and is still an important major topic in ongoing research [90, pp. 49–52]. Investigations on magnetic materials are driven by the requirements of applications in many key areas of modern technology, such as permanent magnets for motors and generators, magnetic sensors and magnetic storage media (hard disks). The basic quantity of magnetism is the magnetic moment.

2.1.1 Magnetic moment

As stated by the Bohr-van Leeuwen-theorem, if a system of electrons is treated purely by classical statistics, the magnetization of the system would always be zero [2, pp. 6–8]. The classical approach doesn't allow change in kinetic energy of electrons in a magnetic field. Magnetism is a quantum mechanical effect and therefore can not be described in a purely classical way. Still, many phenomena can be treated by semi-classical approaches. For example, diamagnetic and paramagnetic properties were described by a semi-classical approach by Langevin already in 1905.

The source of magnetism is found to be magnetic moments of elementary particles. The magnetic moment of electrons is tightly connected to its angular momentum, as demonstrated by the Einstein-de Haas effect [30]. Therefore the magnetic moment can be described by calculating the angular momentum of an electron. There are two contributions to this momentum: a) the orbital moment \mathbf{l} of an electron orbiting the nucleus in an atom, and b) the intrinsic spin moment \mathbf{s} of an electron [16, pp. 63–66]. Each of the angular moments results in a corresponding magnetic moment

$$\mathbf{m}_l = -\frac{e}{2m_e} \mathbf{l}, \quad (2.1)$$

$$\mathbf{m}_s = -\frac{e}{m_e} \mathbf{s}. \quad (2.2)$$

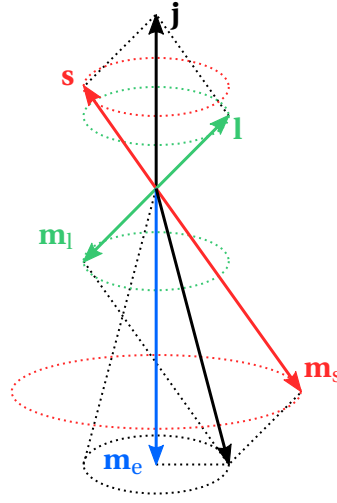


Figure 2.1: Sketch of angular moments and the coupled magnetic moments of an electron.

Here, e and m_e are the charge and the mass of an electron, respectively. It can be seen that the proportionality factor between the magnetic and angular moments are not equal. The impact of the spin moment on the magnetic moment is twice as big as that of the orbital moment. This magneto-mechanical anomaly implies, that the total magnetic moment of an electron $\mathbf{m}_l + \mathbf{m}_s$ has not the same direction as its total angular momentum $\mathbf{j} = \mathbf{l} + \mathbf{s}$. The magnetic moment of an electron \mathbf{m}_e is determined only by the component (anti-)parallel to \mathbf{j} (see Figure 2.1).

Within an atom or ion the angular moments of all the electrons are coupled by spin-orbit interactions depending on the proton number. Only unpaired spins in unfilled shells of the atom will contribute to a total angular moment. The relation between the magnitude of the total angular moment \mathbf{J} and the magnetic dipole moment \mathbf{m}_{tot} is described by the Landé factor g_L [16, p. 65].

$$\|\mathbf{m}_{\text{tot}}\| = \frac{g_L \mu_B \|\mathbf{J}\|}{\hbar} \quad (2.3)$$

with

$$\mu_B = e\hbar/(2m_e) \approx 9.274 \times 10^{-24} \text{ Am}^2 \quad (2.4)$$

being the Bohr magneton and

$$\hbar \approx 1.055 \times 10^{-34} \text{ Js} \quad (2.5)$$

being the reduced Planck constant. It turns out, that often the orbital moment is negligibly small and therefore it is sufficient to use only the total spin moment [2,

p. 35], especially for 3d elements. In this case the Landé factor $g_L = 2$ and

$$\mathbf{m}_{\text{tot}} = g_L \mu_B \mathbf{s} \quad (2.6)$$

Alternatively, the gyromagnetic ratio γ of an electron is used to describe the relation between the angular momentum and the magnetic moment

$$\mathbf{m}_{\text{tot}} = \gamma \mathbf{J} \quad (2.7)$$

with

$$|\gamma| = \frac{|e|}{m_e} = 1.76086 \times 10^{11} \text{ rad/(sT)}. \quad (2.8)$$

Usually the magnetization of a solid body is treated per volume, therefore it is calculated by

$$\mathbf{M} = N \mathbf{m}_{\text{tot}}, \quad (2.9)$$

with N being the number of atoms per unit volume. In vacuum there is no magnetization and the magnetic flux density \mathbf{B} is proportional to the magnetic field strength \mathbf{H}

$$\mathbf{B} = \mu_0 \mathbf{H}, \quad (2.10)$$

via the vacuum permeability $\mu_0 = 4\pi \times 10^{-7} \text{ Vs/(Am)}$. In the presence of a magnetic material its magnetization alters the magnetic flux density

$$\mathbf{B} = \mu_0 (\mathbf{H} + \mathbf{M}). \quad (2.11)$$

If all magnetic moments are aligned the material has reached its maximal magnetization, also called spontaneous magnetization M_s . Usually, in terms of units, it is more convenient to work with the saturation polarization

$$J_s = \mu_0 M_s, \quad (2.12)$$

which has also μ_0 as proportionality factor.

2.1.2 Ferromagnetism

Magnetic materials are often roughly categorized by the magnetic response to an applied external magnetic field H_{ext} [12, p.5, pp. 19–23]. The response function is called the magnetic susceptibility χ . For linear materials

$$\chi = \frac{M}{H_{\text{ext}}}. \quad (2.13)$$

Here the magnetization M is the magnitude in the direction of the applied field. Even if generally the response is not linear, χ is often used to distinguish between diamagnetism ($\chi < 0$), para- and antiferromagnetism ($\chi > 0$) and ferro- and ferrimagnetism ($\chi \gg 0$). This means, when an external magnetic field is applied, diamagnetic materials create a weak opposing magnetic moment, in para- and antiferromagnetic materials weak aligned magnetization is induced and ferro- and ferrimagnetic materials show a strong aligned field. Moreover, when no external field is applied, only ferro- and ferrimagnetic materials can show a remanent magnetization M_r .

Below the so-called Curie temperature ferromagnetic materials show spontaneous magnetization due to an intrinsic alignment of the magnetic moments. Above the Curie temperature the order of the moments collapses and the material becomes paramagnetic.

Exchange interaction

In order to explain the spontaneous ordering of the magnetic moments, magnetic dipole interactions between the magnetic moments are far too weak. The underlying forces are exchange interactions, which again have their root in quantum mechanics. The exchange interaction is a consequence of electrostatic repulsion (Coulomb's law) and the Pauli exclusion principle [16, p. 135]. To reach an electrostatic energy minimum in ferromagnetic materials it is more favorable to align neighboring magnetic moments parallel. Therefore an overall spontaneous magnetization is observed without an external field.

In other cases an anti-parallel alignment is the most energy-efficient order. For this scenario the magnetic moments cancel each other out, hence showing no macroscopic spontaneous magnetization. Such materials are categorized as antiferromagnets and play an important role in sensor applications like GMR (giant magnetoresistance) devices and MRAM (magnetoresistive random-access memory) or HDD (hard disk drives) [65, 45].

The exchange interaction comes in different manifestations depending on the material: direct and indirect interaction between spins of ions at lattice sites, indirect interaction via itinerant conduction electrons (Ruderman-Kittel-Kasuya-Yoshida also known as RKKY interactions) [16, pp. 141–143], but also interaction between the itinerant electrons.

Different models to describe exchange interactions are available, but no complete model exists considering all kinds of interactions [2, p. 48]. Without knowing about exchange interactions, in 1907 Weiss already proposed a classical approach by using an additional molecular field which should describe the force responsible for the spontaneous alignment [95, pp. 55–59]. For certain cases this model is valid and still useful today.

Addressing localized spins, Heisenberg formulated a model to describe exchange interactions by quantum mechanics [95, p. 63], [2, pp. 35–43], [16, pp. 135–138]. The Heisenberg-Hamiltonian reads

$$\mathcal{H} = -2 \sum_{i>j} \mathcal{J}_{i,j} \hat{S}_i \cdot \hat{S}_j, \quad (2.14)$$

with \mathcal{J} being the exchange integral and \hat{S} the spin operators on the lattice sites i and j . Usually the exchange integral is hard to obtain. Generally, if $\mathcal{J} > 0$ the coupling between spins is parallel and describes ferromagnetism, if $\mathcal{J} < 0$ the coupling is antiparallel and antiferromagnetism or ferrimagnetism is observed.

In many magnetic materials, especially in metals, direct localized interactions are still too weak to explain ferromagnetism as for example in iron. Here the most important contribution stems from the delocalized conduction electrons which interact with each other. Therefore a band model was proposed, which only considers a gas of free itinerant electrons. The model states, that for ferromagnetic materials a spin-splitting of the electronic band structure decreases the overall energy. In other words, by changing spin directions to align spins parallel, the energy is more reduced by exchange interactions than increased by the kinetic energy associated with the flipped spins.

Magnetocrystalline anisotropy

The exchange interaction alone does not favor any specific direction of spin alignment. But in most ferromagnetic materials the magnetization direction is not random. There are different types of anisotropy at work, but the most important one is the magnetocrystalline anisotropy. It is caused by the electrostatic crystal field and spin orbit interaction [133, pp. 73–76]. It is therefore tightly bound to the crystallographic structure of the material. Hence, most magnetic materials show, depending on the lattice structure, one or several preferred axes, planes or cones in which the magnetic moments are aligned. The anisotropy energy can be understood as the energy required to rotate the magnetization away from a preferred direction.

In hexagonal crystals the magnetocrystalline anisotropy is uniaxial. The anisotropy energy is a function of the angle θ between the magnetization and the preferred crystallographic c-axis, also called easy axis. The energy density is described by the first terms of a power series

$$\varepsilon_{\text{ani}} = K_u \sin^2 \theta + K_2 \sin^4 \theta. \quad (2.15)$$

The anisotropy constants K_u and K_2 are temperature dependent and usually gained experimentally. Experiments show that for most ferromagnetic materials terms of higher order can be neglected, often even the second term. In most hexagonal crystals

$K_u > 0$, which means the material has an easy axis. For $K_u < 0$ the material shows an easy plane perpendicular to the now hard c-axis [2, pp. 85–86]. It is often useful to describe the anisotropic contribution as an anisotropy field. Neglecting K_2 the anisotropy field is

$$H_{\text{ani}} = \frac{2K_u}{\mu_0 M_s}. \quad (2.16)$$

Magnetostatic field

Another relevant, but often considerably weaker anisotropy contribution is the shape anisotropy. It derives from the demagnetization energy, also called magnetostatic self-energy, and depends on the shape of a magnetic sample. For a ferromagnetic single domain the shape anisotropy is determined by the ratio between the magnets dimensions, *i.e.* the more elongated a sample is in one direction with respect to the others, the higher is the shape anisotropy in this direction.

The magnetostatic field originates from the dipolar interactions of a magnetized material. Within the magnet the demagnetizing field opposes and reduces the total magnetic moment, hence the name. Outside the magnet the field is also called stray field. The long-range character of magnetostatic interactions leads to a macroscopic orientation of the magnetization, and sequentially to the shape anisotropy [133, p. 81].

Ferromagnets are often categorized into magnetically soft and hard materials. If the magnetic field of a magnet is easily reversed, it is classed as soft magnet. Once magnetized, hard magnets withstand high demagnetization fields. The decisive properties for a magnetic material to be either soft or hard are primarily the magnetocrystalline anisotropy and the demagnetizing field [63, 67] [16, p. 265]. The demagnetizing field tends to reduce the magnetostatic energy by forming magnetic domains (see Section 2.3.3) and therefore helps the reversal of the magnetization. If the magnetization reversal is governed by the magnetocrystalline anisotropy, it is called magnetically hard. If the demagnetizing field is the dominating force, the material is called magnetically soft. The external field required to demagnetize a previously saturated magnet to zero is called the coercive field.

2.1.3 Ferrimagnetism

As described previously in Section 2.1.2 the parallel alignment of the magnetic moments due to exchange interaction is the cause for the spontaneous magnetization in ferromagnetic materials. In ferrimagnetic materials however, the coupling between neighboring moments is antiparallel. In the simplest case ferrimagnetic materials can be described with two ferromagnetic sublattices which are coupled antiparallel, as shown in Figure 2.2.

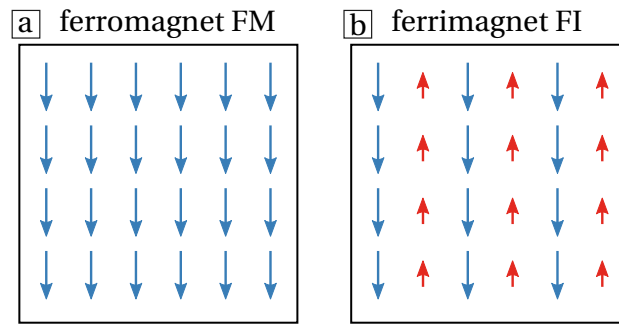


Figure 2.2: Ferromagnetic lattice with parallel aligned magnetic moments [a] and ferrimagnet with two sublattices coupled antiparallel [b].

Generally the magnetic moment of the sublattices are not equal and therefore an overall magnetic net moment remains. If the magnetic moments of both sublattices are equal, the overall magnetization is zero and the material is called antiferromagnetic.

There is a wide range of ferrimagnetic materials such as ferrites and garnets. Rare-earth transition metal alloys like FeTb, GdFeCo or FeGd are ferrimagnets which have received a great deal of attention for their application in magneto-optical recording [85, 18]. The interest in such materials was renewed when it was demonstrated, that an all-optical switching was possible [135, 147, 115, 156]. The optical switching of the magnetization can be done in a picosecond time scale, while conventional recording by a magnetic field is done over nanoseconds [80, 106].

The magnetic response of a ferrimagnet depends on the exchange interaction strength between the moments within the sublattices and also between the two sublattices [133, pp. 174–178]. Therefore the magnetic properties strongly depend on the composition of the ferrimagnet [93]. The magnetization of the sublattices can also have different temperature dependencies. This can lead to a magnetization compensation point at a certain temperature below the Curie temperature. At this point the magnetization of the anti-parallel sublattices are equal and cancel each other out. Contrary to antiferromagnets, the compensation of the opposing moments happens only at a certain compensation temperature. Apart from the possible compensation point, ferrimagnets can often be treated as a ferromagnet since they are also governed by exchange interaction, can show magnetocrystalline anisotropy and a magnetostatic field.

2.1.4 Exchange coupled composites

The concept of exchange coupled composites (ECC) was already proposed for permanent magnets in the early 90s in order to increase the energy product [63, 37]. The

idea behind this approach is to combine the high saturation polarization of soft magnetic materials with the high coercive field of magnetically hard materials. Due to the exchange coupling the two-phase magnet might show a reversible demagnetization curve [63]. Since this behavior to some extent resembles a mechanical spring, these composites are also called exchange spring magnets. Strong permanent magnets with a high energy product, even at elevated temperatures, are an essential component for modern and future applications, especially in green technologies like wind turbines or electric vehicles [56, 10, 48].

Another big branch of exchange coupled composites are exchange bias magnets discovered by Meiklejohn and Bean [91] in the 50s. In exchange bias magnets an antiferromagnetic layer is exchange coupled to a ferromagnetic layer. Due to their antiparallel sublattices with equal magnetic moment, the antiferromagnet itself shows almost no response to an applied external field. However, at the interface the magnetic moments of the ferromagnet are pinned due to strong exchange coupling. The coupling at the interface leads to an unidirectional anisotropy of the magnet. Therefore, the required field to switch the magnet is considerably higher in one direction than in the opposite direction. The hysteresis curve is shifted along the field axis, hence the term exchange bias. Exchange bias magnets found their application in magnetic recording media, recording read heads, magnetic sensors and magnetoresistive random access memory (MRAM) [100].

The concept of exchange coupled composites was later transferred to magnetic recording media, apparently simultaneously but independently by Suess *et al.* [139] and Victora and Shen [150] in 2005. Here, in order to overcome the magnetic recording trilemma (see Section 2.4.1) the storage media should consist of at least two layers, a soft and a hard phase. While the hard phase is the actual storage layer, which is thermally stable, the exchange coupled soft layer helps to switch the bits on the hard layer during writing. Since then the application of ECC in magnetic recording is an extensively studied topic as it is seen as an important approach to increase storage density in hard disk drives (HDD) [15, 151, 138, 137]. Moreover the combination of ECC with heat assisted magnetic recording (HAMR) [140] and/or bit patterned media (BPM) [94, 69] was proposed. Even though these combinations would push the theoretical limit of storage density even higher, ultimately the fabrication costs will determine if future recording devices really employ these technologies.

2.2 Micromagnetism

In general, the term micromagnetism comprises models for magnetic phenomena on a submicron length scale. Therefore features like magnetic domains, domain walls, magnetic pinning and nucleation also considering the microstructure can be described. The magnetic switching behavior and hysteresis is heavily influenced by

these micro-features and therefore can be investigated by micromagnetic models as well.

When micromagnetism was first introduced by Brown, magnetic problems were treated analytically or semi-analytically. With the dawn of modern computers, Brown soon proposed the numerical treatment of micromagnetic equations [13]. With the increase of computing power during the 80s, micromagnetic simulations became an important tool to study magnetic problems [34]. The so-called static approach was used to calculate magnetization configurations and determine nucleation fields. This calculation is time independent and is done by minimizing the energy of the magnetic system. The further increase in computing power enabled the deployment of time dependent dynamic micromagnetics. Dynamic approaches are based on the equation of motion introduced by Landau and Lifshitz [76], or by Gilbert [40], which describes the time evolution of the magnetization [75].

Since magnetism is a quantum mechanical effect (see Section 2.1.1), a quantum mechanical treatment of magnetic phenomena might be the best option. However, the huge number of atomic spins involved currently prevents the quantum mechanical treatment for magnets above a length scale of nanometers. The classical macroscopic treatment by Maxwell's equations on the other hand, does not consider micromagnetic features. Micromagnetism is a continuum theory and neglects the quantum mechanical spins and replaces them with a continuous vector field. The underlying assumption is, that the spin orientation changes only slightly from one lattice point to the next. With this classical approximation of a quantum mechanical effect the micromagnetic theory is also called a quasi-classical theory. By combining the classical description of magnetic effects on the length scale of nanometers as exchange interaction and the effects on much bigger length scales as the demagnetizing energy, the theory of micromagnetism is the best available tool to investigate the magnetization distribution of a material in the nano- to micrometer range.

The theory of micromagnetism has some basic assumptions:

1. The spin operators of the Heisenberg model are replaced by classical vectors assuming almost parallel alignment of neighboring spins.
2. The magnetization \mathbf{M} is defined as a spatial density of magnetic moments
3. The magnitude of the magnetization is constant over the ferromagnetic sample and depends on the temperature
4. The temperature is constant in time and space

Micromagnetics is still a strongly investigated field of science and continuously expanded or tailored to solve specific questions, as for example the treatment of highly inhomogeneous structures [5] (challenging assumption 1.) or the possibility to have rapidly changing temperature [9] (challenging assumptions 3. and 4.).

2.2.1 Static micromagnetism

The goal of micromagnetic calculation is to describe the magnetic state, *i.e.* the spatial vector field $\mathbf{M}(\mathbf{x})$ of a magnet, in response to an external field, considering the ferromagnetic effects such as exchange interaction, magnetocrystalline anisotropy and demagnetizing field (see Section 2.1.2). Here \mathbf{x} is the positional vector. Since the magnitude of each magnetization vector is constant, the magnetic configuration can be described by the unit vector field $\mathbf{m}(\mathbf{x}) = \mathbf{M}(\mathbf{x})/M_s$, with M_s being the spontaneous magnetization.

The magnetic static state of a material is determined by an (at least local) energy minimum. Therefore the energy has to be formulated in terms of $\mathbf{m}(\mathbf{x})$ and the total energy has to be minimized [16, p. 234]. The total energy of a system to be minimized is called the Gibbs free energy E_{tot} and is the sum of all the energy contributions: the exchange energy E_x , the magnetocrystalline anisotropy energy E_{ani} , the magnetostatic energy E_{dmag} and the energy of an applied external field E_{ext} .

$$E_{\text{tot}} = E_x + E_{\text{ani}} + E_{\text{dmag}} + E_{\text{ext}} \quad (2.17)$$

Depending on the investigated phenomena more energy terms, like magnetoelastic or magnetostrictive energy, can be added. In the following the most important energy terms are described (see derivations in [16, pp. 234–237], [72, pp. 13 – 27], [34]).

Exchange interaction

To formulate an energy term for exchange interaction the continuum approximation is used. The spin operators of the Heisenberg Hamiltonian (2.14) are replaced by classical vectors. The exchange interaction is short ranged and only small spatial changes in magnetization are assumed. After reduction by the energy of a completely aligned spin state as a reference state, the exchange energy is [34]

$$E_x = \mathcal{J} S^2 \sum \varphi_{i,j}^2 \quad (2.18)$$

with $\varphi_{i,j}$ being the angle between the two neighboring spins i and j , and S being the spin quantum number. By assuming these angles to be small, they can be replaced by the difference of the two relevant vectors \mathbf{m}_i and \mathbf{m}_j to express exchange energy in terms of $\mathbf{m}(\mathbf{x})$. A subsequent first order Taylor expansion leads to

$$\|\varphi_{i,j}\| \approx \|\mathbf{m}_i - \mathbf{m}_j\| \approx \|(\mathbf{r}_i \cdot \nabla) \mathbf{m}_j\| \quad (2.19)$$

with \mathbf{r}_i being the position vector joining the lattice points i and j . Thus the exchange energy can be rewritten in terms of the magnetic vectors as

$$E_x = \mathcal{J} S^2 \sum_i \sum_{\mathbf{r}_i} \|(\mathbf{r}_i \cdot \nabla) \mathbf{m}_j\|^2. \quad (2.20)$$

Being a short range interaction, the second sum over position vectors \mathbf{r}_i is only over the nearest neighbors. Eventually, by replacing the first summation by an integral over the whole magnetic sample Ω , the exchange energy is obtained

$$E_x = \int_{\Omega} A_x (\nabla \mathbf{m})^2 d\mathbf{x} \quad (2.21)$$

with

$$(\nabla \mathbf{m})^2 = (\nabla m_x)^2 + (\nabla m_y)^2 + (\nabla m_z)^2 \quad (2.22)$$

and the exchange stiffness constant

$$A_x \approx \frac{\mathcal{J} S^2 n_c}{a}. \quad (2.23)$$

Since the exchange stiffness constant is proportional to the exchange integral \mathcal{J} , it is usually determined experimentally. The parameter n_c is the number of atoms per unit cell of the crystal and a is the lattice constant of the crystal [16, p. 235]. Values for A_x are usually in the range of 1 to 30 pJ/m.

Magnetocrystalline anisotropy

As described previously in Section 2.1.2 magnetocrystalline anisotropy is caused by the crystal field and spin-orbit interaction of the electrons. This leads to preferred directions (easy axes) to align the magnetic moments. The anisotropy energy can be described as the energy required to rotate the magnetic moments out of these preferred axes. In the simplest case, as in hexagonal or tetragonal crystallites, the material has a single easy axis. In this case the energy E_{ani} is a function of the angle θ between the magnetic moment and the crystallographic c-axis. The energy density of such a uniaxial system is shown in Figure 2.3.

Integrating over the energy density ε_{ani} formulated in (2.15) gives the uniaxial magnetocrystalline anisotropy energy

$$E_{\text{ani}} = \int_{\Omega} K_u \sin^2 \theta + K_2 \sin^4 \theta d\Omega \quad (2.24)$$

Often $K_u \sin^2 \theta$ is the dominating term and the higher order term can be neglected. The uniaxial magnetocrystalline anisotropy constant K_u is usually found experimentally and ranges from 100 J/m³ to 10 MJ/m³. By using the identity $\sin^2 \theta = 1 - (\mathbf{m} \cdot \mathbf{k})^2$ and neglecting the second term of (2.24) the anisotropy energy might also be expressed more conveniently in terms of the magnetic moment as

$$E_{\text{ani}} \approx - \int_{\Omega} K_u (\mathbf{m} \cdot \mathbf{k})^2 d\Omega. \quad (2.25)$$

Here \mathbf{k} is the unit vector pointing in the direction of the easy axis.

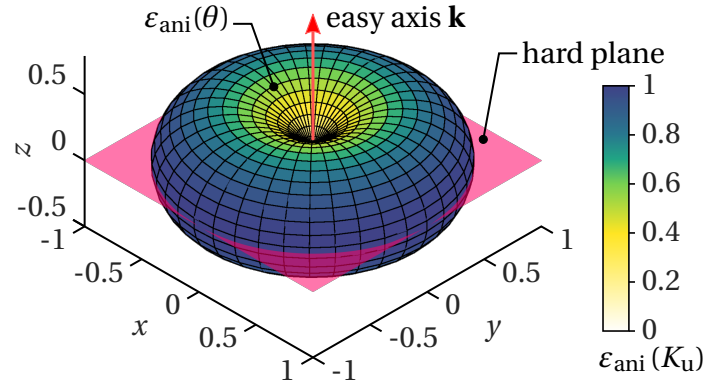


Figure 2.3: Magnetocrystalline anisotropy energy density ε_{ani} as a function of the direction for an uniaxial system ($K_u > 0$). The easy axis is parallel to the z -axis, while rotating the magnetic moment into the xy -plane requires maximum energy.

Demagnetizing energy

The dipolar interaction energy is a magnetostatic energy and created by the field of the magnetization of the material itself. It opposes the magnetization, hence it is called the demagnetization energy. Each magnetic dipole in a material creates a field and therefore each magnetic moment is exposed to the field created by all other dipoles. Contrary to the exchange energy the demagnetizing energy stems from long range interactions. In addition the created field in the environment around the magnetic material, called stray field, has to be considered. This makes the calculation more complicated, since it is an open boundary problem with boundary conditions at infinity. Computing this energy contribution is the most demanding, hence different approaches like Fast Fourier Transformation (FFT) techniques [86] or a hybrid finite element/boundary element method (FEM/BEM) [64] have been used. A comprehensive description of the magnetostatic energy is given in [129] or [2, pp. 141–156].

Generally, the energy can be calculated by summing up the energy of each magnetic moment in the demagnetizing field \mathbf{H}_{dmag} produced by the magnetization of the surrounding magnetic moments. For the continuum approach the sum can be replaced by an integral over the magnetic body

$$E_{\text{dmag}} = -\frac{\mu_0}{2} \int_{\Omega} \mathbf{M} \cdot \mathbf{H}_{\text{dmag}} d\Omega \quad (2.26)$$

$$= -\frac{J_s}{2} \int_{\Omega} \mathbf{m} \cdot \mathbf{H}_{\text{dmag}} d\Omega \quad (2.27)$$

Because the demagnetizing field is non-rotational ($\nabla \times \mathbf{H}_{\text{dmag}} = 0$) it can be written as

a gradient of a scalar potential

$$\mathbf{H}_{\text{dmag}} = -\nabla\phi. \quad (2.28)$$

With Gauss's law for magnetism $\nabla \cdot \mathbf{B} = 0$ and the relation (2.11) it holds

$$\nabla \cdot \mathbf{H}_{\text{dmag}} = -\nabla \cdot \mathbf{M}, \quad (2.29)$$

which with (2.28) plugged in leads to

$$\nabla^2\phi = \nabla \cdot \mathbf{M}. \quad (2.30)$$

Equation (2.30) is the Poisson equation and can be solved using Green's function. Outside the magnetic body the magnetization is zero, therefore one gets a discontinuity at the magnet's surface

$$\nabla^2\phi_{\text{in}} = \nabla \cdot \mathbf{M} \quad (2.31)$$

$$\nabla^2\phi_{\text{out}} = 0. \quad (2.32)$$

Boundary conditions have to be defined, so that at the surface of the magnetic body the continuity of the normal component of \mathbf{B} (from $\nabla \cdot \mathbf{B} = 0$) and the tangential component of \mathbf{H}_{dmag} (from $\nabla \times \mathbf{H}_{\text{dmag}} = 0$) is ensured. In terms of the scalar potential these conditions may be written as [35]

$$\phi_{\text{in}} = \phi_{\text{out}} \quad (2.33)$$

$$(\nabla\phi_{\text{out}} - \nabla\phi_{\text{in}}) \cdot \mathbf{n} = \mathbf{M} \cdot \mathbf{n}, \quad (2.34)$$

where \mathbf{n} is the unit surface normal pointing outwards. Obeying these boundary conditions (2.30) is solved for the scalar potential

$$\phi(\mathbf{x}) = -\frac{1}{4\pi} \left(\int_{\Omega} \frac{\rho(\mathbf{x}')}{\|\mathbf{x} - \mathbf{x}'\|} dV' - \int_{\partial\Omega} \frac{\sigma(\mathbf{x}')}{\|\mathbf{x} - \mathbf{x}'\|} dS' \right). \quad (2.35)$$

Analogue to the electrostatic Poisson's equation, the magnetic volume charge

$$\rho = -\nabla' \cdot \mathbf{M}(\mathbf{x}') \quad (2.36)$$

and the magnetic surface charge

$$\sigma = \mathbf{M}(\mathbf{x}') \cdot \mathbf{n} \quad (2.37)$$

are defined. Now (2.28) can be solved for \mathbf{H}_{dmag} and used in the formulation (2.27) for the demagnetization energy.

Zeeman energy

By applying an external field \mathbf{H}_{ext} on a magnet another energy contribution is added, the Zeeman energy. The interaction energy of the magnet is computed by summing up the product of the dipole moments \mathbf{m}_{tot} with the applied field

$$E_{\text{ext}} = -\mu_0 \sum_i \mathbf{m}_{\text{tot}}^i \cdot \mathbf{H}_{\text{ext}} \quad (2.38)$$

Again the transformation to a continuum model can be made by using the magnetization per unit volume and integration

$$E_{\text{ext}} = - \int_{\Omega} \mu_0 \mathbf{M} \cdot \mathbf{H}_{\text{ext}} \, d\Omega \quad (2.39)$$

$$= - \int_{\Omega} J_s \mathbf{m} \cdot \mathbf{H}_{\text{ext}} \, d\Omega. \quad (2.40)$$

Gibb's free energy

In order to compute the magnetic equilibrium state the sum of all these energy terms, the Gibb's free energy

$$E_{\text{tot}} = \int_{\Omega} A_x (\nabla \mathbf{m})^2 - K_u (\mathbf{m} \cdot \mathbf{k})^2 - \frac{J_s}{2} \mathbf{m} \cdot \mathbf{H}_{\text{dmag}} - J_s \mathbf{m} \cdot \mathbf{H}_{\text{ext}} \, d\Omega \quad (2.41)$$

is minimized. The energy minimization is a fast way to compute the magnetic state, but also has its drawbacks. By design this approach does not consider dynamic magnetic phenomena and only the nucleation field of a magnet in a reversal process can be found. The magnetic system may also show a more complex energy landscape with many local extrema which makes it harder to determine the correct reversal process of a magnet.

The Gibb's free energy can also be translated to an effective field that collects all the field contributions and acts on the magnet

$$\mathbf{H}_{\text{eff}} = -\frac{1}{M_s} \frac{\delta E_{\text{tot}}}{\delta \mathbf{m}} = \frac{2A_x}{M_s} \Delta \mathbf{m} + \frac{2K_u}{M_s} \mathbf{k} (\mathbf{m} \cdot \mathbf{k}) + \mathbf{H}_{\text{ext}} + \mathbf{H}_{\text{dmag}}. \quad (2.42)$$

When the magnetic system is relaxed, *i.e.* in the energy minimum, the magnetization is parallel to this effective field

$$\mathbf{M} \times \mathbf{H}_{\text{eff}} = \mathbf{0}. \quad (2.43)$$

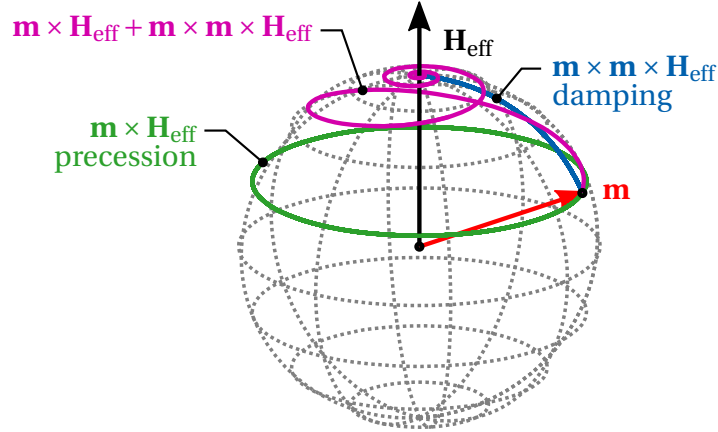


Figure 2.4: Traces of the time evolution of the magnetic moment (red) on the unit sphere generated by the precession term (green), damping term (blue) and both terms combined (magenta) of the Landau-Lifshitz-Gilbert equation.

2.2.2 Dynamic micromagnetism

A more realistic approach to bring the magnetic system to an energetic minimum is the description of motion of the magnetic moments. Contrary to the minimization of the energy, this approach describes the time evolution of the magnetic moments towards the energetic minimum. In 1935 Landau and Lifshitz derived a dynamic micromagnetic equation from the thermodynamical principle of irreversibility [76]

$$\frac{\partial \mathbf{M}}{\partial t} = -|\gamma| \mathbf{M} \times \mathbf{H}_{\text{eff}} - \lambda \mathbf{M} \times (\mathbf{M} \times \mathbf{H}_{\text{eff}}). \quad (2.44)$$

The motion of the magnetic moment is usually dominated by the first term on the right hand side of (2.44). It describes the precession of the magnetic moment around the effective field \mathbf{H}_{eff} from (2.42), called the Larmor precession with the frequency of $-\gamma\mu_0 \|\mathbf{B}\|$. The second term represents the damping term which moves the magnetic moment towards energetic equilibrium, *i.e.* parallel to \mathbf{H}_{eff} (see Figure 2.4). The prefactor λ is a phenomenological damping constant.

Later, in 1955 Gilbert replaced the damping term by a still phenomenological term [82] with the damping prefactor α [40]. The Gilbert equation reads

$$\frac{\partial \mathbf{M}}{\partial t} = -|\gamma| \mathbf{M} \times \mathbf{H}_{\text{eff}} + \alpha \mathbf{M} \times \frac{\partial \mathbf{M}}{\partial t}. \quad (2.45)$$

By modifying the prefactors the Gilbert equation can be transformed into the Landau-Lifshitz form [82, 35], also called the Landau-Lifshitz-Gilbert equation

$$\frac{\partial \mathbf{M}}{\partial t} = -\gamma' \mathbf{M} \times \mathbf{H}_{\text{eff}} - \frac{\alpha \gamma'}{M_s} \mathbf{M} \times (\mathbf{M} \times \mathbf{H}_{\text{eff}}) \quad (2.46)$$

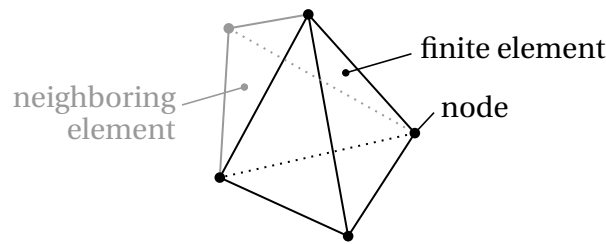


Figure 2.5: Representation of a tetrahedral finite element, the basic building block of the finite element meshes used in this thesis.

with

$$\gamma' = \frac{|\gamma|}{1 + \alpha^2}. \quad (2.47)$$

This form is the most used in numerical micromagnetics. It can be seen from (2.46) and (2.47), that the Gilbert damping constant α also affects the precession term. While in (2.44) the damping factor λ only affects the damping term, in (2.46) the damping factor α slows down the precession of the magnetic moment. For very small damping, formulations (2.44) and (2.46) are equivalent.

2.2.3 Finite element calculations

Computing the magnetic state by energy minimization (Section 2.2.1) or by dynamic micromagnetics (Section 2.2.2) usually requires a numerical approach. The micromagnetic differential equations have to be solved repeatedly for the entire magnetic sample. Therefore the investigated space needs to be discretized. Depending on the problem (and of course availability of the software) either the finite difference (FD) or the finite element (FE) method is used. While the FD method usually needs lesser computing resources compared to the FE method, a regular lattice of the domain is needed. For curved and more complex structures the FE method is used, which usually employs an unstructured tetrahedral mesh to discretize the spatial domain. Popular micromagnetic software using FD are *OOMMF* [25] or *mumax* [148], while the FE method is employed for example by *nmag* [33] or *magnum.fe* [1].

In this thesis the FE software package *FEMME* [128] is used for the simulations. To generate the finite element mesh, *i.e.* the ensemble of all tetrahedral elements representing the investigated space, the software *Salomé* [124], *Neper* [114] and *Gmsh* [39] have been used. The solution of the equation to be solved on this spatial domain is approximated by piecewise continuous polynomials (also called basis or shape functions) and thereby split into a system of algebraic equations depending on the finite elements. The unknown coefficients of these polynomials are then determined

by minimizing the distance to the exact solution. The solution is approximated on the nodes of the finite element mesh and interpolated in each finite element. Thereby the problem to find the continuous solution of the differential equation has been reduced to find a finite number (depending on the number of elements) of coefficients of the basis functions by minimization. A detailed explanation of finite element techniques for micromagnetic applications can be found in [35] or [129].

2.2.4 Mesh size

An important parameter in micromagnetic finite element (FE) calculations is the size of the finite elements. This parameter is a trade off between accuracy and computational resource requirements. The FE-mesh has to be fine enough, *i.e.* the element edge length small enough, to provide enough mesh nodes to render magnetic processes accurately [23]. On the other hand an increase in mesh nodes means a drastic increase of required computing resources. Rave and his co-workers [117] have shown, that it is sufficient to keep the element size below a characteristic length l_c of a material to capture the reversal process accurately, even in corners and edges of the model. This length is defined by whether the material favors the formation of a Néel- or a Bloch type domain wall during reversal (see Section 2.3.4). The widths of the walls, δ_{BW} (2.59) for the Bloch wall and δ_{NW} (2.61) for the Néel wall, give the characteristic length of the magnet

$$l_c = \min\left(\frac{\delta_{BW}}{\pi}, \frac{\delta_{NW}}{\pi}\right) \quad (2.48)$$

In general, the size of the finite elements have to be smaller than the characteristic length. To showcase the impact of mesh size the demagnetization process of a cuboid ferrimagnet with $100 \text{ nm} \times 100 \text{ nm} \times 20 \text{ nm}$ is calculated with three different values for the mean size of the elements, 10 nm, 3 nm and 2 nm. For the used parameters the actual characteristic length is $l_c = \min(1.06 \text{ nm}, 11.74 \text{ nm})$. An increasing external field is applied in the negative direction to move a domain wall until the whole sample is magnetized in the negative direction. Figure 2.6 shows a huge difference in the demagnetization curve when the mesh size is changed. The smaller the edge length of the mesh elements, the less external field is needed to move the domain wall.

When looking at the actual magnetization configuration of the magnet in Figure 2.7 the shape and movement of the domain wall can be seen. The top row represents three states during the demagnetization of the 10 nm mesh, the bottom row shows three states of the much finer 2 nm mesh. The figure shows the top view of the magnet with blue regions having downwards pointing magnetization and red regions having upwards pointing magnetization. The two regions are separated by a domain wall.

It can be seen, that for the bigger mesh size of 10 nm in the top row, the domain wall is artificially pinned at the finite elements as discussed by Donahue *et al.* [24]. This

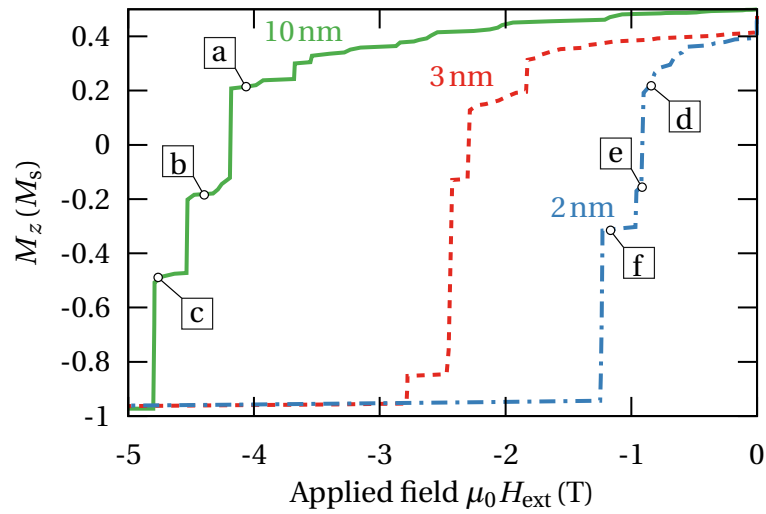


Figure 2.6: Demagnetization curve of a ferrimagnetic sample with spatial variation of easy axis and magnetocrystalline anisotropy computed with three different mesh sizes: 10 nm, 3 nm and 2 nm. The labels correspond to the magnetic configuration states in Figure 2.7.

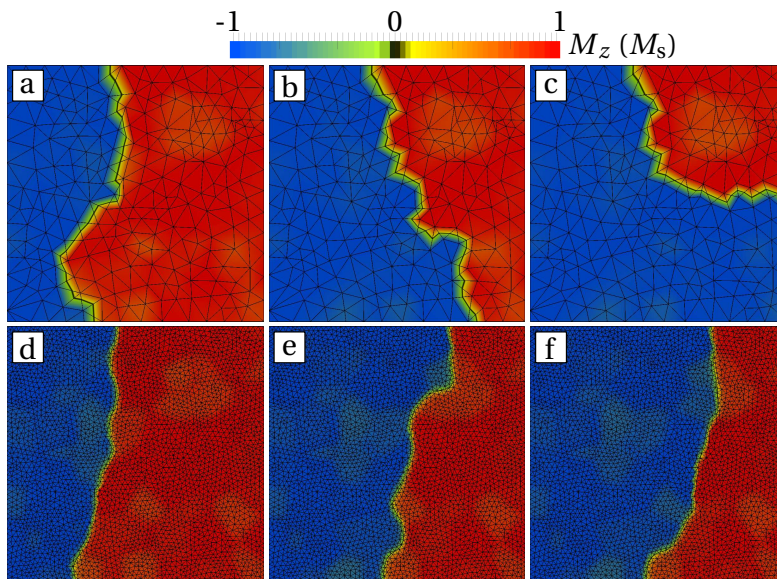


Figure 2.7: Domain wall motion during reversal process for two different mesh sizes: 10 nm [a] to [c] and 2 nm [d] to [f]. The labels [a] to [f] correspond to the state labels in Figure 2.6.

artifact leads to the increased required fields to move the domain wall and eventually produces unrealistic results. The bottom row with 2 nm mesh size gives better results but is still above the needed characteristic length of 1.06 nm for this example. However, a smaller mesh size might not be possible due to computing resource restrictions. A possible solution to this limitation is to either reduce the overall sample size and discretize the cuboid with a 1 nm mesh, or use an adaptive mesh refinement [142]. An adaptive mesh has a fine mesh at sites where decisive micromagnetic features are expected to happen and has an increasingly coarser mesh in assumed unimportant regions of the magnetic domain. Therefore, in the above example, the already reversed part could have been meshed with a coarser mesh to reduce computational costs.

2.3 Magnetization reversal

In order to investigate the characteristics of a magnetic material and to compare simulation results with experiments, the study of the magnetization reversal process is the most important option. This means a magnetic sample is exposed to an increasing external field, which eventually aligns the magnetization of the sample in the direction of the field. Usually the magnet is initially fully magnetized in one direction and gets fully reversed into the opposite direction by the applied field. The reversal process reveals several characteristics of the magnet. For example: The magnet could reverse homogeneously or inhomogeneously; nucleation of reversed regions occur at certain locations; a domain wall could form propagating in certain directions; the domain wall could get pinned at inhomogeneities or interfaces. All these magnetic features can serve to understand the underlying characteristics and are also valuable parameters to validate simulations with experiments.

2.3.1 Hysteresis loop

The magnetic response to the applied field depends on the history and initial state of a magnet. This gives the curve $M(H_{\text{ext}})$ its hysteretic behavior. For example, a fully saturated magnet will show a different reversal curve than a magnet which got its initial magnetization configuration by cooling down to room temperature from a temperature above Curie temperature. Therefore the computation or measurement of the hysteresis loop, an example sketch is shown in Figure 2.8, is the most used technique to investigate and compare magnetic materials.

Initially the magnet was fully saturated to M_s by a strong positive field $H_{\text{ext}+}$ in z -direction. When the field is reduced to 0 the remanent magnetization M_r remains due the energy terms for exchange interaction and anisotropy. By increasing the applied field in the negative z -direction more and more regions start to switch until the z -component of the overall magnetization reaches 0. The field required to reach

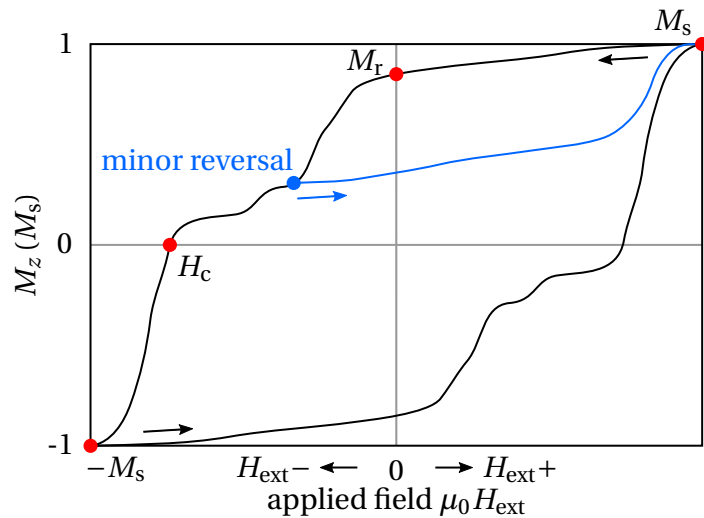


Figure 2.8: Full hysteresis curve of a magnetic material showing some of the main features: saturation magnetization M_s , remanent magnetization M_r and coercive field H_c . An example of a minor reversal curve is also shown in blue.

this point is defined as the coercive field H_c . By increasing the field even further the magnet eventually gets saturated in the opposite direction when $-M_s$ is reached. Reversing the process by decreasing the applied field to 0 and further increase it into the positive direction the initial point is reached at saturation and a full hysteresis loop is completed. Often it is sufficient to just record the second and third quadrant, the curve between M_r and $-M_s$, to gain insight on the magnets behavior.

The determination of a minor reversal curve (blue curve in Figure 2.8) at certain points reveals how stable a just switched region is. Minor reversal curves are obtained by picking an interesting point along the reversal curve in the second or third quadrant and reversing the external field again until positive saturation is reached. A whole set of minor reversal curves along the demagnetization curve can be used to compile a first order reversal curve diagram (FORC) [127] to obtain a "fingerprint" of a magnet.

2.3.2 The Stoner-Wohlfarth model

One of the simplest and also analytically solvable models to describe a magnetic hysteresis is the Stoner-Wohlfarth model [136]. It is often used as a basic example of hysteresis and magnetization reversal [105, pp. 319–321] [16, pp. 247–249] [133, pp. 110–116]. The model describes a spatially uniform magnetized particle (with ellipsoidal shape), small enough to strongly favor only a single domain (see Figure 2.9). The exchange interactions are sufficiently strong to have a constant exchange energy. The particle therefore will reverse its magnetization in a coherent rotation.

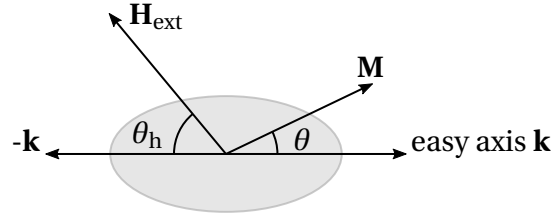


Figure 2.9: Illustration of a Stoner-Wohlfarth particle with parallel shape anisotropy and magnetocrystalline anisotropy (easy axis).

The shape anisotropy of the particle is $\mu_0 M_s^2 (1 - 3D) / 4$ with D being the demagnetization factor [133, pp. 82–83] of the ellipsoid. The particle possesses a uniaxial anisotropy with the easy axis parallel to the long axis of the ellipsoid. Therefore the energy density terms can be summed up to have a combined anisotropy constant K

$$\varepsilon_{\text{ani}} = K_u \sin^2 \theta + \frac{1}{4} \mu_0 M_s^2 (1 - 3D) \sin^2 \theta = K \sin^2 \theta, \quad (2.49)$$

with the angle θ between magnetization vector and easy axis. In order to switch the magnetization \mathbf{M} of the particle, an external field \mathbf{H}_{ext} is applied at an angle θ_h with respect to the negative easy axis direction \mathbf{k} . With the energy density terms for anisotropy and Zeeman energy the total free energy density of the particle is

$$\varepsilon_{\text{tot}} = K \sin^2 \theta + \mu_0 M_s H_{\text{ext}} \cos(\theta_h + \theta). \quad (2.50)$$

The energy minima are found by the equilibrium condition

$$\frac{\partial \varepsilon_{\text{tot}}}{\partial \theta} = K \sin(2\theta) - \mu_0 M_s H_{\text{ext}} \sin(\theta_h + \theta) = 0. \quad (2.51)$$

For small values of H_{ext} the energy landscape will show minima at $\theta = 0$ and $\theta = \pm\pi$. Therefore, depending on the initial state of \mathbf{M} the magnetization will rotate into one of these minima due to the anisotropy energy. The magnetization can only be switched to the other minimum by increasing the external field in the opposite direction. This is the origin of the hysteretic behavior. In order to determine the external field, at which the magnetization switches, the instability condition

$$\frac{\partial^2 \varepsilon_{\text{tot}}}{\partial \theta^2} = 2K \cos(2\theta) - \mu_0 M_s H_{\text{ext}} \cos(\theta_h + \theta) = 0. \quad (2.52)$$

has to be satisfied. To switch the magnetization with a positive initial state $\theta = 0$ by an antiparallel external field $\theta_h = 0$, the external field has to be increased to the so-called nucleation field [133, p. 112]

$$H_n^0 = \frac{2K}{\mu_0 M_s} = H_{\text{ani}} + \frac{1}{2} (1 - 3D) M_s. \quad (2.53)$$

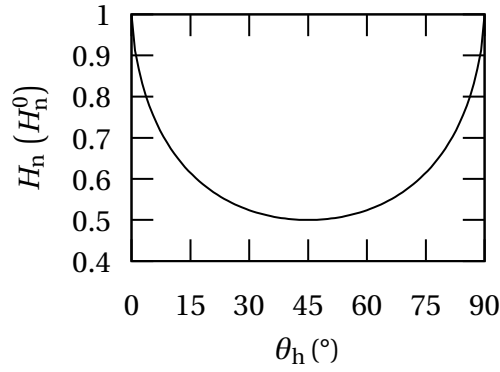


Figure 2.10: Angular dependence of the Stoner-Wohlfarth nucleation field.

Here H_{ani} is the theoretical anisotropy field from (3.9) and the second term is due to shape anisotropy. Generally the nucleation field depends on the angle of the external field θ_h . For $0 \leq \theta_h \leq \pi/2$ the field to switch the particle is given by [72, p. 110]

$$H_n(\theta_h) = H_n^0 (\cos^{2/3} \theta_h + \sin^{2/3} \theta_h)^{-3/2}. \quad (2.54)$$

Figure 2.10 shows the relation between the reduced nucleation field $H_n(\theta_h) / H_n^0$ and the external field angle θ_h .

The nucleation field decreases with increasing θ_h until a minimum is reached at $\theta_h = \pi/4$. At this point only half of the field is needed to reverse the magnetization of the particle as for $\theta_h = 0$. Increasing the field angle further also increases the nucleation field. Equation (2.54) can be used to approximate switching fields of small magnets with coherent reversal for different angles when one angle is known.

In theory the nucleation field represents the upper limit of the coercive field for magnetic materials $H_c \leq H_n$. However, real magnetic materials have inhomogeneities which reduce their H_c to 20% to 30% of H_{ani} . This huge discrepancy between theory and experiment is called Brown's paradox.

2.3.3 Magnetic domains and reversal modes

A magnetic domain is defined as a region in a ferromagnetic (or ferrimagnetic) material within which the magnetization is largely uniform [105, p. 296]. The formation of domains is due to the magnetic system seeking its energy minimum. The creation of multiple magnetic domains is solely due to the demagnetizing energy. In single domain particles the exchange energy is high enough to withstand the demagnetizing energy, but with increasing particle size the demagnetizing field dominates and forms two or multiple domains separated by so called domain walls (see Section 2.3.4).

The Stoner-Wohlfarth model as described in Section 2.3.2 is only valid for sufficiently small particles and uniform magnetization. The size of these particles strongly

favor a single domain to be formed and therefore such magnets reverse their magnetization in a coherent rotation.

However, with decreasing particle size the energy barrier between energy minima decreases to a point where the ambient thermal energy will be large enough to randomly switch the particle's magnetization. The range in which a ferromagnetic particle becomes gradually thermally unstable due to its size is called the superparamagnetic limit. Below this limit the particle shows no net magnetization since the randomly changing magnetization states cancel each other out over time, but still possesses a single magnetic domain. An approximation for the stability is given by the Arrhenius law [133, p. 222]

$$\tau = \frac{1}{f_0} \exp\left(\frac{K_u V}{k_B T}\right), \quad (2.55)$$

where τ is the expected life time of a magnetic state before it switches, f_0 is the attempt frequency (usually in the range of 1 to 100 GHz [15, p. 64]) and T is the temperature. The energy barrier is determined by the anisotropy constant and the particle volume $K_u V$. Reformulating (2.55) and expecting a life time of 10 years yields the minimum energy barrier needed to resist thermal fluctuations

$$K_u V = k_B T \ln(\tau f_0) \approx 40 k_B T. \quad (2.56)$$

This means, that at room temperature a spherical particle with $K_u = 1 \text{ MJ/m}^3$ needs at least a diameter of 14.5 nm to be magnetically stable for this time period.

In Figure 2.11 the schematic drawing of the nucleation field as function of particle size is shown. Very small particles are below the superparamagnetic limit and are therefore subject to thermal fluctuations. With increasing particle size the regime with the highest H_n is reached. Here approximations by the Stoner-Wohlfarth model are most accurate since the assumption of coherent magnetic reversal is met. Increasing the particle size further leads to a reduction of the nucleation field since demagnetizing energy gets more prominent. The demagnetization field therefore is allowed to re-orientate magnetic moments to reduce the systems energy and the magnetization in the particle becomes inhomogeneous. This influence can be seen in the reversal of the particle, when the nucleation field is decreased by the curling of magnetic moments. For a spherical particle the transition from coherent reversal to curling reversal is at a diameter of [133, p. 132]

$$d_{\text{coherent}} \approx 10.2 \sqrt{\frac{A_x}{\mu_0 M_s^2}}. \quad (2.57)$$

Eventually, with even bigger particles the demagnetizing field can induce magnetic domains separated by domain walls to lower the overall energy, and consequently the

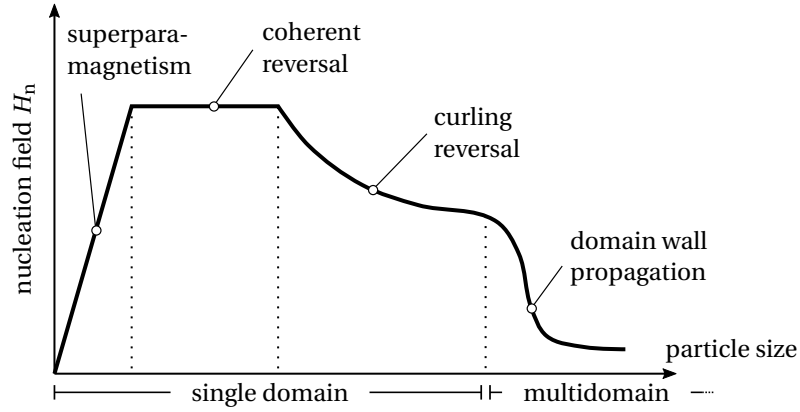


Figure 2.11: Schematic representation of nucleation field H_n as function of the magnetic particle size, based on the figure in [72, p. 102]. The superparamagnetic regime as well as the different reversal modes depending on particle size are shown.

nucleation field. A magnet which was not yet magnetized or a soft magnet might show very little net magnetization since magnetic domains have been formed. Applying an external field will enlarge the magnetic domains oriented parallel to this field by moving domain walls into other domains until the whole magnet is aligned. It should be noted here that particles with a size in the multidomain regime can still hold a single domain when previously magnetized due to exchange and anisotropy energy. But contrary to small particles, these particles reverse by nucleation and propagation of a domain wall. For a spherical particle with uniaxial anisotropy the transition from single to multidomain regime is at the critical diameter [133, p. 126]

$$d_{\text{single}} \approx 72 \frac{\sqrt{A_x K_u}}{\mu_0 M_s^2}. \quad (2.58)$$

For example a spherical particle with $A_x = 1 \text{ pJ/m}$, $K_u = 1 \text{ MJ/m}^3$ and $J_s = 1 \text{ T}$ has a critical diameter of $d_{\text{single}} = 90 \text{ nm}$.

Looking at Figure 2.11 might give the idea that magnets composed of nanoparticles in the coherent reversal regime are the only solution to achieve high coercive fields. But as already mentioned in Section 2.3.2 Brown's paradox shows a huge discrepancy between the theoretical H_n and the H_c of real magnets. While inhomogeneities within the material (like contamination with different materials or defects in the crystallographic lattice) lower the switching field for single domain particles, in the multidomain regime inhomogeneous sites can help to increase H_c by pinning the domain wall at such sites after nucleation.

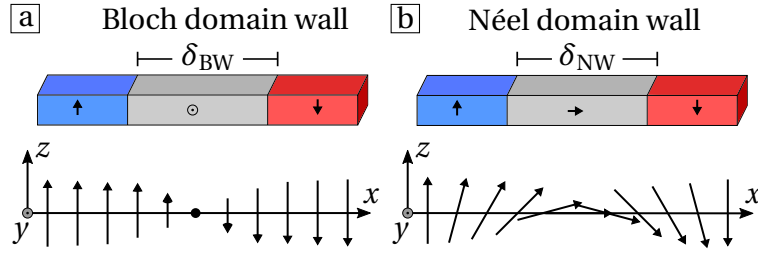


Figure 2.12: Illustration representing the spin configuration across a Bloch domain wall [a] and a Néel domain wall [b].

2.3.4 Domain walls and domain wall pinning

If the demagnetizing energy of a magnetic sample is big enough to dominate over exchange and anisotropic energy, magnetic domains separated by domain walls are formed to minimize the systems energy. Domain walls are thin regions between two domains where the magnetic spins are allowed to rotate from one domain direction to the other domain's direction. This rotation costs energy because it works against the exchange interactions of neighboring spins. In a material with uniaxial anisotropy, the anisotropic energy favors only the two antiparallel directions of the easy axis and tries to minimize the number of spins with intermediate rotation angles within the wall (see Figure 2.12). These competing forces lead to a characteristic domain wall width. In magnetically hard materials a 180° Bloch wall will be formed with the domain wall width

$$\delta_{\text{BW}} = \pi \sqrt{\frac{A_x}{K_u}}. \quad (2.59)$$

The energy cost per domain wall area to form this wall is

$$\gamma_{\text{BW}} = 4 \sqrt{A_x K_u}. \quad (2.60)$$

From (2.59) and (2.60) it can be seen, that an increase of the anisotropy constant increases the wall energy and decreases the domain wall width. This also means that in soft magnetic materials, where K_u is much smaller, domain walls become much wider to an extent that states with continuous rotation of magnetization form [16, p. 240]. Here the definition of domains becomes less clear. While in magnetically hard bulk magnets the domain wall configuration is determined by the competing anisotropy energy and exchange interaction, in thin magnetically soft films the demagnetizing energy is the determining term. In such films the formation of a Néel wall is very common. The magnetic configuration of both a Bloch wall and a Néel wall is shown

in Figure 2.12. Here the x -axis is defined in the normal direction of the domain wall. The neighboring domains possess antiparallel magnetization in z -direction. A Bloch wall is formed by gradually rotating the magnetic spins within the yz -plane along the x -axis. In a Néel wall the spins are gradually rotating within the xz -plane along the x -axis.

The domain wall width of a Néel wall is

$$\delta_{\text{NW}} = \pi \sqrt{\frac{2\mu_0 A_x}{J_s^2}}. \quad (2.61)$$

There are many more different domain wall configurations with different angles between neighboring domains and much more complex spin configurations. They all are the result of the tendency to minimize the systems overall energy and competing energy terms. In order to investigate domain walls in a micromagnetic simulation the mesh size has to be sufficiently small to resolve the rotating magnetic moments across the wall (see Section 2.2.4).

Domain wall pinning

In a perfectly homogeneous magnet the coercive field would be equal to the nucleation field. With increasing applied opposing field a small reversed region would nucleate and the so formed domain wall would immediately propagate and reverse the whole magnetic domain. Real magnets though are almost exclusively inhomogeneous. During reversal, the domain wall can get stuck at local defects and needs an increased external field to move further. This pinning therefore leads to $H_c > H_n$. There are many possible sources of defects, like crystallographic defects or impurities and very often grain boundary phases in granular material. These defects imply a change in the magnetic properties K_u and A_x . Hence, if the domain wall approaches a defect the domain wall energy (2.60) changes. If the domain wall energy decreases, the domain wall is trapped in this energy well and needs an increased external field to get pushed further. This type of pinning is called *attractive* pinning. Figure 2.13 [a] shows an example for attractive pinning. The energy well is formed due to a magnetically soft phase between two hard magnetic grains as often seen in granular media. To push the domain wall further to reverse the neighboring grain, an increased external field is necessary. If the domain wall energy is increased by the property change, the defect creates an energy barrier which again needs increased external field to overcome. In this case the increased H_c is caused by *repulsive* pinning. The pinning types at different defects are elaborately discussed in [72].

Exchange coupled composites possess an additional pinning site to consider. The interface between two materials constitutes a huge plane where magnetic properties are suddenly changing. This can lead to domain wall pinning during magnetization reversal. Therefore the investigation of domain wall propagation and pinning plays an

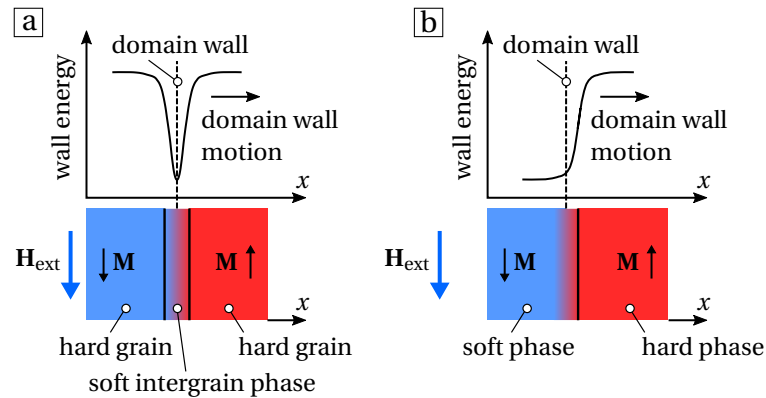


Figure 2.13: Attractive domain wall pinning at a soft grain boundary phase [a] and repulsive pinning at a soft-/hard phase transition [b].

important role in the development and design of magnetic multilayer structures [141, 151]. Figure 2.13 [b] shows an example of repulsive pinning at the interface between a soft and a hard magnetic material. The domain wall is pinned in the proximity of the interface and only an increase of the applied field can overcome the energy barrier and push the domain wall further into the hard phase.

2.4 Magnetic recording

One of the major possible applications of exchange coupled ferri-/ferromagnetic bilayers, as investigated in this thesis, is the use as storage medium in magnetic recording. Magnetic hard disc drives (HDD) have become the most common secondary storage device in computers. The areal storage density of HDD showed an exponential growth since their introduction, especially from the 90s onwards. The growth slowed down since 2010 due to the magnetic grain size approaching the superparamagnetic limit (see Section 2.3.3). Starting from 310 kb/cm^2 ($\sim 2 \text{ kb/in}^2$) in 1956 the areal density rose to above 200 Gb/cm^2 ($\sim 1.3 \text{ Tb/in}^2$) in recent years. The increase in areal density needed simultaneous improvements in different components of the HDD (see Figure 2.14). The read and write head was reduced in size, reader sensor sensitivity had to be increased and the storage medium was optimized to have smaller grains and a high signal to noise ratio (SNR) [52]. A major step was the transition from longitudinal magnetic recording (LMR) to perpendicular magnetic recording (PMR) in 2005, when the storage medium with the anisotropic easy axis pointing out-of-plane (in PMR) was fabricated instead of in-plane (in LMR).

Despite the rise of solid-state drives (SSD), HDDs are expected to still be in demand for quite some time. Even though SSDs have recently exceeded HDDs in terms of

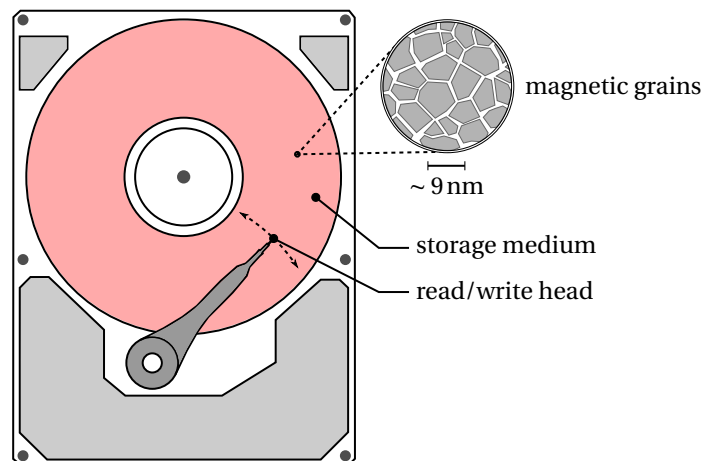


Figure 2.14: Sketch of a magnetic hard disk drive (HDD). The read/write head is mounted on a suspension controlled by a rotary actuator and floats on an air cushion of ~ 2 to 3 nm [52, p. 6] over the storage medium. The recording layer of the medium consists of magnetic grains which can be magnetized in up or down direction by the write head. The local magnetic field of the grains is picked up by the read head and transformed into voltage and sequentially into data bits.

areal density, the price per capacity of SSDs is still about 10 times higher than that of HDDs. For example as of April 2018 comparing consumer grade 4TB drives, the price for SSD is about 300€/TB while HDDs are available for 30€/TB. This price gap is expected to last for the next ten years [92, 17]. The demand for new storage space for newly generated data is growing at an annual rate of 45%, increasingly fueled by the widespread use of mobile devices and social media [11, p. 54]. Hence, the extensive use of cheaper HDDs, especially in large data storage centers serving cloud storage solutions, is expected to be continued for at least the next ten years.

2.4.1 Trilemma of magnetic recording

In current PMR HDDs, bits are written on a granular medium by magnetizing a cluster of grains in an up or down direction. In order to increase areal density the magnetized volume per bit, *i.e.* the number and size of the grains, has to be decreased. When the number of grains per bit is decreased, the transitions between bits relative to bit size are less smooth, hence the SNR is decreased. This negatively affects the readability of a written bit sequence. A decrease in grain size can fall below the superparamagnetic limit (see Section 2.3.3) where data can not be stored reliably due to thermal instability. According to (2.56), to maintain thermal stability when the volume is decreased, the anisotropy needs to be increased. This can be achieved by using a different material

for the recording layer, like $L1_0$ -FePt. The problem with this magnetically hard grains is their high coercivity which makes them impossible to switch by the recording head, since the writing field is limited to around 1 T. These conflicting requirements are known as the *trilemma of magnetic recording*.

2.4.2 Future recording technologies

Different approaches were suggested to overcome these limitations and it is as yet unclear which technology will succeed next. Two main technologies are expected to be introduced in the foreseeable future, heat assisted magnetic recording [118] (HAMR) and microwave assisted magnetic recording [17] (MAMR). Both technologies use an assisting energy contribution to switch the bits.

In HAMR [74] the writeability of the hard magnetic grains is reestablished by selectively heating up the cluster of grains to be written by laser light. The increased temperature decreases the coercive field and the write head is able to record the bit. After writing the grains are allowed to cool down to be thermally stable again.

In MAMR [159] a spin torque oscillator is mounted right on the write head which introduces energy into the medium by microwaves. Again this energy contribution helps to switch the grains when a write field is applied.

Further in the future bit patterned media recording [4] (BPMR) is a possible candidate for even higher areal densities, especially when combined with, for example HAMR (often called heated dot magnetic recording – HDMR). In BPMR the conventional granular medium is replaced by well defined lithographically patterned magnetic islands. Instead of using a cluster of grains to store a bit, in BPMR only one single dot is used. Therefore the transition noise is eliminated and the SNR only depends on position jitter and the distribution of magnetic properties across the dots. In Chapter 5 the use of ferri-/ferromagnetic bilayers for BPMR dots is investigated.

Ferrimagnetic films

Contents

3.1	Micromagnetism for ferrimagnetic thin films	35
3.2	Properties of ferrimagnetic films	37
3.2.1	Fresnel imaging of domain patterns	38
3.2.2	Model for ferrimagnetic films	39
3.2.3	Validation of the ferrimagnetic model	41
3.3	Magnetization reversal and domain wall motion.....	48
3.4	Summary.....	50

Portions of this chapter were previously published in [103] and [101] under the CC BY 4.0 license and have been reproduced with permission of the coauthors and in accordance with the publisher's policy. Content which was not generated by the author of this thesis is explicitly denoted.

Ferrimagnetic materials have been widely used as magneto-optical recording media [73, 58] and provide great potential for future devices in sensor technology and magnetic recording. Interest in ferrimagnetic materials has been renewed by experiments revealing all-optical switching of the magnetization [60, 135, 32]. Ultrafast optical manipulation of the magnetization, with laser pulses in the range of femtoseconds, have been investigated experimentally and by micromagnetic simulations [61].

Ferrimagnetic thin films have been extensively studied by Giles and Mansuripur *et al.* [41, 84, 85, 88] in terms of magneto-optical recording. In their work they investigated the magnetization reversal dynamics and domain wall motion by utilizing an adapted Gilbert equation on a two dimensional lattice of magnetic dipoles. This approach will be used in a three dimensional model system of ferrimagnetic thin films

in the following Section 3.1. Atxitia and his co-workers presented a micromagnetic model utilizing the Landau-Lifshitz-Bloch equation focused on the dynamic behavior up to and above the Curie temperature [8, 99]. They could successfully reproduce the experimental results for ultrafast switching and optical excitation of ferrimagnets.

The aim of this chapter is to investigate the magnetization reversal process of a ferrimagnetic film by micromagnetic calculations. These simulation results are compared to experiments and serve as a basis for the simulations of exchange coupled bilayer films in Chapter 4. The finite-element micromagnetic model for strongly coupled ferrimagnetic thin films proposed by Mansuripur [85], which is used throughout this thesis, is described in Section 3.1. In Section 3.2 microstructural properties are introduced. Magnetic domain patterns with in-plane magnetization in thin square elements are investigated by simulations and compared to measurements. Afterwards the magnetization reversal by domain wall motion of a ferrimagnetic film with out-of-plane anisotropy is calculated and again compared to measurements done by Schubert *et al.* [130].

3.1 Micromagnetism for ferrimagnetic thin films

Ferrimagnets have previously been simulated in two dimensions for the application in magneto-optical recording [88, 109]. In the following a three dimensional model for ferrimagnets will be described. In contrast to the ferromagnetic materials, ferrimagnets possess sublattices with unequal opposing magnetic moments. In the following, it is assumed that two sublattices, superscripts (a) and (b), are strongly coupled antiparallel. With this condition the approach of Mansuripur [85, pp. 652–654] can be used. In this model the Landau-Lifshitz-Gilbert equation from Section 2.2.2 is adapted for ferrimagnets. For each sub-lattice $L^{(a)}$ and $L^{(b)}$ the Gilbert equation from (2.45) can be written as:

$$\dot{\mathbf{M}}^{(a)} = -\gamma^{(a)} \mathbf{M}^{(a)} \times \left(\mathbf{H}^{(a)} + h\mathbf{M}^{(b)} \right) + \alpha^{(a)} \mathbf{M}^{(a)} \times \dot{\mathbf{m}}^{(a)} \quad (3.1a)$$

$$\dot{\mathbf{M}}^{(b)} = -\gamma^{(b)} \mathbf{M}^{(b)} \times \left(\mathbf{H}^{(b)} + h\mathbf{M}^{(a)} \right) + \alpha^{(b)} \mathbf{M}^{(b)} \times \dot{\mathbf{m}}^{(b)} \quad (3.1b)$$

Here the time derivative of magnetization is denoted by Newton's dot notation: $\dot{\mathbf{M}} := \partial \mathbf{M} / \partial t$. The sublattice $L^{(a)}$ is defined by its magnetization magnitude $M^{(a)}$ and its unit vector $\mathbf{m}^{(a)} = \mathbf{M}^{(a)} / M^{(a)}$, the gyromagnetic ratio $\gamma^{(a)}$ and the corresponding damping parameter $\alpha^{(a)}$. The field on the subnet $L^{(a)}$ is split into the effective local exchange field $h\mathbf{M}^{(b)}$ of subnet $L^{(b)}$ acting on subnet $L^{(a)}$ and the sum of the remaining effective fields $\mathbf{H}^{(a)}$. This notation applies to the sublattice $L^{(b)}$ respectively. The scalar h here describes the proportionality of the exchange field to the magnetization. Due to the strongly coupled sublattices, the magnetic moments $\mathbf{M}^{(a)}$ and $\mathbf{M}^{(b)}$ will always stay antiparallel. Therefore the cross products $\mathbf{M}^{(a)} \times h\mathbf{M}^{(b)}$ and $\mathbf{M}^{(b)} \times h\mathbf{M}^{(a)}$ vanish in the

reformulation later on. The permanent antiparallel configuration also allows to define an effective net magnetization as $\mathbf{M} = M\mathbf{m}$ with $M = M^{(a)} - M^{(b)}$ and $\mathbf{m} = \mathbf{m}^{(a)} = -\mathbf{m}^{(b)}$ (see Figure 3.1).

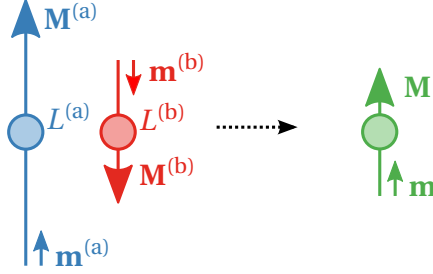


Figure 3.1: In this model the magnetic moments $\mathbf{M}^{(a)}$ and $\mathbf{M}^{(b)}$ of the sublattices $L^{(a)}$ and $L^{(b)}$ of a ferrimagnet are assumed to be antiparallel at all times and therefore substituted by an effective net magnetization \mathbf{M} .

Summing up equations (3.1a) and (3.1b) and substituting the unit vectors of both sublattices with either \mathbf{m} or $-\mathbf{m}$, yields

$$\left(\frac{M^{(a)}}{\gamma^{(a)}} - \frac{M^{(b)}}{\gamma^{(b)}} \right) \dot{\mathbf{m}} = -\mathbf{m} \times \left(M^{(a)} \mathbf{H}^{(a)} - M^{(b)} \mathbf{H}^{(b)} \right) + \left(\frac{\alpha^{(a)} M^{(a)}}{\gamma^{(a)}} + \frac{\alpha^{(b)} M^{(b)}}{\gamma^{(b)}} \right) \mathbf{m} \times \dot{\mathbf{m}} \quad (3.2)$$

By defining the effective values as

$$\gamma_{\text{eff}} = \frac{M^{(a)} - M^{(b)}}{\frac{M^{(a)}}{\gamma^{(a)}} - \frac{M^{(b)}}{\gamma^{(b)}}} \quad (3.3)$$

$$\alpha_{\text{eff}} = \frac{\frac{\alpha^{(a)} M^{(a)}}{\gamma^{(a)}} + \frac{\alpha^{(b)} M^{(b)}}{\gamma^{(b)}}}{\frac{M^{(a)}}{\gamma^{(a)}} - \frac{M^{(b)}}{\gamma^{(b)}}} \quad (3.4)$$

$$\mathbf{H}_{\text{eff}} = \frac{M^{(a)} \mathbf{H}^{(a)} - M^{(b)} \mathbf{H}^{(b)}}{M^{(a)} - M^{(b)}} \quad (3.5)$$

the Gilbert equation of a strongly coupled ferrimagnetic thin film is obtained:

$$\dot{\mathbf{m}} = -\gamma_{\text{eff}} \mathbf{m} \times \mathbf{H}_{\text{eff}} + \alpha_{\text{eff}} \mathbf{m} \times \dot{\mathbf{m}} \quad (3.6)$$

Equation (3.5) is particularized by splitting the effective fields $\mathbf{H}^{(a)}$ and $\mathbf{H}^{(b)}$ into a sum of their components: the external field \mathbf{H}_{ext} , the demagnetizing field \mathbf{H}_{dmag} , the

anisotropy field \mathbf{H}_{ani} and the exchange field \mathbf{H}_x . The external field and the demagnetizing field are equal for both subnets:

$$\mathbf{H}_{\text{dmag}}^{(a)} = \mathbf{H}_{\text{dmag}}^{(b)} = \mathbf{H}_{\text{dmag}} \quad (3.7)$$

$$\mathbf{H}_{\text{ext}}^{(a)} = \mathbf{H}_{\text{ext}}^{(b)} = \mathbf{H}_{\text{ext}} \quad (3.8)$$

For the anisotropy field a common anisotropic easy axis is assumed, defined by an unit vector \mathbf{k} . Each sublattice exhibits its own magnetic uniaxial anisotropy constant, $K_u^{(a)}$ and $K_u^{(b)}$, and therefore different anisotropy fields.

$$\mathbf{H}_{\text{ani}}^{(a)} = \frac{2K_u^{(a)}}{M^{(a)}} (\mathbf{m}^{(a)} \cdot \mathbf{k}) \mathbf{k} \quad (3.9a)$$

$$\mathbf{H}_{\text{ani}}^{(b)} = \frac{2K_u^{(b)}}{M^{(b)}} (\mathbf{m}^{(b)} \cdot \mathbf{k}) \mathbf{k} \quad (3.9b)$$

They also posses exchange fields with different exchange constants, $A_x^{(a)}$ and $A_x^{(b)}$, which are proportional to the Laplacian of their respective magnetization.

$$\mathbf{H}_x^{(a)} = \frac{2A_x^{(a)}}{M^{(a)2}} \nabla^2 \mathbf{M}^{(a)} \quad (3.10a)$$

$$\mathbf{H}_x^{(b)} = \frac{2A_x^{(b)}}{M^{(b)2}} \nabla^2 \mathbf{M}^{(b)} \quad (3.10b)$$

Equations (3.10a) and (3.10b) differ from the model by Mansuripur, since instead of a two-dimensional hexagonal lattice of dipoles, the LLG is solved on a three-dimensional FE-mesh. When defining an effective net anisotropy constant $K_u = K_u^{(a)} + K_u^{(b)}$ and an effective net exchange stiffness constant $A_x = A_x^{(a)} + A_x^{(b)}$, equation (3.5) can be rewritten with $M = M^{(a)} - M^{(b)}$ as

$$\mathbf{H}_{\text{eff}} = \mathbf{H}_{\text{ext}} + \mathbf{H}_{\text{dmag}} + \underbrace{\frac{2K_u}{M} (\mathbf{m} \cdot \mathbf{k}) \mathbf{k}}_{\mathbf{H}_{\text{ani}}} + \underbrace{\frac{2A_x}{M} \nabla^2 \mathbf{m}}_{\mathbf{H}_x} \quad (3.11)$$

Equations (3.3), (3.4) and (3.11) represent all the parameters for the adapted Gilbert equation (3.6) which can be solved by employing the finite element micromagnetic package called *FEMME* [129, 128].

3.2 Properties of ferrimagnetic films

Major parts of this Section 3.2 were published in [101] under the CC BY 4.0 license and have been reproduced with permission of the coauthors and in accordance with the publisher's policy.

In order to develop a useful model for ferrimagnetic films simulation results have to be compared, validated and adjusted to experimental data if necessary. Collaborators at the Paul Scherrer Institute (PSI) in Switzerland provided the needed experimental data. Amorphous $\text{Fe}_{64}\text{Gd}_{36}$ thin film square elements were investigated by imaging in the Fresnel mode of a transmission electron microscope (TEM). The equilibrium state without an applied field shows the well-known four-domain flux closure pattern with in-plane magnetization. However, the vortex is displaced from the center of the square element and the domain walls are curved. In a reference measurement of a thin $\text{Ni}_{81}\text{Fe}_{19}$ element, the vortex core is perfectly centered and the domain walls straight. When an increasing external field is applied in-plane, the vortex core can be moved. While the displacement of the vortex core increases linearly with the applied field in NiFe elements, in the ferrimagnetic FeGd squares the vortex core moves by sudden jumps. By just using random anisotropy and a patchy microstructure in the model for ferrimagnetic films we can reproduce the measured results in our simulation. The Simulation of amorphous films composed of patches with varying intrinsic magnetic properties was originally introduced by Mansuripur *et al.* [84, 87, 50], in order to describe domain wall processes in magneto-optical recording media.

In the following I will describe briefly the experimental method of this investigations in Section 3.2.1 and the used micromagnetic model in Section 3.2.2. Afterwards the results are compared and discussed in Section 3.2.3.

3.2.1 Fresnel imaging of domain patterns

The here described experimental work was done by Eugenie Kirk, Phillip Wohlhüter, Elisabeth Müller and Laura Heyderman at the Paul Scherrer Institute, Switzerland.

Amorphous $\text{Fe}_{64}\text{Gd}_{36}$ thin film was deposited at different thickness by ultra high vacuum (UHV) magnetron sputtering. The film was patterned into square elements of edge lengths ranging from 3 to 10 μm by electron beam lithography and subsequent lift-off. For reference measurements Permalloy (Py, $\text{Ni}_{81}\text{Fe}_{19}$) squares of edge length 10 μm and thickness 15 nm were fabricated.

The specimens were imaged by Lorentz microscopy in a transmission electron microscope (TEM) in the Fresnel mode [62]. This method is based on the interaction between the electron beam and the magnetic field \mathbf{B} of the measured sample in the presence of an electric field \mathbf{E} . The electrons of charge q moving with the velocity \mathbf{v} through the field experience the Lorentz force \mathbf{F}_L and get deflected:

$$\mathbf{F}_L = q\mathbf{E} + q\mathbf{v} \times \mathbf{B} \quad (3.12)$$

Since the deflection angle also depends on the in-plane magnetization of the sample the domains of different magnetization can be detected. In the Fresnel mode an over- or under-focusing is used to reveal the domain walls of the sample. The domain

patterns of the square elements were imaged in remanent state without any external field.

In order to investigate the vortex motion an increasing external in-plane field was applied. The vortex position is tracked as a function of the applied field, which is created by the remanent field of the TEM objective lens. Tilting the sample inside the objective lens field results in increased in-plane fields. At zero tilt, the in-plane component of the magnetic field is minimal, which is reflected by a center position of the vortex in NiFe. On increasing the tilt, and thus the applied magnetic field, the vortex is displaced from the center (see Figure 3.4 and Fresnel images in Figure 3.5).

3.2.2 Model for ferrimagnetic films

Distorted flux closure patterns as seen in the measurements described in the previous Section 3.2.1 have been investigated in the past and possible sources have been isolated. Dietrich *et al.* [21] found curved domain walls in Permalloy squares which they attributed to a curvature of the sample surface. Also an interfering magnetic field as created by the tip of a magnetic force microscope can induce twisted flux closure patterns [38]. Hertel and co-workers [54] show that the demagnetizing field of nano-islands with inclined surfaces cause asymmetric domain patterns. Heyderman *et al.* [55] also reported asymmetric domain configurations for Ni₈₃Fe₁₇ and Co elements when decreasing the thickness to below 17 nm. They attributed the observed patterns to material defects such as edge and surface roughness, but also local magnetocrystalline anisotropy which serve as local pinning sites for domain walls and vortices.

Giles *et al.* suggested in [42] real amorphous rare earth-transition metal alloys show increased coercivity, probably due to spatial fluctuations of magnetic properties and material inhomogeneities. For their micromagnetic model also used in [41, 88], in order to become effective, these properties have to be distributed over patches with at least the size of the domain wall width. This structural property might be attributed to a still existing near-range order in the amorphous material. By means of the patchy structure, they introduced a structural correlation length into their micromagnetic model. Within a patch, which can have arbitrary shape, the direction of the local anisotropy was assumed constant.

Fu and co-workers [36] showed that the critical field for the nucleation of reversed domains strongly depends on the patch size, whereas the pinning field of domain walls depends on the patch-to-patch easy axis orientation. They emphasize that the nanoscale patches result from local variations of the intrinsic magnetic properties and are different from microstructural features as for example columnar structures or polycrystalline grains. Nucleation fields and domain wall pinning fields computed with the assumption of random anisotropy fluctuation compare well with experimental data.

Based on these findings spatial distributions of the magnetocrystalline anisotropy axis and anisotropy constant are incorporated into the model. Therefore these two parameters, defining the anisotropic field in equation (3.11), are functions of space and become $\mathbf{k} = \mathbf{k}(\mathbf{x})$ and $K_u = K_u(\mathbf{x})$. The thin film model is divided into patches p_i to allow the introduction of inhomogeneities (see Figure 3.2). Both anisotropic properties are randomly and independently distributed across these patches. This means that every patch p_i has its own \mathbf{k}_i and $K_{u,i}$. In order to model these patches a three-dimensional tetrahedron finite-element mesh is used. It is created by the software package *Neper* [114], which employs *Gmsh* [39] as its finite-element-mesh generator. This software allows to create the patches by using Voronoi-tessellation.

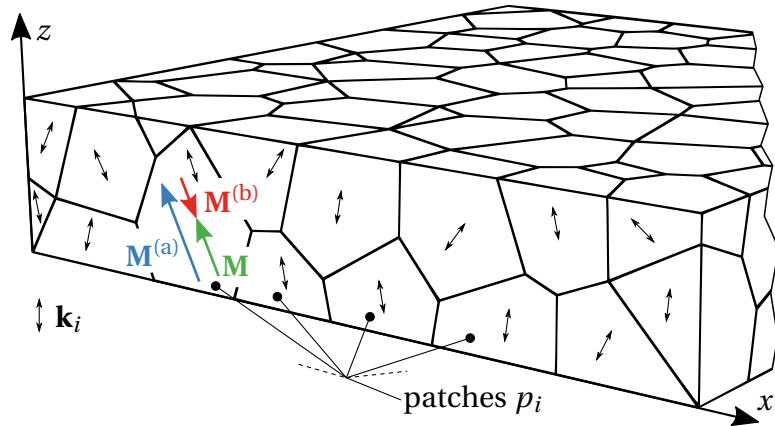


Figure 3.2: Part of a geometric model for a ferrimagnet with patches p_i to model inhomogeneities and their respective anisotropic easy axis \mathbf{k}_i .

It remains to choose the size of the patches. In the paper of Mansuripur *et al.* [88] the simulations were done on a 2D-model with an area A^{FI} and a certain number of patches n_p . The mean patch size \bar{s}_p can be defined as the diameter of a circle with an area equal to the mean area of the patches as in (3.13).

$$\bar{s}_p = \sqrt{\frac{4}{\pi} \frac{A^{\text{FI}}}{n_p}} \quad (3.13)$$

Therefore, the patch sizes for rare earth transmission metals in their work were set in the range of 7 to 15 nm. In this thesis however, 3D-models with volume V^{FI} are used and therefore the patch size is defined by the diameter of a sphere with equal volume to the mean volume of the patches \bar{V}_p as in (3.14).

$$\bar{s}_p = \sqrt[3]{\frac{6}{\pi} \frac{V^{\text{FI}}}{n_p}} \quad (3.14)$$

In Figure 3.2 a ferrimagnetic phase with a mean patch size of $\bar{s} = 13$ nm is depicted.

The deviation of \mathbf{k}_i from the z -axis is limited by a maximum angle of θ_{\max} which can be set from 0 to $\pi/2$. Since this angle defines a cone with the z -axis as its center it is also sometimes referred to as a cone angle. Hence, a cone angle of 0 would mean that the magneto-crystalline anisotropic easy axis of each grain of the model is perfectly aligned with the z -axis (film normal). In this thesis, when dealing with thin films, this is equal to all easy axes pointing out-of-plane. On the other end with $\theta_{\max} = \pi/2$ the easy axes are pointing in random directions yielding a film with no globally preferred direction. Also the magnetic anisotropy constant varies following a Gaussian distribution with a relative standard deviation σ_K across patches p_i . Apart from the anisotropy no other intrinsic properties differ from patch to patch.

3.2.3 Validation of the ferrimagnetic model

The remanent Fresnel images of the specimens show the well-known four-domain flux closure pattern. However, in thin ferrimagnetic specimens, for example the 20 nm $\text{Fe}_{64}\text{Gd}_{36}$ square in Figure 3.3 [b](#), it can be seen that the vortex is displaced from the center of the square element and the domain walls are curved. In the reference measurement on 15 nm thick $\text{Ni}_{81}\text{Fe}_{19}$, the vortex core is centered as expected and the domain walls are almost straight (Figure 3.3 [a](#)) as seen in the work of Lau *et al.* [\[77\]](#). Further measurements revealed that with increased thickness of the FeGd squares the vortex core moves towards the center of the square and therefore closer to the ideal symmetric pattern.

In the micromagnetic simulations continuous elements without structural features are compared to patchy elements. For the ease of computation the lateral extension of the square elements was reduced. Geometric models were generated for 20 nm thick elements with edge lengths of 100 nm, 300 nm and 600 nm and divided into patches with a mean size of $\bar{s} = 13$ nm. The saturation polarization was set to $J_s = 1$ T and the exchange stiffness constant to $A_x = 10$ pJ/m. The easy axes of each patch was set to a random angle in the range from 0 to $\theta_{\max} = \pi/2$. The patchy element was given a mean magnetocrystalline anisotropy of $\bar{K}_u = 0.1$ MJ/m³ with relative standard deviation of $\sigma_K = 20\%$ across the patches. The mean anisotropy field assigned to the patches of the micromagnetic model corresponds to the experimentally measured field in $\text{Fe}_{64}\text{Gd}_{36}$ [\[143\]](#).

The continuous film was modeled with zero magneto-crystalline anisotropy. The exchange constant and the magnetization of this film match the values for NiFe. The uniaxial anisotropy of NiFe is essentially zero unless the film shows a stress induced magneto-elastic anisotropy. In FeGd structural randomness is more important than in Permalloy because the magneto-crystalline anisotropy in FeGd is much higher than in Permalloy. Basically for the continuous reference calculation we take the finite element mesh but remove the spatial inhomogeneities by setting the magneto-

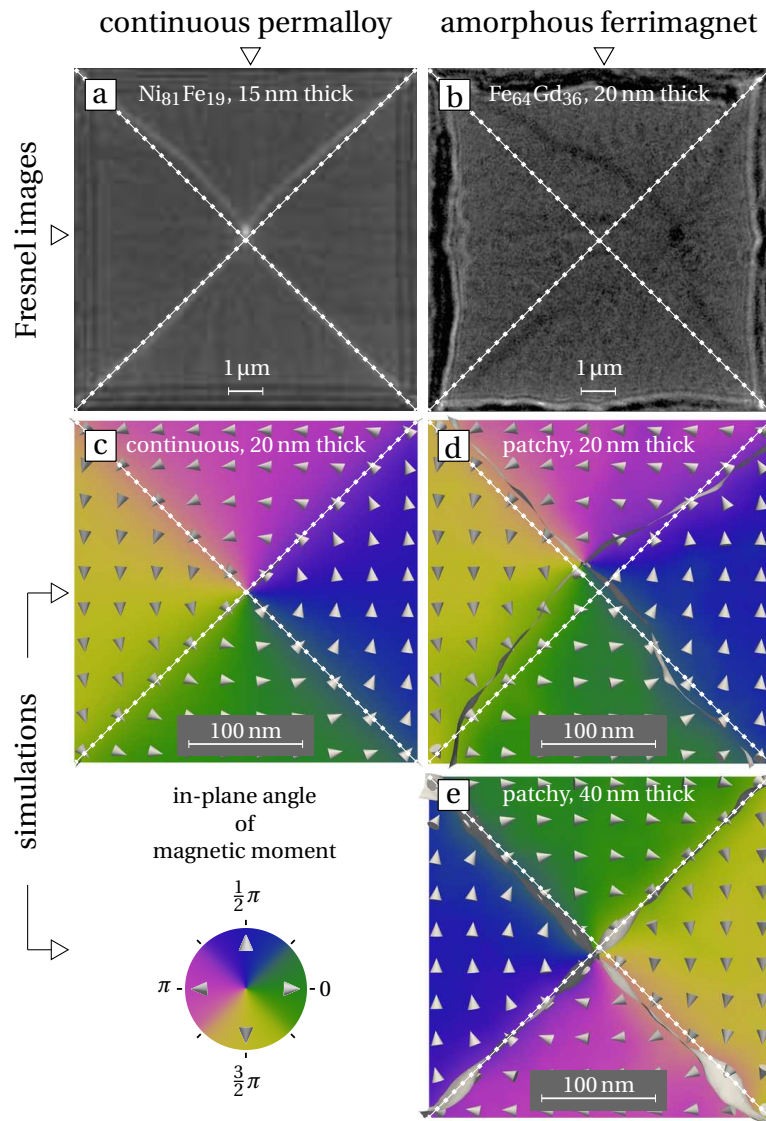


Figure 3.3: The remanent domain pattern of a Permalloy square shows an ideal flux-closure pattern and straight domain walls in the TEM image **a** and also in the simulation **c**. The ferrimagnetic $\text{Fe}_{64}\text{Gd}_{36}$ squares show a displaced vortex core and curved domain walls in the measurement **b** as well as in the simulation with a patchy microstructure **d**. When the thickness of the simulated element is doubled **e** the vortex core is centered again, but the randomness can still be recognized by the twist in the domain walls. The measured figures **a** and **b** are courtesy of E. Kirk and E. Müller, Paul Scherrer Institute.

crystalline anisotropy constant to zero. In this way the effect of the modeled patches can be investigated by comparison. For convenience an overview of the used material parameters is given in Table 3.1.

Table 3.1: Properties for continuous Permalloy and ferrimagnetic element: Exchange coupling stiffness A_x , mean anisotropy constant \bar{K}_u , rel. standard deviation of anisotropy constant σ_K , maximal deviation angle of the easy axis θ_{\max} , saturation polarization J_s and mean patch size \bar{s} .

Material	A_x (pJ/m)	\bar{K}_u (kJ/m ³)	σ_K (%)	θ_{\max} (°)	J_s (T)	\bar{s} (nm)
Py (Ni ₈₁ Fe ₁₉)	10	0	0	0	1	-
FI (Fe ₆₄ Gd ₃₆)	10	100	20	90	1	13

After initializing each mesh node with random magnetization the equilibrium state is computed by letting the system relax for 4 ns without an applied external field. The square elements with 100 nm edge length were too small to form a four-domain pattern and relaxed to either a C- or S-state [116], regardless of the patchy inhomogeneities. With the chosen magnetic properties the 300 nm squares are big enough to hold a four-domain flux closure pattern. In Figure 3.3 the relaxed equilibrium states of 300 nm squares are compared to the measurement. The white dotted lines are a guide to the eye to mark the ideal four-domain flux closure pattern. The domain walls in the simulations are shown as gray ribbons and the magnetic moments as gray arrows. The in-plane angle of the magnetic moments is represented according to the color-map.

The square without the patchy microstructure in Figure 3.3[c] shows an almost perfect four-domain flux closure pattern with the vortex core in its center as expected. When the patches are introduced in Figure 3.3[d] the random inhomogeneities cause an asymmetric flux closure pattern with an off-center vortex core and curved domain walls. By doubling the thickness of the sample to 40 nm the vortex core is almost centered again (Figure 3.3[e]). The domain pattern is therefore symmetric again but the randomness can still be seen in the twisted domain walls. This behavior may be attributed either to the increased magnetostatic energy in the thicker square or to averaging of the anisotropy fluctuations throughout the thickness of the sample. However, so far the calculations are in good qualitative agreement with the experimental findings in Figure 3.3[a] and Figure 3.3[b].

Starting from the remanent state an increasing external in-plane field is applied. In the TEM this can be done by tilting the sample inside the objective lens field. At zero tilt, the in-plane component of the magnetic field is minimal, which is reflected by a center position of the vortex in the remanent state of NiFe. Tilting the sample inside the objective lens field results in increased in-plane fields. With increasing in-plane

field the vortex core can be moved due to the growth of the magnetic domain parallel to the field. This allows to observe the vortex core movement away from its original position.

The vortex in a material with little pinning such as NiFe is displaced reversibly with the applied field. In case of ferrimagnetic $\text{Fe}_{64}\text{Gd}_{36}$, the behavior is more complex. The top graph in Figure 3.4 shows the displacement of the vortex core relative to the starting point in a $3\mu\text{m} \times 3\mu\text{m}$ FeGd square with a thickness of 50 nm.

The vortex position is tracked as a function of applied in-plane field given as a fraction of the remanent field of the TEM objective lens. Starting from the equilibrium state at zero field the vortex core displacement is exponential until it gets pinned at a relative field of 0.06 (red curve). At around 0.09 the vortex gets depinned and moves on linearly. When the external field is decreased again (blue curve) the pinning/depinning events can be observed in the same field range. The vortex displacement between 0.06 to 0.1 is hysteretic.

The simulation starts from the field-less equilibrium state computed previously. An increasing external in-plane field is applied to observe how the vortex core gets pushed away from its original position. In the bottom diagram of Figure 3.4 the resulting magnetization curve (red solid line) is plotted against the applied field. Similar to the measured vortex displacement, a sudden jump of the magnetization is observed in the simulation between labels [b] and [c]. When the applied field after the depinning in [c] is reduced again, a hysteresis loop is observed (blue dashed line).

The two diagrams in Figure 3.4 cannot be compared directly since they show different parameters. However, the magnetization M_y shown in the simulated curve of the bottom diagram is related to the vortex position. For both, the experimental and the simulated vortex movement, four magnetization states are depicted in Figure 3.5. The domain patterns during the application of the increasing external field can be seen: On the left hand side the simulated domain configuration and in the right hand column the measured Fresnel images. An applied field parallel to the yellow domain is applied which pushes the vortex core away from its original position. The labels [a] to [d] in Figure 3.5 correspond to those in Figure 3.4. Depinning happens between the labels [b] and [c] in the simulation and between [c] and [d] in the experiment. Of course, again the comparison is only qualitatively since the edge length of the squares differ by an order of magnitude.

In the experimental measurements it was observed, that with increasing element size the simple four domain states could be found less often. Instead the domain patterns got more complex with multiple vortex cores pointing in both out-of-plane directions. In Figure 3.6 [a] the computed remanent state of a patchy square element with an edge length of 600 nm is shown. Similar to the measured remanent states of larger ferrimagnetic squares, the domain pattern is more complex with multiple vortices. One of many Fresnel images is shown in Figure 3.6 [b] with an edge length

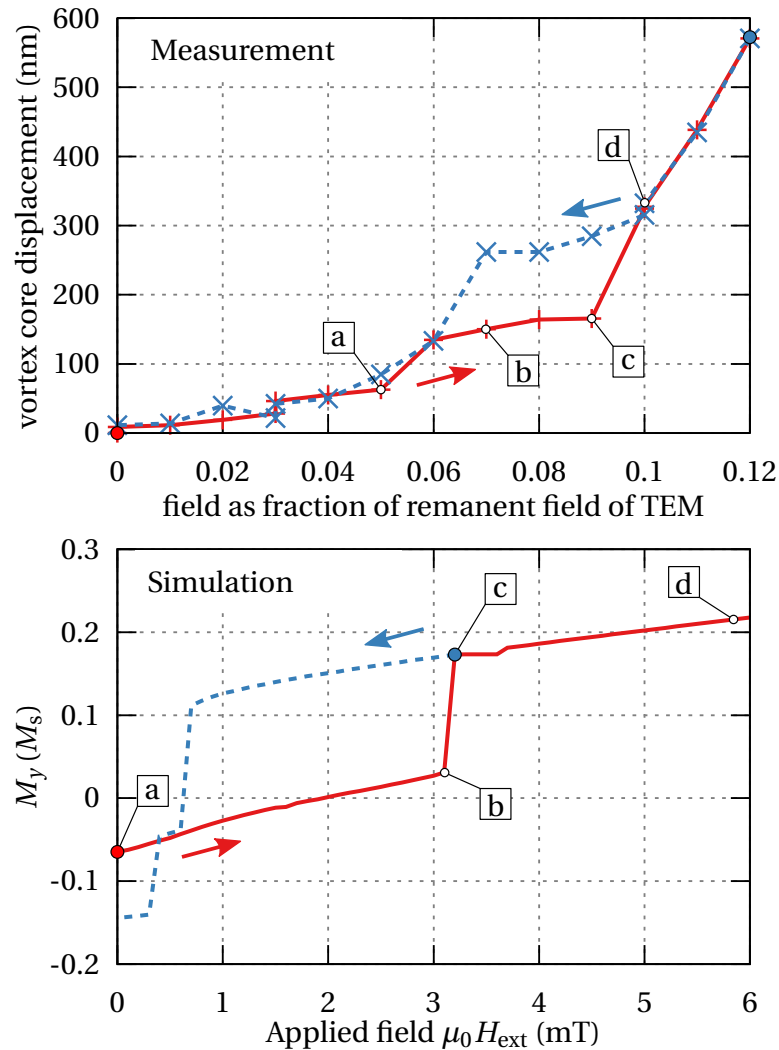


Figure 3.4: Experimentally measured (top) and simulated (bottom) vortex core movement in an $\text{Fe}_{64}\text{Gd}_{36}$ square element when applying an increasing in-plane field (solid red) and decreasing the field to zero again (dashed blue). The labels in both diagrams correspond to those in Figure 3.5. The shown displacement is orthogonal to the applied field direction. The edge length and thickness are $3\ \mu\text{m}$ and $50\ \text{nm}$ for the measured square element and $0.3\ \mu\text{m}$ and $20\ \text{nm}$ for the simulated element respectively. The measured data was kindly provided by P. Wohlhüter, Paul Scherrer Institute.

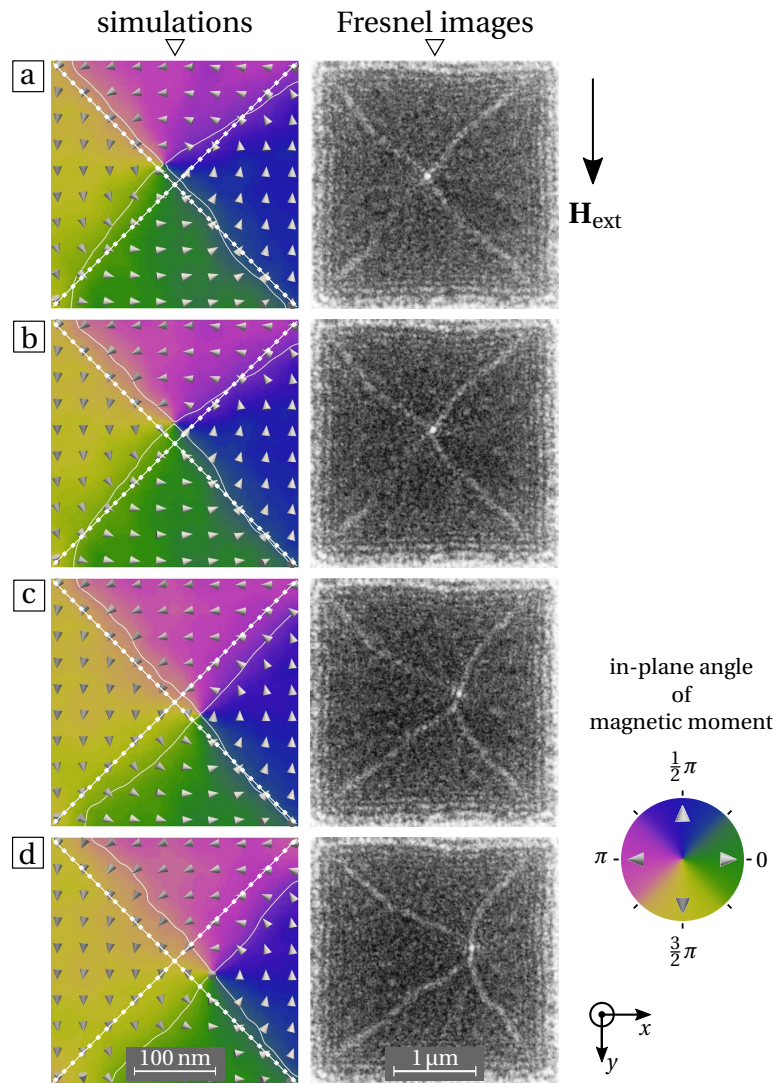


Figure 3.5: Calculated (left) and measured (right) stages (a to d) of flux closure patterns in ferrimagnetic square elements when applying an increasing external field. The left and right images do not experience the same field but share the same label a to d which correspond to the respective graph in Figure 3.4. The measured TEM images are courtesy of E. Kirk, A. Weber and E. Müller, Paul Scherrer Institute.

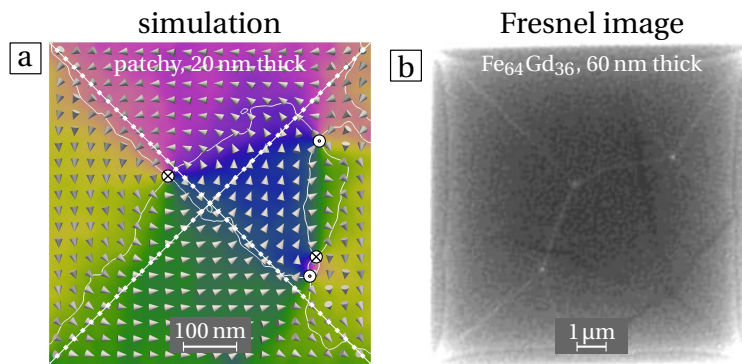


Figure 3.6: With increasing size of the square element, the domain patterns get more complex in the simulation with 600 nm edge length [a] as well as in the experiment with 10.8 μm edge length [b]. Both show multiple vortices with their cores pointing in both out-of-plane directions. The measured figure on the right hand side was kindly provided by E. Kirk, A. Weber and E. Müller, Paul Scherrer Institute.

of 10.8 μm . At this size less than half of the measured specimens show a four-domain pattern, most show different variants with two or more vortices.

Using micromagnetic simulations and considering anisotropic inhomogeneities in the amorphous ferrimagnetic thin square elements, five features observed in the Fresnel measurements could be reproduced:

- off-centre position of the vortex core at equilibrium without applied field
- with increasing thickness the displacement of the vortex core from the centre is reduced
- curved domain walls without applied field
- the domain patterns get more complex with increasing size of the square elements
- non-linear vortex core movement when applying an in-plane field

So far elements with in-plane magnetization at remanent states or with applied external field in in-plane direction were simulated. The results match the experiments very well. In the following section the established micromagnetic model will be used on thin films with out-of-plane anisotropy.

3.3 Magnetization reversal and domain wall motion

In order to gain comparable results to experiments, a model based on the heterostructures measured by Schubert *et al.* [130] is developed. In their work, among other compositions, a ferrimagnetic, amorphous thin film of Fe₈₁Tb₁₉ alloy was investigated. For the following micromagnetic calculations, the intrinsic properties at a temperature of $T = 70$ K are taken.

A geometrical model of $100 \text{ nm} \times 100 \text{ nm} \times 20 \text{ nm}$ with 120 patches and an average patch diameter of 13 nm is generated. With an average magnetocrystalline anisotropy constant of $\bar{K}_u = 889 \text{ kJ/m}^3$ the ferrimagnetic film is relatively magnetically hard. The anisotropy constant varies across the patches with a standard deviation of $0.2\bar{K}_u$. The easy axes are randomly misaligned within a cone angle of $\theta_{\max} = \pi/4$ and therefore preserve an overall out-of-plane anisotropy. The saturation polarization at $T = 70$ K is $J_s = 135 \text{ mT}$ and the exchange stiffness constant is assumed to be $A_x = 1 \text{ pJ/m}$. The values are summarized in Table 3.2.

Table 3.2: Properties of ferrimagnetic layer at $T = 70$ K investigated in [130].

Material	A_x (pJ/m)	\bar{K}_u (kJ/m ³)	σ_K (%)	θ_{\max} (°)	J_s (mT)	\bar{s} (nm)
FI (Fe ₈₁ Tb ₁₉)	1	889	0.2	45	135	13

The model is fully magnetically saturated in positive z -direction, *i.e.* out-of-plane direction, in its initial state. By applying an opposing external field \mathbf{H}_{ext} the magnetization reversal curve is computed. In the simulations we are only interested in the static hysteresis behavior. Therefore we use an effective damping constant of $\alpha_{\text{eff}} = 1$ and change the external field at the rate of 27 mT/ns .

Due to limited computation resources the model size is limited and prevents the simulation of the whole film investigated in the experimental work. The relatively small size of only 100 nm edge length results in a nucleation driven reversal process. This does not resemble the reality, because in the experiment the reversal shows a lateral movement of a domain wall. For this reason we start our simulations with an artificially set domain wall in the center of the model in order to study the reversal by domain wall motion.

The simulation of the ferrimagnetic layer shows now a lateral movement of the domain wall. This movement is governed by pinning processes at the patch boundaries. Pinning is caused by the variation of anisotropic properties across the patches as described in Section 3.2. The spatial variation of the magnetic anisotropy constant $K_u(\mathbf{x})$ gives rise to energy barriers against domain wall motion at patch interfaces. In Figure 3.7 three snapshots of the domain wall movement are depicted. The domain

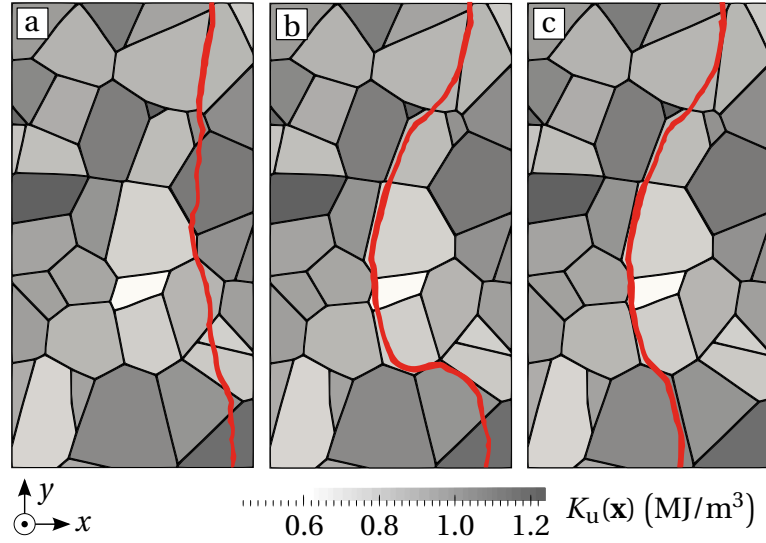


Figure 3.7: Lateral domain wall (red) movement in a ferrimagnetic film governed by pinning processes with an applied increasing out-of-plane field. The pinning is determined by the distribution of $K_{u,i}$ across the patches. Domain wall reversibly moved from the initial state **a**, pinning at patches with increased $K_{u,i}$ **b** and depinning in the lower area of **c** are shown. The values of the external field for the domain wall positions **a**, **b** and **c** can be read from the computed magnetization curve shown in Figure 3.8

wall is drawn on a x - y -slice through half of the ferrimagnet which is colored by $K_u(\mathbf{x})$. The darker the patch appears the higher is its $K_{u,i}$ value.

After artificially setting the domain wall, the system is allowed to relax for 2 ns (Figure 3.7 **a**) before an external field is applied in z -direction. With increased field in Figure 3.7 **b** the domain wall gets pushed through patches with weaker anisotropy (lightgrey) in the center and stops at the repulsive barrier of patches with increased $K_{u,i}$ (darkgrey). The domain wall stays pinned at patch boundaries in the upper and lower region of the slice.

This situation is similar to domain wall pinning in a two-phase system being composed of a hard- and soft-magnetic phase, when the pinning field is proportional to the difference of the magnetocrystalline anisotropy of both phases [70, 71]. The repulsive patch can be seen clearly at the bottom region of Figure 3.7 **b**, whereas the top part of the domain wall is pinned at a patch outside the presented x - y plane and therefore invisible. By further increasing the external field, the domain wall is pushed against the repulsive patch at the bottom. When the pinning field $H_p = \Delta K_u / (2\mu_0 M_s)$ [70] is reached, the domain wall spontaneously moves through this

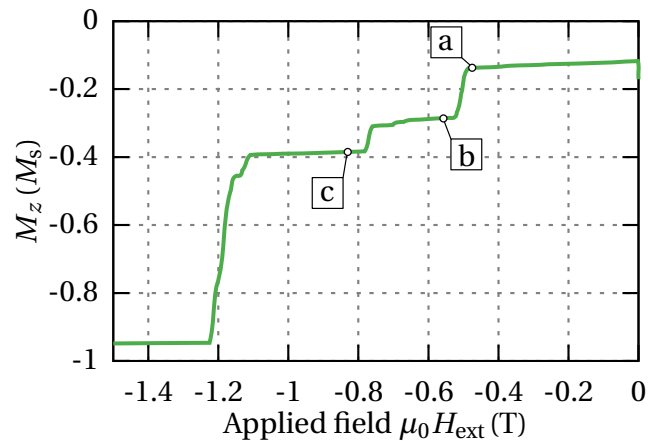


Figure 3.8: Pinning and depinning events on the demagnetization curve of a ferri-magnetic layer. More than half of the layer is already artificially reversed before the negative external field is applied. The labels **a**, **b** and **c** mark the three states depicted in Figure 3.7.

patch and pins at the next repulsive patch boundary (Figure 3.7 **c**). Each pinning process can be observed as a sudden drop in the magnetization reversal curve in Figure 3.8.

3.4 Summary

In this chapter we described the micromagnetic model for ferrimagnetic films according to Mansuripur [85] which we implemented in the 3D finite element micromagnetic package FEMME. Spatial fluctuations of magnetic properties were incorporated in the model by dividing the film into patches and assigning each patch a random anisotropy constant and easy axis. This structural property might be explained by a still existing near-range order in the amorphous material [41].

By using this model, in-plane domain patterns in thin ferrimagnetic $\text{Fe}_{64}\text{Gd}_{36}$ square elements were investigated and compared to measured elements. An in-plane external field was applied to these elements to investigate the movement of the vortex core. The patchy model proves to be successful in reproducing five features that were seen in the measured Fresnel images: 1) four-domain flux closure pattern with an off-center vortex core and 2) curved domain walls at remanent state, 3) with increasing thickness the displacement of the vortex core from the center is reduced, 4) the domain patterns get more complex with increasing size of the square elements and 5) a non-linear vortex core movement when an increasing in-plane field is applied. This shows

that the presence of randomness in the magnetocrystalline anisotropy creates pinning sites for domain walls and vortex cores.

In a next step the patchy model was used to investigate the reversal of a ferrimagnetic $\text{Fe}_{81}\text{Tb}_{19}$ thin film with an increased out-of-plane anisotropy. The magnetic properties were taken from the work of Schubert *et al.* [130]. The simulations show a laterally moving domain wall which gets pinned and depinned at the patch boundaries. These pinning events manifest themselves as sudden drops in the demagnetization curve.

Ferri-/ferromagnetic heterostructures

Contents

4.1	Model for exchange coupled composites.....	53
4.2	Magnetization reversal.....	56
4.3	Domain wall motion	59
4.3.1	Domain wall pinning.....	60
4.4	Summary.....	62

Portions of this chapter were previously published in [103] under the [CC BY 4.0 license](#) and have been reproduced with permission of the coauthors and in accordance with the publisher's policy. Content which was not generated by the author of this thesis is explicitly denoted.

Exchange coupled composite films incorporating ferrimagnetic materials have been proposed for many different applications. Romer *et al.* [123] used a ferrimagnetic TbFe layer coupled to a ferromagnetic layer to create a large exchange bias field.

Yamada and his collaborators [158] experimentally showed the approach of using an exchange coupled magnetic capping layer on a ferrimagnetic layer (TbFeCo) to lower the required external field for magneto-optical recording. In contrast to the simulations in this thesis, the used capping layer had in-plane magnetization.

In experiments with strongly exchange coupled TbFe/FeCo multilayers, Armstrong *et al.* [6] revealed that demagnetization occurs by nucleation of a domain which extends through the entire layer-stack. A single twin wall is formed which moves until the whole sample is reversed. Contrary to the investigated model in this thesis, the layers are exchange coupled antiparallel and have an in-plane easy axis.

Antiferromagnetically exchange coupled ferri-/ferrimagnetic bilayers have been investigated by Mangin *et al.* [83]. In their work they identified the magnetic configuration at the interface as the determining mechanism for the exchange bias field.

A general micromagnetic model for exchange coupled bilayer systems was described by Oti [107]. He simulated laminated cobalt-alloy films used in longitudinal recording. The effect of media dimensions and interface exchange on magnetization at remanent and coercive states for two layers separated by a nonmagnetic phase were investigated. Both layers are modelled as an array of uniaxial volume elements and show an isotropic three-dimensional distribution of magnetocrystalline anisotropy axes.

Schubert and collaborators [130] experimentally investigated the interface exchange coupling of ferri-/ferromagnetic heterostructures with out-of-plane anisotropy. Their results revealed that an interfacial domain wall, which may be pinned at the interface between the ferrimagnet and the ferromagnet, greatly affects the demagnetization process.

Applications of heterostructures built on ferromagnetic and ferrimagnetic layers might be found in magnetic recording media with tailored switching behavior. The big advantage of ferrimagnetic materials is the ability to tailor their magnetic properties by their composition with respect to the desired working temperature [93]. In order to exploit these properties, a deeper understanding of ferrimagnetic materials as well as an investigation of the exchange coupling with ferromagnetic materials is necessary. Exchange coupled composites (ECC) of hard and soft-magnetic phases are used in perpendicular magnetic recording [141, 15, 81] and may benefit even more from tailored ferrimagnetic layers.

In the following sections the previously used model for the ferrimagnetic layer will be expanded by an exchange coupled ferromagnetic layer. The exchange energy at the interface between the two layers is computed and the exchange coupling fields acting on both layers at the interface are derived. By parametrizing the model to be close to a measured specimen in the work of Schubert *et al.* [130], the simulated reversal curves can be compared to experimental data. Using this model the reversal process and domain wall motion is investigated.

4.1 Model for exchange coupled composites

To simulate the ferri-/ferromagnetic heterostructures the model for ferrimagnetic films described in the previous Chapter 3 needs to be extended by the exchange coupled ferromagnetic layer. For the later investigated bilayer system collinear coupling between the two phases is used, but the following model can also be used for antiparallel coupling. The bilayer system with its ferrimagnetic phase Ω^{FI} , ferromagnetic phase Ω^{FM} and interface Γ is depicted in Figure 4.1.

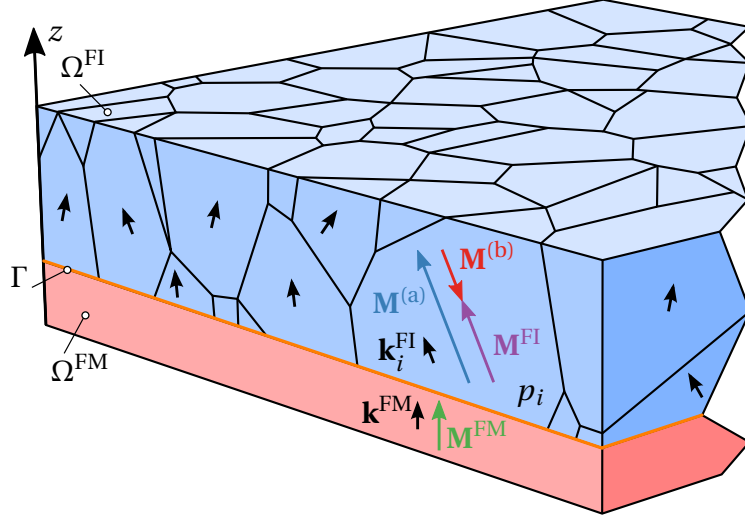


Figure 4.1: Geometric model of a bilayer system with a ferrimagnetic phase Ω^{FI} and a ferromagnetic phase Ω^{FM} connected at the interface Γ . The amorphous Ω^{FI} is separated in regions (patches p_i) with varying uniaxial anisotropic direction \mathbf{k}_i and anisotropic constant $K_{u,i}$. Ω^{FM} is a continuous phase with a weak out-of-plane uniaxial anisotropy \mathbf{k}^{FM} .

In order to model the exchange coupling at the interface, the effective exchange field from the ferrimagnetic layer $\mathbf{H}_{\text{ix}}^{\text{FI}}$ acting on Ω^{FM} and the effective exchange field from the ferromagnetic layer $\mathbf{H}_{\text{ix}}^{\text{FM}}$ acting on Ω^{FI} have to be taken into account. Therefore the equation for the effective fields of both layers, Ω^{FI} and Ω^{FM} , has to be extended as follows:

$$\mathbf{H}_{\text{eff}}^{\text{FI}} = \mathbf{H}_{\text{ext}} + \mathbf{H}_{\text{dmag}} + \mathbf{H}_{\text{ani}}^{\text{FI}} + \mathbf{H}_{\text{x}}^{\text{FI}} + \mathbf{H}_{\text{ix}}^{\text{FM}} \quad (4.1a)$$

$$\mathbf{H}_{\text{eff}}^{\text{FM}} = \mathbf{H}_{\text{ext}} + \mathbf{H}_{\text{dmag}} + \mathbf{H}_{\text{ani}}^{\text{FM}} + \mathbf{H}_{\text{x}}^{\text{FM}} + \mathbf{H}_{\text{ix}}^{\text{FI}} \quad (4.1b)$$

For the simulation both layers are separately represented by a three-dimensional tetrahedron finite-element (FE) mesh with a characteristic mesh size of 3 nm. Exchange coupling only effects spins within the exchange length (~ 2.5 nm, see Section 2.2.4), hence the interface exchange field acts only on the mesh nodes at the interface of the two layers. The interfacial exchange fields can be calculated by the variation of the interface exchange energy E_{ix} over the magnetic moment as given in (4.3).

$$\mathbf{H}_{\text{ix}}^{\text{FI}} = \mathbf{H}_{\text{ix}}^{\text{FM}} = 0 \quad \text{on} \quad (\Omega^{\text{FI}} \cup \Omega^{\text{FM}}) \setminus \Gamma \quad (4.2)$$

$$\left. \begin{aligned} \mathbf{H}_{\text{ix}}^{\text{FI}} &= -\frac{1}{\mu_0} \frac{\delta E_{\text{ix}}}{\delta \mathbf{M}^{\text{FI}}} \\ \mathbf{H}_{\text{ix}}^{\text{FM}} &= -\frac{1}{\mu_0} \frac{\delta E_{\text{ix}}}{\delta \mathbf{M}^{\text{FM}}} \end{aligned} \right\} \text{ on } \Gamma \quad (4.3)$$

The exchange energy across the interface is given by

$$\begin{aligned} E_{\text{ix}} &= -\mathcal{J} \sum_{i,j} S_i^{\text{FM}} S_j^{\text{FI}} \simeq -\frac{\mathcal{J} S^2}{a^2} \int_{\Gamma} \mathbf{m}_i^{\text{FM}} \mathbf{m}_j^{\text{FI}} d\Gamma \\ &= -J_{\text{ix}} \int_{\Gamma} \mathbf{m}_i^{\text{FM}} \mathbf{m}_j^{\text{FI}} d\Gamma \end{aligned} \quad (4.4)$$

where \mathcal{J} is the exchange integral, S_i^{FM} and S_j^{FI} are the respective spins, a is the distance of the spins in a simple cubic lattice and J_{ix} is the interface exchange coupling strength. In equation (4.4) the transition from a discrete spin model to a continuous description with the unit magnetization vectors \mathbf{m}_i^{FM} and \mathbf{m}_j^{FI} is made. In order to take into account the microstructural features of the ferrimagnet, as explained earlier in Section 3.2.2, the two layers have to be meshed separately. Hence the nodes at the interface of the two meshes do not match. This problem has been addressed in the study from Dean and his collaborators on antiferromagnetic/ferromagnetic bilayers [20] and therefore can be solved in the same manner. They employed a surface integral technique to restore the continuity at the interface and calculate E_{ix} using a symmetric Gaussian quadrature rule for triangles [28, 89].

To be able to compare the simulation results with experimental data, a model close to the $\text{Fe}_{81}\text{Tb}_{19}$ (20 nm) layer exchange coupled to a $[\text{Co}(0.4 \text{ nm})/\text{Pt}(0.8 \text{ nm})]_{10}$ multilayer stack from the work of Schubert *et al.* [130] was developed. The FeTb layer experimentally shows an out-of-plane anisotropy and represents the hard magnetic part of this bilayer system. This ferrimagnetic phase is modeled by a $100 \text{ nm} \times 100 \text{ nm} \times 20 \text{ nm}$ layer of 120 patches with an average diameter of 13 nm (Ω^{FI} in Figure 4.1). In this particular system the Co/Pt multilayer stack of the experiment is modelled as a 12 nm thick continuous, soft magnetic layer Ω^{FM} which is collinearly coupled to the ferrimagnet. The properties of both layers used for the simulations are listed in Table 4.1: the exchange constant A_x , the mean of local uniaxial anisotropy constants \bar{K}_u , the standard deviation of anisotropy constants across patches σ_K , the maximal deviation angle of the anisotropic easy axis from the out-of-plane axis θ_{max} , the effective saturation polarization $J_s = \mu_0 M_s$ and the average patch size \bar{s} . For comparison with the data from [130] the intrinsic properties are chosen at a temperature of $T = 70 \text{ K}$. The demagnetization curve at 70 K shows a well pronounced tail at a high external field. It will be shown that this tail can be attributed to a distribution of the interlayer coupling strength.

Table 4.1: Properties of ferri-/ferromagnetic heterostructure at $T = 70$ K investigated in [130].

Layer	A_x (pJ/m)	\bar{K}_u (kJ/m ³)	σ_K (%)	θ_{\max} (°)	J_s (mT)	\bar{s} (nm)
FM ([Co/Pt])	2	147	0	0	628	-
FI (Fe ₈₁ Tb ₁₉)	1	889	20	45	135	13

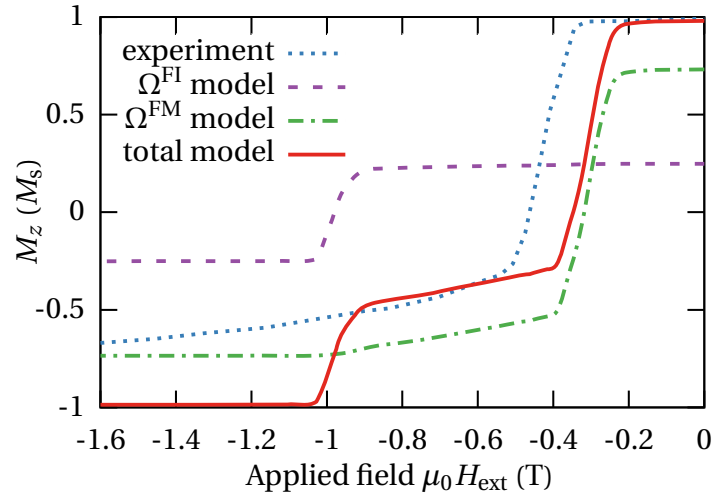


Figure 4.2: Computed reversal curves of the ferrimagnetic layer (dashed), the ferromagnetic layer (dot-dashed) and the overall bilayer system (solid) compared to the experimental measurement of Schubert *et al.* [130] at $T = 70$ K (dotted), all normalized by the total saturation magnetization M_s of the bilayer. The simulation was done with an interface exchange strength of $J_{\text{ix}} = 10$ mJ/m².

4.2 Magnetization reversal

By applying an out-of-plane external field \mathbf{H}_{ext} (parallel to the z -axis) the magnetization reversal curve of the bilayer system is computed. Because only the static hysteresis behaviour is needed, an effective damping constant of $\alpha_{\text{eff}} = 1$ is used. The external field is changed at the rate of 27 mT/ns, assuming an effective gyromagnetic ratio of $\gamma_{\text{eff}} = 0.63$ m/(sA) [85]. Figure 4.2 shows the computed reversal curve of both layers separately and in total, all normalized by the total saturation magnetization. Additionally the experimentally measured curve from [130] is drawn.

The soft magnetic Ω^{FM} phase starts to switch already at -0.25 T, but due to interface exchange coupling the reversal process gets stopped when the domain wall

reaches the interface. The reversed domain approaches the interface and the domain wall pushes through when eventually the Ω^{FI} phase switches at once at -0.9T .

While the switching of the soft magnetic phase and reversal process at the interface matches the experimental measurement very well, the simulated ferrimagnetic phase reaches its negative saturation at a much lower field than in the experiment. This disagreement can be identified as finite size effect of the simulation, since the small model size cannot correctly represent the effect of a distribution of the exchange coupling strength across the interface of the much bigger measured sample. This effect can be overcome by averaging over many computed magnetization reversal curves for the same model but with different values of the interface exchange coupling constant J_{ix} .

Simulations with 40 different J_{ix} were performed. The values of J_{ix} were distributed randomly. The optimum distribution was found by repeated calculations of the averaged demagnetization curve. The distribution was adjusted manually in order to reduce the squared distance between the experimental demagnetization curve and the computed curve.

The inset of Figure 4.3 shows the distribution that minimizes the squared distance of the computed hysteresis loop to the experimental one. The distribution is fitted by a Weibull-distribution (4.5), which is often used to describe particle size distributions.

$$f(J_{\text{ix}}; \lambda, k) = \frac{k}{\lambda} \left(\frac{J_{\text{ix}}}{\lambda} \right)^{k-1} e^{-(J_{\text{ix}}/\lambda)^k}, \quad \forall x \geq 0 \quad (4.5)$$

The best fit is obtained for $\lambda = 2.21$ and $k = 1.13$. Figure 4.3 shows the resulting average curve which reproduces the shape of the measured reversal curve.

The distribution is expected to change with temperature. Schubert *et al.* [130] show that the tail in the hysteresis loop changes with temperature and becomes longer with decreasing temperature. According to the model presented above, this would indicate that the width of the distribution increases with decreasing temperature. The fitted distribution shows that large portions of the interface area are weakly coupled and therefore favor the formation of an interface domain wall. Nucleation of patches in the ferrimagnetic layer occur first on those sites at the interface with strong exchange coupling. With increasing external field the reversal proceeds by pushing the domain wall in the ferrimagnetic phase from patch to patch towards full reversal. This lateral movement of the domain wall is similar to the movement seen in the previous Section 3.3.

Calculated minor reversal curves of the bilayer system are shown in Figure 4.4. The minor curves starting at -0.3T and -1.38T show that the switching of the ferromagnet is fully reversible. As soon as the domain wall has been pushed into the ferrimagnetic phase by the applied field, irreversible switching of the ferrimagnet occurs and the reversal curve does not go back to remanence. The same result has been observed

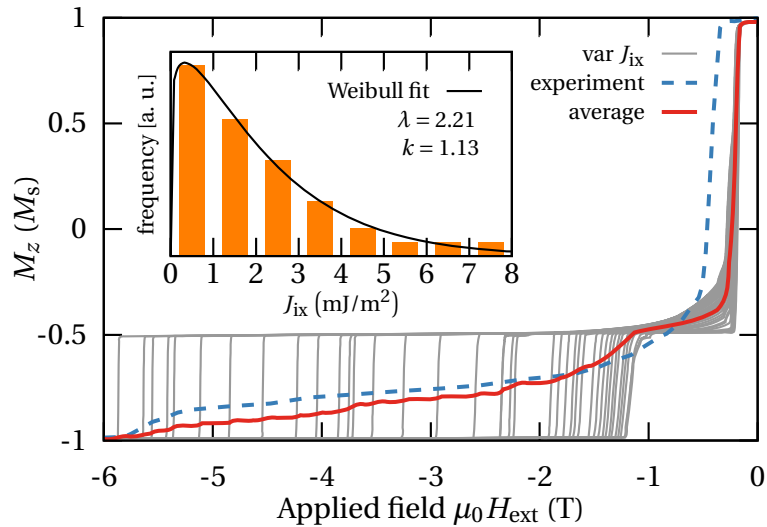


Figure 4.3: Averaged magnetization reversal curve (solid red line) of the bilayer system compared to the experimental measurement (dashed blue line) of Schubert *et al.* [130]. The average is computed over a variation of simulation runs (bright gray solid lines) with an J_{ix} - distribution shown in the inset.

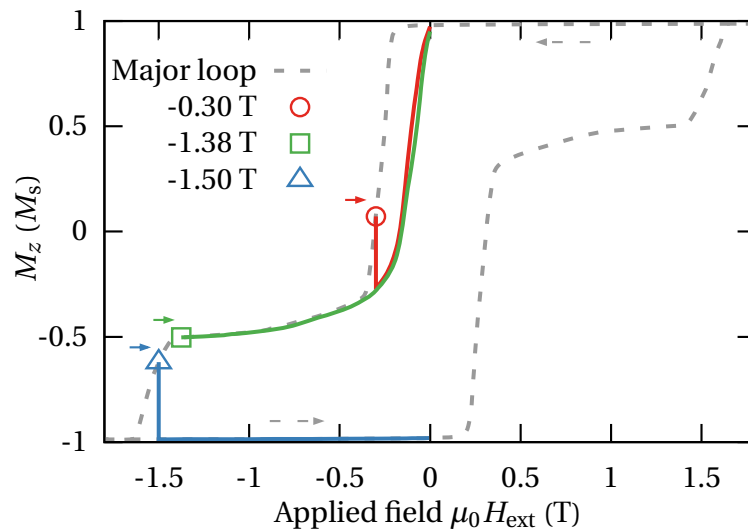


Figure 4.4: Minor reversal curves from a bilayer system with $J_{\text{ix}} = 14 \text{ mJ}/\text{m}^2$. The two magnetization configurations, \circ and \square , are fully reversible. The \triangle curve, which starts after nucleation in the ferrimagnet, shows a changed remanent state.

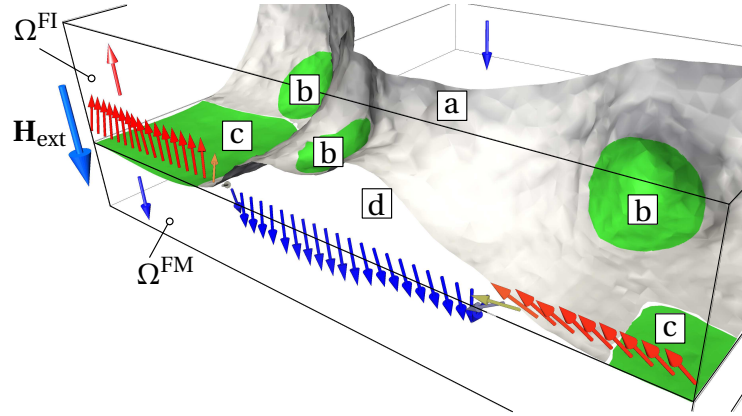


Figure 4.5: Snapshot during the magnetization reversal process showing the domain wall position (gray surface). The regions with arrows pointing downwards are already reversed whereas the regions with arrows pointing upwards are still not aligned with the external field \mathbf{H}_{ext} . The configuration of the domain wall in the ferrimagnetic phase is determined by pinning at patch boundaries **b** and pinning at the interface of the bilayer system **c**. Pinning sites are colored in green. Depinning from patch boundaries **a** and depinning from the interface **d** are both shown in the center of the Ω^{FI} phase.

in [130], but with intermediate states where the Fe/Tb layer is not fully switched. The absence of this states can again be attributed to the J_{ix} - distribution, as explained earlier in this section, which was not considered in these particular simulations.

4.3 Domain wall motion

By adding the ferromagnetic layer Ω^{FM} to the ferrimagnet Ω^{FI} , the reversal process gets more complex, hence the domain wall position should be visualized in three dimensions throughout the reversal process to investigate the partaking mechanisms. Due to the relatively small size of the bilayer model, the magnetization reversal is determined by the nucleation of the FI-layer. From the experiments in [130] it is known, that the reversal is governed by a lateral movement of a domain wall. Therefore, as in previous Section 3.3, an artificial domain wall is set-up by reversing half of the bilayer at the initial state to skip the nucleation field. After the simulation is started, the system is allowed to relax to its remanent state. Then an increasing external out of plane field \mathbf{H}_{ext} is applied to reverse the whole model. In this way, the movement of the domain wall can be observed in the remaining half of the model. A snapshot of this bilayer system during reversal is shown in Figure 4.5.

The domain wall is depicted as a grey surface in the Ω^{FI} phase and splits the bilayer system in an already reversed region and a region which is still not reversed. The reversed regions are denoted by the arrows aligned with the external field \mathbf{H}_{ext} . The anterior part of the Ω^{FI} is still not reversed and is marked by arrows pointing upwards, antiparallel to \mathbf{H}_{ext} . With the applied increasing field, the domain wall motion is determined by pinning and depinning. Pinning occurs at two locations (green areas in Figure 4.5): at patch boundaries [b] and at the interface between the ferrimagnet and the ferromagnetic layer [c]. The external field exerts a force on the domain wall. In regions without a pinning site the domain wall is pushed further, which leads to bowing of the wall. This is clearly seen at [a] inside the ferrimagnet and at [d] where the wall breaks away from the interface between the ferrimagnet and the ferromagnet. In the bilayer system the exchange coupled ferromagnetic layer helps the reversal by pushing the interface domain wall upwards into the ferrimagnetic phase [d].

4.3.1 Domain wall pinning

Pinning and depinning is the main mechanism governing the magnetization reversal. The pinning field H_p at the interface between the hard ferrimagnetic layer FI and the soft ferromagnetic layer FM can be calculated by [70, 141]

$$H_p = \frac{2K_u^{\text{FI}}}{J_s^{\text{FI}}} \frac{1 - \varepsilon_K \varepsilon_A}{(1 + \sqrt{\varepsilon_J \varepsilon_A})^2}, \quad (4.6)$$

where

$$\varepsilon_K = \frac{K_u^{\text{FM}}}{K_u^{\text{FI}}}, \quad \varepsilon_A = \frac{A_x^{\text{FM}}}{A_x^{\text{FI}}} \quad \text{and} \quad \varepsilon_J = \frac{J_s^{\text{FM}}}{J_s^{\text{FI}}}. \quad (4.7)$$

When the external field reaches H_p the domain wall gets pushed into the harder ferrimagnetic layer. Since the uniaxial anisotropy constant K_u^{FI} varies across patches, the pinning field varies across the interface and the domain wall depins from the interface into patches with weaker anisotropy first. With increasing external field the domain wall also moves into patches with higher K_u^{FI} .

The pinning of the domain wall inside the ferrimagnetic layer at the patch boundaries is also determined by the anisotropic properties of the patches. In order to assess the effect of the anisotropic properties, the magnetization reversal curves of bilayers with varying standard deviation of the uniaxial anisotropy constant σ_K^{FI} and cone angle of the anisotropic easy axis $\theta_{\text{max}}^{\text{FI}}$ are computed. Again, an artificial domain wall is set in the center of the bilayer to observe pinning and depinning of the domain wall. The parameter σ_K^{FI} is varied between 0 and \bar{K}_u^{FI} and $\theta_{\text{max}}^{\text{FI}}$ is varied between 0 and 45°. It is especially pointed out here, that the mean anisotropic constant $\bar{K}_u^{\text{FI}} = 889 \text{ kJ/m}^3$ is

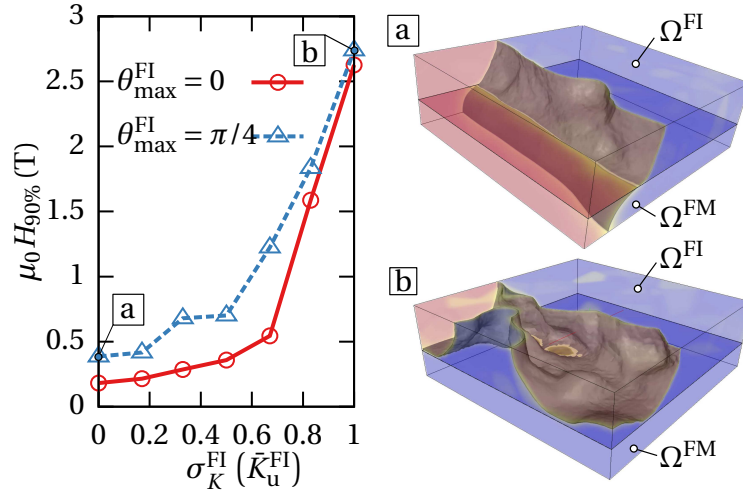


Figure 4.6: Effect of cone angle $\theta_{\max}^{\text{FI}}$ and distribution of uniaxial anisotropy constant σ_K^{FI} on domain wall pinning and consequently the switching field. $H_{90\%}$ is defined as required field to demagnetize the FI-layer to 90% of its the saturation magnetization M_s^{FI} . The two images at the right hand side show snapshots during domain wall movement. The gray surface is the domain wall in the FI (top) and FM (bottom) layer and splits the sample in regions with magnetization pointing up (red) and down (blue). \circ : perfectly aligned sample with perpendicular anisotropy, \triangle : deviation angles of anisotropy easy axes are homogeneously distributed between 0 and 45° .

kept equal across all the simulations, only its standard deviation σ_K^{FI} is varied. The deviation angle of the easy axes with respect to the out-of-plane axis are homogeneously distributed between 0 and $\theta_{\max}^{\text{FI}}$. The remaining parameters are chosen as listed in Table 4.1. For each parameter set five simulations are performed with different random easy axes and K_u^{FI} for the patches within the respective distribution parameters. This allows to combine the resulting demagnetization curves into an average curve per parameter set.

Since half of the bilayer is already switched at the initial state in this simulation set-up, a coercive field can not be used as a measure to compare the different results. Hence, the applied field when 90% of the harder FI-layer is switched is taken as a measure, *i.e.* $H_{90\%} := H_{\text{ext}}(M_z^{\text{FI}} = 0.9M_s^{\text{FI}})$. Figure 4.6 shows this switching fields $H_{90\%}$ for $\theta_{\max}^{\text{FI}} = 0$ and $\pi/4$ plotted against the standard deviation of the uniaxial anisotropy constant σ_K^{FI} . The values are the average over five simulation runs.

Due to lack of pinning sites in the ferrimagnetic layer, when $\sigma_K^{\text{FI}} = 0$ and $\theta_{\max}^{\text{FI}} = 0$, the domain wall moves laterally through the bilayer. The domain wall in the harder FI-layer closely follows the wall in the soft ferromagnetic layer. Therefore also pinning at the interface is not observed. The only energy needed to reverse the bilayer is the

energy to push the domain wall further without any blocking pinning site. Therefore, the external field required to switch the bilayer is relatively low $H_{90\%} = 181 \text{ mT}$.

Keeping $\sigma_K^{\text{FI}} = 0$, with increasing $\theta_{\text{max}}^{\text{FI}}$, pinning sites are created between patches. Therefore a higher external field is needed to switch the bilayer. At $\theta_{\text{max}}^{\text{FI}} = \pi/4$ the required external field is more than doubled with $H_{90\%} = 386 \text{ mT}$. In Figure 4.6 this result is marked with [a]. In the accompanying snapshot [a] pinning sites can be seen by the bowed domain wall in the FI-layer. The domain wall in the FM-layer is leading the reversal. With further advancement of the reversal, the domain wall also gets weakly pinned at parts of the interface (not seen in the snapshot).

When σ_K is also increased the required field increases significantly. With $\sigma_K = \bar{K}_u^{\text{FI}} = 889 \text{ kJ/m}^3$ and $\theta_{\text{max}}^{\text{FI}} = \pi/4$ the field $H_{90\%} = 2.739 \text{ T}$. A snapshot of the domain wall movement for this parameter set and is shown in Figure 4.6 [b]. Much more pinning sites can be seen at patch boundaries and the domain wall also pins at the interface.

With perfectly aligned easy axes ($\theta_{\text{max}}^{\text{FI}} = 0$) the required field is almost as high with $H_{90\%} = 2.626 \text{ T}$. Therefore, looking at the diagram in Figure 4.6 it can be stated, that the distribution of K_u is the dominating factor for the pinning events and consequently for the required switching field. The pinning events can be seen in the magnetization reversal curves in Figure 4.7.

The bright curves show actual magnetization evolutions of five single simulations, red for no distribution of K_u^{FI} and blue for the maximal value. The thick dark lines represent the average of their respective five curves. For all curves the cone angle is set to $\theta_{\text{max}}^{\text{FI}} = \pi/4$. The magnetization curves for $\sigma_K = \bar{K}_u^{\text{FI}}$ (blue) show much more steps, *i.e.* pinning events, than those with no distribution of the magnetocrystalline anisotropy constant.

4.4 Summary

The adapted and implemented micromagnetic model for ferrimagnetic thin films presented in Chapter 3 was extended by considering an additional exchange coupled ferromagnetic film. In order to incorporate the microstructural features of the amorphous ferrimagnet, the two layers had to be meshed separately. To restore the continuity at the interface between the two layers, a surface integral technique, as suggested by Dean *et al.* [20], was used and the interface exchange energy was computed.

The magnetization reversal curve of the ferri-/ferromagnetic bilayer was computed by averaging over many curves calculated with different exchange coupling energy. The exchange coupling strength proves to be an important property to control the switching field of the bilayer. A Weibull-distribution with the parameters $\lambda = 2.21$ and $k = 1.13$ for the exchange coupling strength was found to successfully shape the averaged curve to reproduce the measured data of Schubert *et al.* [130]. The result

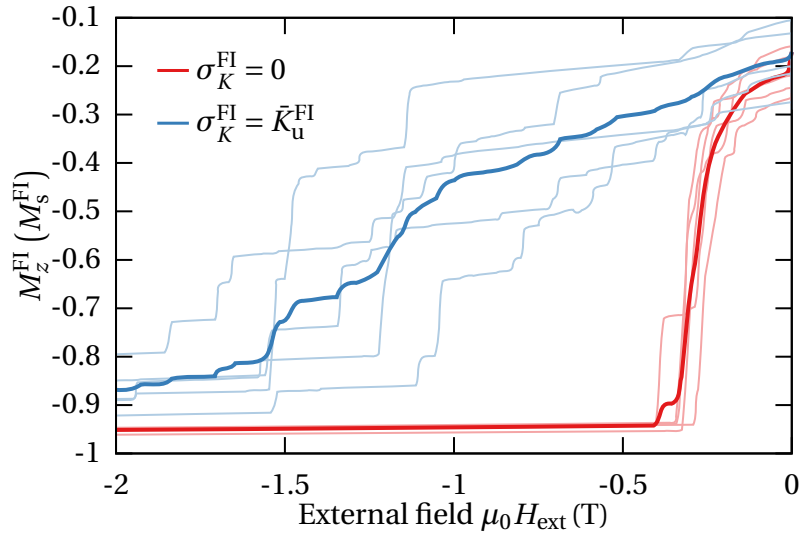


Figure 4.7: Magnetization reversal curves showing pinning and depinning events depending on the uniaxial anisotropy constant distribution across the ferrimagnetic patches. The red curves result from homogeneous K_u across patches, but still varying cone angle θ_{\max} and the blue curves from FI-layer with a standard deviation as big as the mean K_u^{FI} value. The thick solid lines represent the mean curves of their respective five thinner curves.

indicates that large regions are weakly coupled and only a minor portion exhibits stronger coupling. Minor reversal curves show that as long as the harder ferrimagnetic layer is not switched, the magnetization configurations are fully reversible. As soon as the domain wall gets pushed through the interface into the ferrimagnetic layer, the switching is irreversible. This is also in agreement with the findings in [130].

The domain wall motion is investigated in the ferri-/ferromagnetic bilayer. The models show a lateral movement of the domain wall, governed by pinning at the patch boundaries of the ferrimagnetic layer, due to its spatial distribution of anisotropic properties. While pinning sites are provided by the distribution of the easy axis across the patches, the distribution of the uniaxial anisotropy constant is the determining parameter for creating pinning sites. The pinning events can be clearly seen as steps in the magnetization reversal curves. Pinning occurs also at the interface, but the coupled ferromagnetic layer helps the reversal of the bilayer. By pushing the domain wall upwards into the ferrimagnetic layer its switching field is reduced depending on the exchange coupling strength at the interface (*cf.* Figure 4.3). This results support the findings of Schubert *et al.* [130].

Exchange coupled bilayers in bit patterned media

Contents

5.1	Model for ferri-/ferromagnetic bilayer dots.....	66
5.2	Magnetization reversal of bilayer dots	68
5.2.1	Effect of dot diameter	69
5.2.2	Effect of exchange coupling strength at the interface	71
5.2.3	Effect of ferrimagnetic layer thickness.....	75
5.3	Switching field distribution	80
5.3.1	Intrinsic switching field distribution.....	82
5.3.2	Dipolar interaction field in bit patterned media	85
5.3.3	Bit error rate of bilayer dot arrays	90
5.4	Further characterization of dots in bit patterned media	97
5.4.1	Switching field reduction by redeposition.....	97
5.4.2	Effect of dot edge roughness	99
5.5	Read back field of bilayer dots	102
5.6	Summary.....	104

Portions of this chapter are reprinted from [104] and [102] with permission of the coauthors and in accordance with the publisher's policy. Copyright 2015 and 2016, AIP Publishing LLC. Content which was not generated by the author of this thesis is explicitly denoted.

One of the possible applications of ferrimagnetic materials lies in the use as a component for magnetic recording media (see Section 2.4). The concept of bit patterned media (BPM) is one of several promising approaches to push data density in magnetic storage devices beyond the limits of conventional perpendicular magnetic recording (PMR) [144, 112, 4]. In this scheme the recording media is an array of decoupled magnetic single domain islands where each dot stores one data bit. While this recording scheme reduces bit transition jitter and improves signal to noise ratio (SNR) compared to PMR [3], the writeability and thermal stability of the magnetic islands need to be maintained (see Section 2.4.1). This can be addressed by designing the islands as exchange spring or exchange coupled composite (ECC) structures which are made of at least two layers with different magnetic anisotropy [149, 141, 137, 46]. One layer is made of a material with high magnetic anisotropy (usually FePt) to ensure thermal stability. By adding an exchange coupled soft magnetic layer the required switching field is decreased and therefore the writeability is restored. Experimental studies confirmed the feasibility of exchange coupled media in multilayer structures [14] and later also in bit patterned media [44, 125, 51]. Krone *et al.* [69] performed micromagnetic simulations of arrays consisting of exchange coupled composite stacks and also graded media, where the magnetic anisotropy constant decreased quadratically across ten layers.

In this chapter, arrays of exchange coupled bilayer dots, where a ferrimagnetic material such as FeTb or FeGd represents the soft magnetic layer, are investigated. Ferrimagnetic materials have been extensively studied [41, 84] and used as magneto-optical recording media [73, 58]. A big advantage of using ferrimagnetic layers is the possibility to tailor their magnetic properties through their composition with respect to the desired working temperature [93]. Moreover, since these layers are amorphous, the lack of crystalline defects may positively influence the switching field distribution of the exchange coupled ferromagnetic layer. Also in combination with the concept of heat assisted magnetic recording (HAMR) such materials bear potential when exploiting their compensation point. In the following sections the previously developed model is used to investigate the switching behavior of exchange coupled ferri-/ferromagnetic composite dots. First the reversal curves of such single dots with varying microstructure are calculated. The calculations are carried out with different diameters, exchange coupling strength at the interface and varying thickness of the ferrimagnetic layer. The effects of these parameters on the reversal process and the switching field distribution are discussed subsequently.

Since in bit patterned media the dots are also influenced by their neighboring dots, the dipolar interaction field is computed for two types of arrays: a square patterned array and a triangular patterned array. The combination of the single dots switching field distribution and the interaction field distribution is then expressed by calculating the theoretical bit error rate for writing. In order to quantify the effect of the coupled

ferrimagnetic layer the bit error rate is determined for arrays of dots without this soft layer and with different soft layer thickness. Dots in sample arrays fabricated at the Paul Scherrer Institute in Switzerland show a certain edge roughness. Therefore the effect of this roughness on the switching field is investigated by micromagnetic simulations for different dot diameters. The fabricated samples also show redeposited material at the vertical faces of the dots. The possible reduction of the switching field due to this redeposition is simulated and discussed.

5.1 Model for ferri-/ferromagnetic bilayer dots

In this chapter cylindrical dots composed of a ferromagnetic layer Ω^{FM} and a ferrimagnetic layer Ω^{FI} collinearly exchange-coupled at the interface Γ are investigated. A detailed explanation of the ferrimagnetic model has already been given in Section 3.2 and of the ferri-/ferromagnetic exchange coupled bilayer in Section 4.1. This micromagnetic model is again applied to investigate the reversal of bilayer dots and is briefly repeated here for convenience.

Mansuripur's [85] approach is implemented by assuming that the ferrimagnetic sublattices are strongly coupled antiparallel at all times. Therefore the magnetic moments $\mathbf{M}^{(a)}$, $\mathbf{M}^{(b)}$ of the sublattices are substituted by an effective net moment $\mathbf{M}^{\text{FI}} = \mathbf{M}^{(a)} + \mathbf{M}^{(b)}$. The Gilbert equations of both sublattices can then be summed up to obtain an effective Gilbert equation. To take into account the exchange coupling between the two layers, the equation for the effective field of each layer has to be extended. The interface exchange field $\mathbf{H}_{\text{ix}} = -1/\mu_0 \delta E_{\text{ix}}/\delta \mathbf{M}$ exerted by the respective neighboring layer is added to \mathbf{H}_{eff} . The exchange energy across the interface Γ is given by $E_{\text{ix}} = -J_{\text{ix}} \int_{\Gamma} \mathbf{m}^{\text{FM}} \mathbf{m}^{\text{FI}} d\Gamma$, where J_{ix} is the exchange coupling strength at the interface and \mathbf{m} is the unit vector of each spin direction. Due to the microstructural differences both layers have to be meshed separately. As the mesh nodes at the interface do not match, a surface integral technique is employed and E_{ix} is calculated by using a symmetric Gaussian quadrature rule for triangles [28, 20]. The microstructural features of the layers are considered in the geometrical model shown in Figure 5.1. The ferromagnetic granular, magnetically hard layer Ω^{FM} is shown on the top, the soft amorphous ferrimagnetic layer Ω^{FI} at the bottom. The layers are coupled collinearly at the interface Γ . No intergranular phase is considered.

The Ω^{FM} model is a $L1_0$ chemically ordered $\text{Fe}_{52}\text{Pt}_{48}$ layer with an average grain size of $\bar{s}_g = 13$ nm. Since the grains grow in a columnar fashion grain size is defined by cross-sectioned area in the in-plane direction as described in (3.13) for patches. The layer exhibits a saturation polarization of $J_s^{\text{FM}} = 1.257$ T and an exchange stiffness constant of $A_x^{\text{FM}} = 10$ pJ/m. Each grain g_i has its own randomized anisotropy constant and uniaxial anisotropy direction. The average assigned anisotropy constant $\bar{K}_u^{\text{FM}} =$

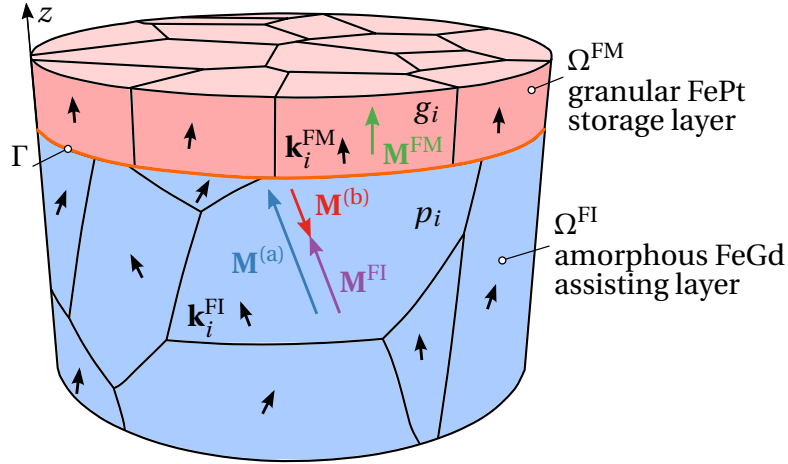


Figure 5.1: Geometric model of the bilayer dot with a ferrimagnetic phase Ω^{FI} and a ferromagnetic phase Ω^{FM} collinearly coupled at the interface Γ . The magnetically softer, amorphous assisting layer Ω^{FI} is divided in patches p_i with varying uniaxial anisotropic properties \mathbf{k}_i^{FI} and $K_{u,i}^{\text{FI}}$. The granular hard magnetic phase (storage layer), Ω^{FM} , possesses strong out-of-plane uniaxial anisotropy.

1.3 MJ/m^3 with a standard deviation of $0.05 \bar{K}_u^{\text{FM}}$. The uniaxial easy direction is limited within a cone angle of $\theta_{\text{max}} = 15^\circ$ from the out-of-plane (z -) axis.

The Ω^{FI} phase is an amorphous $\text{Fe}_{74}\text{Gd}_{26}$ layer. The ferrimagnet is characterized by a saturation polarization of $J_s^{\text{FI}} = 0.268 \text{ T}$ and an exchange stiffness constant of $A_x^{\text{FI}} = 2 \text{ pJ/m}$. To incorporate material inhomogeneities in the amorphous model the layer is divided into patches p_i with an average diameter of $\bar{s}_p = 13 \text{ nm}$ as suggested by Mansuripur and Giles [88]. Generally the patch size is defined by volume according to (3.14). However, in Section 5.2.3 the thickness of the ferrimagnetic layer t_{FI} is reduced below the patch-size \bar{s}_p . This would result in flattened and thus fewer patches, provided the volume is kept constant.

To avoid this, for ferrimagnetic layers with a thickness below the average patch size, the calculation of the layer volume V^{FI} is modified as described in (5.2). To generate the tessellation the number of patches n_p has to be provided. The number of patches is determined by the desired patch size and, of course, by the volume of the layer V^{FI} .

$$n_p = \frac{6 V^{\text{FI}}}{\pi \bar{s}_p^3} \quad \text{with} \quad (5.1)$$

$$V^{\text{FI}} := \begin{cases} \frac{d^2}{4} \pi \bar{s}_p & \text{if } t_{\text{FI}} < \bar{s}_p, \\ \frac{d^2}{4} \pi t_{\text{FI}} & \text{if } t_{\text{FI}} \geq \bar{s}_p. \end{cases} \quad (5.2)$$

Table 5.1: Properties of the FM/FI-bilayer islands for reversal investigation.

Layer	A_x (pJ/m)	\bar{K}_u (kJ/m ³)	σ_K (%)	θ_{\max} (°)	J_s (mT)	\bar{s} (nm)
FM (Fe ₅₂ Pt ₄₈)	10	1300	5	15	1257	13
FI (Fe ₇₄ Gd ₂₆)	2	10	20	90	268	13

This means, just for the calculation of the number of patches, the thickness of the cylindrical layer is artificially limited to the patch size. Of course, with a constant dot diameter d , also the volume of the layer has now a lower limit and subsequently the number of patches too.

Each patch exhibits its own randomly assigned anisotropy constant and uniaxial anisotropy direction. The average anisotropy constant $\bar{K}_u^{\text{FI}} = 10 \text{ kJ/m}^3$ with a standard deviation of $0.2\bar{K}_u^{\text{FI}}$. The uniaxial easy direction varies within a cone angle of $\theta_{\max} = 90^\circ$ from patch to patch. The properties of the bilayer dots are again summarized in Table 5.1 for convenience.

5.2 Magnetization reversal of bilayer dots

In order to increase the capacity of storage devices, *e.g.* the areal density of bit patterned media, small dot diameters are favorable. The field of the write head has to exceed the switching field of the dots to be able to write data on the medium. In current recording devices this write field is limited to around 1 T. Therefore, it is necessary to look at the magnetization reversal and the switching field of the dots to gain a better understanding for their application in magnetic recording.

Using the model of ferri-/ferromagnetic bilayer dots the magnetization reversal is studied by finite element micromagnetic simulations. For this purpose finite element meshes of bilayer dots with different diameters from 5 to 120 nm are generated with the software package Neper [114]. The software is able to tessellate the layers into grains for FePt and patches for FeGd. For each diameter 20 meshes with varying microstructure for both layers are generated. The characteristic length (see Section 2.2.4) for the materials $l_c = 2.8 \text{ nm}$ for the properties given in Table 5.1. With a mesh size for both layers which is always kept smaller than 2.5 nm the domain walls should be represented correctly. The comparison of simulations for several representations of the bilayer structure gives a better idea how the microstructural differences of real bilayer dots effect the reversal. Using the programming language Python [113], a script was developed to automate the process of generating these meshes and starting the simulations.

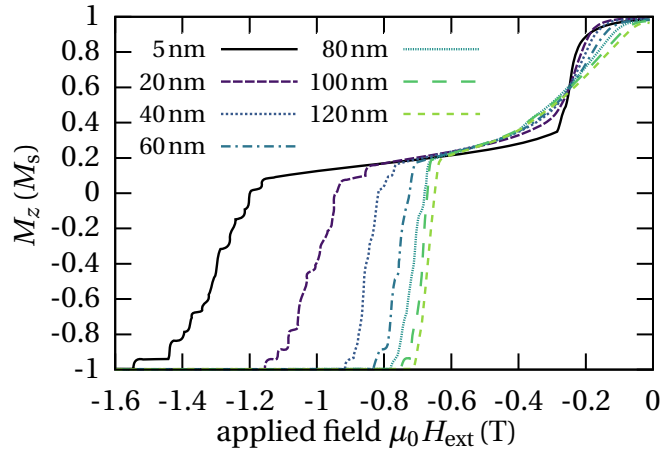


Figure 5.2: Averaged reversal curves of 20 dots for different dot diameters. The layers of the dot are strongly coupled with $J_{ix} = 5 \text{ mJ/m}^2$.

The reversal curves are computed for all diameters and microstructures. Also the randomized anisotropic properties of both layers were generated anew for each simulation within the limits described previously. Since we are only interested in the static hysteresis behavior, the damping constant is set to $\alpha_{\text{eff}} = 1$. The simulations start with magnetically saturated dots. By applying an increasing external field H_{ext} in the opposite direction to the magnetization of the dot, the reversal curve is computed. In the following the effects of three critical parameters are investigated: 1) the diameter of the ferri-/ferromagnetic bilayer dots, 2) the exchange coupling strength at the interface between the two layers, and 3) the thickness of the ferrimagnetic layer. In addition the read-back field for different thickness of the ferrimagnetic layer is computed.

5.2.1 Effect of dot diameter

The simulations are done for bilayer dots with a hard magnetic FePt layer of $t_{\text{FM}} = 5 \text{ nm}$ thickness and a $t_{\text{FI}} = 20 \text{ nm}$ thick soft magnetic FeGd layer. The exchange coupling strength at the interface is set to $J_{ix} = 5 \text{ mJ/m}^2$. For each dot diameter the reversal curve of 20 bilayer dots with varying random microstructure are computed. An average curve over the 20 reversal curves for each dot diameter is then calculated.

Presenting the demagnetization curve averaged over several representations of a dot resembles the experiment, where the hysteresis loop of a thin film containing many dots is measured. In the experiment the dots would also have almost equal diameter, but varying microstructure and anisotropic properties. In this simulation the interaction between the dots is neglected. The resulting averaged reversal curves for different dot diameters are depicted in Figure 5.2.

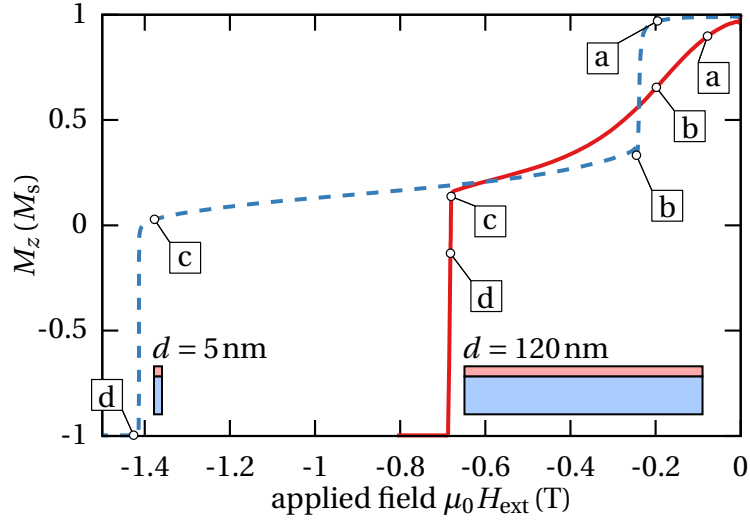


Figure 5.3: Reversal curves of two dots with different diameters: $d = 5$ nm in blue and $d = 120$ nm in red. The labels **a** to **d** of both curves correspond to the respective states shown on page 72 in Figure 5.4 and Figure 5.5.

The reversal curve computation was started with a positively saturated magnetization state at $\mu_0 H_{\text{ext}} = 2$ T, but since the remanent magnetization in z -direction M_r is almost equal to M_s , Figure 5.2 shows only the negative field axis. For all diameters the soft magnetic Ω^{FI} phase switches at about -0.27 T. With increasing diameter the reversal curve of the soft magnetic phase gets flattened. This can be accredited to the shape anisotropy, since the layer thickness is fixed for all models. The reversal of the hard magnetic Ω^{FM} phase strongly depends on the dot diameter. The switching field lies between 0.65 T and 1.3 T. With smaller diameters the Ω^{FM} phase consists only of one or a few grains, which leads to a flattened reversal curve when averaged over the 20 simulations, *i.e.* a broader switching field distribution. The switching field $H_{\text{sw}}^{\text{FM}}$ drastically increases with decreasing diameter. This is because with increasing diameter the reversal mode changes from the single domain to the multi-domain regime (see Section 2.3.3).

To support this claim two simulations, one with a dot diameter $d = 5$ nm and one with $d = 120$ nm, are chosen for further investigation. The reversal curves of these two bilayer dots are shown in Figure 5.3. Since only one example for each diameter is picked the curves are not averaged and the switching of the FePt phase shows a single step for both diameters. For both example dots the spatial magnetization configuration of the whole model during the reversal process is calculated. This enables the investigation of the reversal mechanisms involved.

In order to visualize the magnetic configuration a cut through the center of the

bilayer dots is made. These x - z -slices for different reversal states are shown on page 72 in Figure 5.4 for $d = 5$ nm thickness and for $d = 120$ nm in Figure 5.5. The four different reversal states of each dot are labeled [a] to [d] and are also marked in the respective reversal curves in Figure 5.3. Due to the large diameter difference the figures are not of the same size scale. But in both figures the 5 nm thick FePt layer is on top of the 20 nm thick FeGd layer. The colors show the magnetization in z -direction as a fraction of the saturation magnetization M_z/M_s . In red areas the magnetization is pointing down and is not yet reversed, the domain wall is black, and the blue areas are already reversed and pointing up.

By applying the external field in up direction in the small dot, the magnetic moments of the lower region coherently switch and form a domain wall due to the exchange coupling at the interface (Figure 5.4 [b]). With increasing field the domain wall gets pushed towards the interface [c], when eventually the Ω^{FM} phase nucleates as a single domain [d].

In the 120 nm dot the Ω^{FI} phase starts to rotate more inhomogeneously (Figure 5.5 [a]) and turns in-plane at the surface [b]. At this state the domain wall is widened because of its 90° configuration. With increasing H_{ext} the domain wall gets narrower and is pushed through the interface into the Ω^{FM} phase [c]. Compared to the magnetically harder phase in the smaller dot, the reversal of the harder phase in the bigger dot is much more inhomogeneous and a lateral domain wall movement can be observed leading to full reversal [d].

The difference in reversal of the Ω^{FI} phase of the larger dot compared to the small dot is exactly the reason for the change of shape of the curve in Figure 5.2 as discussed before. In contrast to the 5 nm dot, the 120 nm dot shows an inhomogeneous reversal of the magnetic moments starting with an in-plane configuration at the surface of the ferrimagnet. This leads to a flattened curve, whereas the homogeneous reversal of the soft layer in the small dot shows a steeper curve drop. In the smaller dot the magnetization of the soft layer is better stabilized by the shape anisotropy.

Also the reason for the difference in the reversal curves of the hard magnetic Ω^{FM} phase in Figure 5.2 can be seen. The dimensions of the hard layer of the small dot do not allow the formation of a domain wall and therefore it switches coherently. Due to the aspect ratio of the 120 nm diameter dot weaker grains can nucleate first and a domain wall is formed which moves then laterally. The inhomogeneous reversal leads to a lower switching field compared to the small dot.

5.2.2 Effect of exchange coupling strength at the interface

Another interesting parameter which also bears the potential of tuning the switching properties of the medium is the exchange coupling strength J_{ix} between the layers of the bilayer dots. Therefore the previous simulations of the reversal curves for different

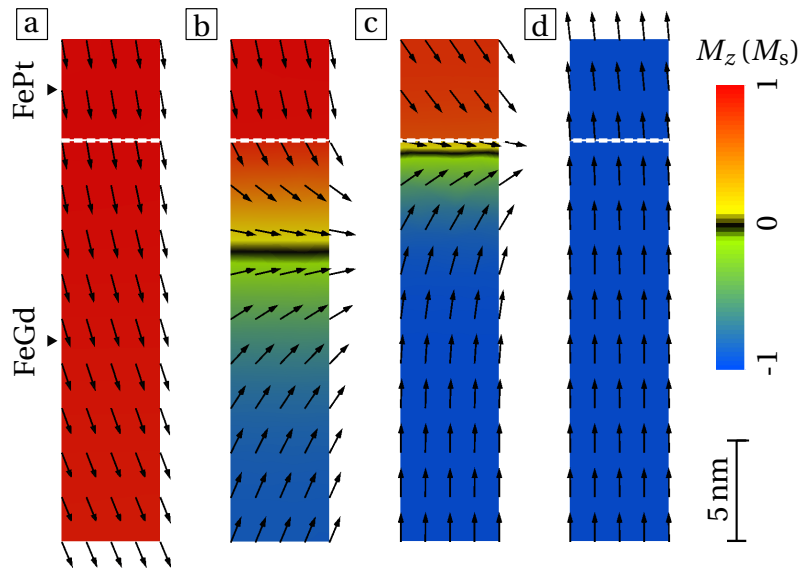


Figure 5.4: Reversal process of a dot with $d = 5$ nm from [a] to [d]. The labels correspond to those of the blue curve in Figure 5.3. The interface Γ is the white dashed line while the Ω^{FM} is the upper and the Ω^{FI} is the lower layer.

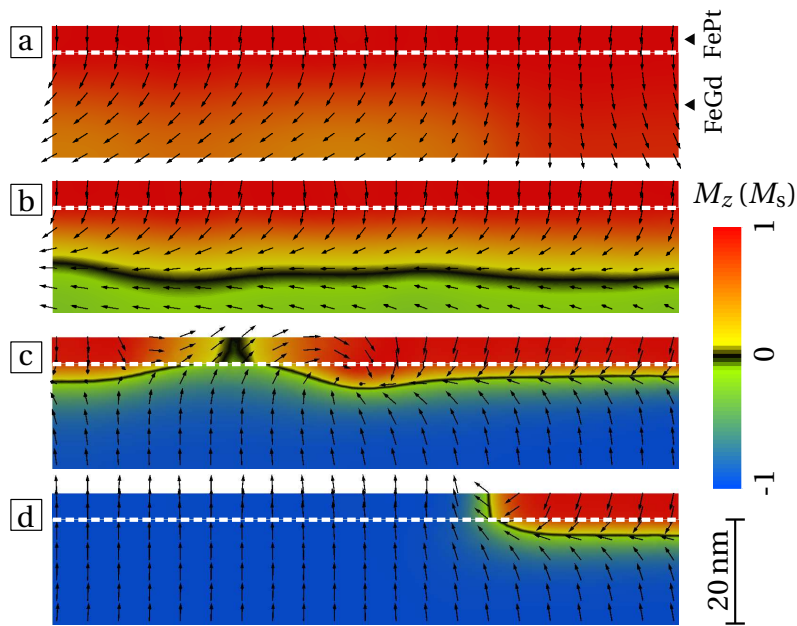


Figure 5.5: Reversal process of a dot with $d = 120$ nm from [a] to [d]. The labels correspond to those of the red curve in Figure 5.3. The interface Γ is the white dashed line while the Ω^{FM} is the upper and the Ω^{FI} is the lower layer.

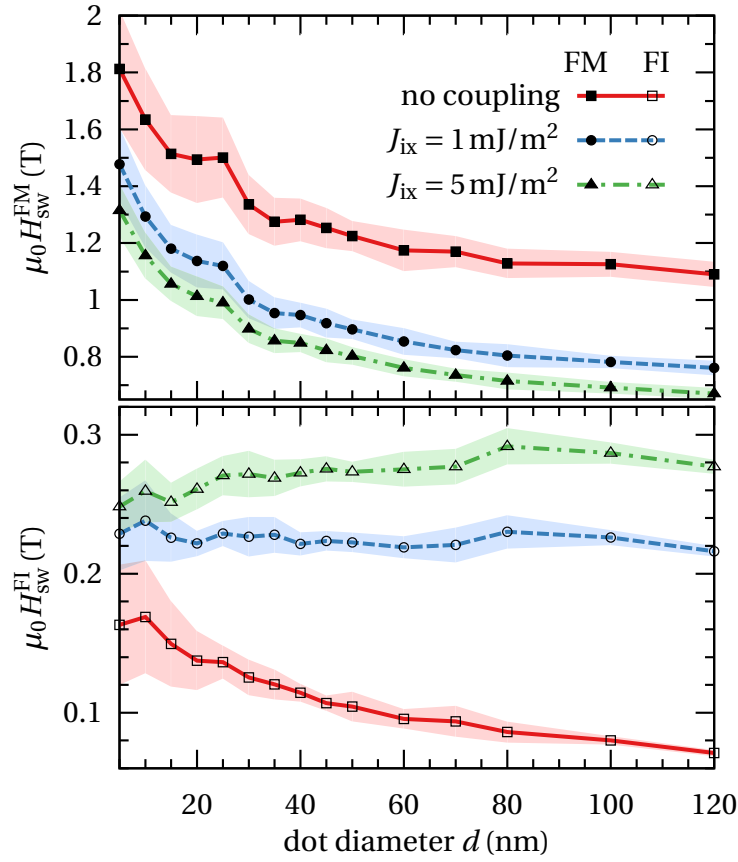


Figure 5.6: Averaged switching field of the Ω^{FM} (top) and the Ω^{FI} phase (bottom) for different interface coupling strengths depending on the dot diameter. The standard deviation σ_{int} of 20 simulations for each data point is depicted as a shaded area: $\bar{H}_{\text{sw}} \pm \sigma_{\text{int}}$.

dot diameters are performed anew with different values of coupling strength between the layers from $J_{ix} = 0$ to 5 mJ/m^2 .

In Figure 5.6 the switching fields for three coupling strengths are plotted against the dot diameter: no coupling (red solid), 1 mJ/m^2 weak coupling (blue dashed) and 5 mJ/m^2 strong coupling (green dot-dashed). In case of no coupling the two layers only experience the stray field of each other.

Figure 5.6 shows the switching field of the hard-magnetic FM phase in the top diagram and that of the soft-magnetic ferrimagnet at the bottom. These switching fields, H_{sw}^{FM} and H_{sw}^{FI} , are defined as $M_z^{FI}(H_{\text{sw}}^{FI}) = 0$ and $M_z^{FM}(H_{\text{sw}}^{FM}) = 0$. Again the field values for each dot diameter are averaged over the $n = 20$ randomized simulation runs. Since the simulations to calculate the switching fields deal only with variation of intrinsic properties of a bilayer dot, the resulting distribution is called intrinsic

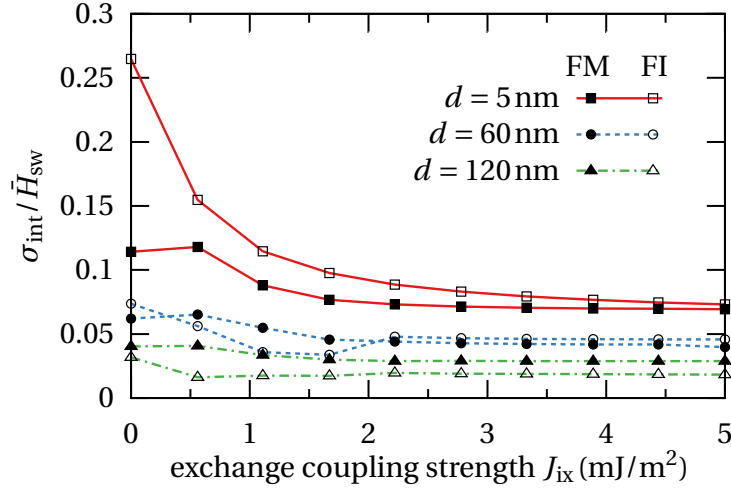


Figure 5.7: Relative standard deviation of the switching field of both layers for different dot diameters as a function of interface exchange coupling strength.

switching field distribution [146]. The intrinsic standard deviation given by (5.3) for the 20 simulations is shown as a shade in the respective color ($\bar{H}_{\text{sw}} \pm \sigma_{\text{int}}$).

$$\sigma_{\text{int}} = \sqrt{\frac{1}{n-1} \sum_{i=1}^n (H_{\text{sw},i} - \bar{H}_{\text{sw}})^2}. \quad (5.3)$$

In Section 5.3 the switching field distribution of bilayer dots is investigated more elaborately. The translation from homogeneous to inhomogeneous reversal of the hard magnetic phase as described before can be clearly recognized in Figure 5.6 where the $H_{\text{sw}}^{\text{FM}}$ curves drop between 25 nm and 30 nm dot diameter. Without a coupled ferrimagnet, $H_{\text{sw}}^{\text{FM}}$ is reduced by 39%, when moving from a 5 nm to a 120 nm dot diameter. For a strongly coupled bilayer this reduction is improved to 50%. If we look at a specific dot diameter, introducing the coupled ferrimagnet reduces $H_{\text{sw}}^{\text{FM}}$ by 30% to 40%. The higher the diameter, the higher the reduction of the switching field of the hard phase. While the switching field of a single ferrimagnetic layer would decrease with growing diameter, an increasing interface coupling can stabilize or even cause an increase of $H_{\text{sw}}^{\text{FI}}$ by about 12% within the investigated diameter range.

Looking at the shaded area for the switching field distribution in Figure 5.6, it can be seen that the switching field distribution decreases with increasing diameter and interface exchange coupling for the ferromagnet. The ferrimagnetic phase shows a significant reduction of the switching field distribution when increasing the diameter from 5 to 20 nm. The switching field distribution stems solely from the random granular variation and the variation of anisotropic properties, K_{u} and \mathbf{k} , in both layers of the dots. This behavior can also be seen in Figure 5.7 where the relative

Table 5.2: Properties of the FM/FI-bilayer islands fitted to experiments.

Layer	A_x (pJ/m)	\bar{K}_u (kJ/m ³)	σ_K (%)	θ_{\max} (°)	J_s (mT)	\bar{s} (nm)
FM (Fe ₅₂ Pt ₄₈)	10	975	5	15	1257	14
FI (Fe ₇₄ Gd ₂₆)	2	8	20	90	268	10

standard deviation of the switching field $\sigma_{\text{int}}/\bar{H}_{\text{sw}}$ is plotted against the exchange coupling strength. The underlying data stems from the same simulation results used in Figure 5.6. The filled markers refer to the ferromagnetic phase and the open markers to the ferrimagnetic phase for three different dot diameters: 5 nm, 60 nm and 120 nm.

Coupling the ferrimagnetic layer to the ferromagnet decreases the relative standard deviation $\sigma_{\text{int}}^{\text{FM}}/\bar{H}_{\text{sw}}^{\text{FM}}$ from 11% to below 7% for 5 nm diameter. For larger diameters it decreases to 4% for 60 nm or even below 2% for 120 nm. The relative standard deviation for the ferrimagnet is also reduced with increasing interface exchange energy, especially for the 5 nm diameter dot, where it is reduced from 26% to 7%. The major change of the switching field distribution occurs below $J_{\text{ix}} = 2 \text{ mJ/m}^2$ and only slightly improves above.

5.2.3 Effect of ferrimagnetic layer thickness

So far the thickness of the layers have been kept constant to investigate coupling strength and dot diameter. In this section the thickness of the ferrimagnetic layer t_{FI} is varied to look at its influence on the reversal process. The thickness of the hard-magnetic FM layer is kept at $t_{\text{FM}} = 5 \text{ nm}$. In order to reflect measurement results provided by collaborators P. Matthes, D. Nissen and M. Albrecht at the Institute of Physics, University of Augsburg, the properties of the two layers for the following simulations are slightly changed. An overview of the used parameters is given in Table 5.2. The interface coupling strength is set constant to $J_{\text{ix}} = 5 \text{ mJ/m}^2$.

Again reversal curves for the bilayer dots are computed and the switching fields determined as before. The thickness of the FI-layer is varied between none at all and $t_{\text{FI}} = 50 \text{ nm}$. As described before in Section 5.1, in order to preserve the shape of the patches, the number of patches for tessellation have to be calculated differently when the thickness of the ferrimagnetic layer drops below the desired patch size. As defined in (5.2), for a certain dot diameter, the number of patches can not be decreased further when reducing t_{FI} below the patch size.

For each value of t_{FI} , the switching fields of 100 islands with randomized microstructure and anisotropic properties are computed. The curves in Figure 5.8 show the mean value $\bar{H}_{\text{sw}}^{\text{FM}}$ of these 100 switching fields depending on t_{FI} for three different

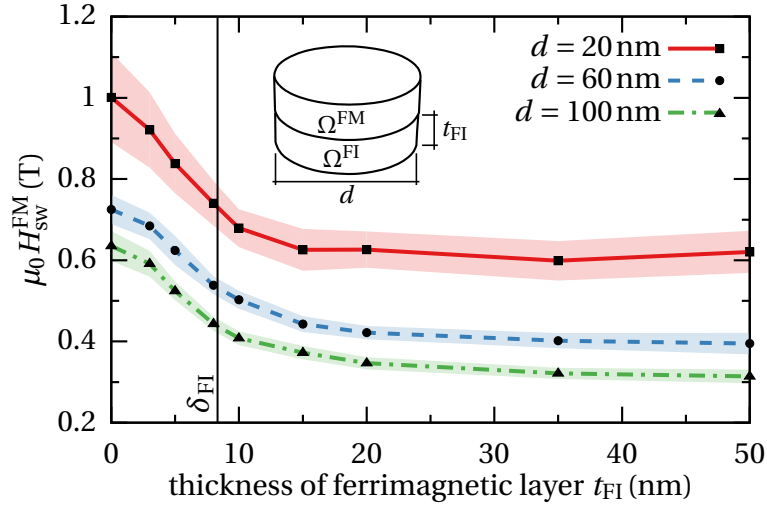


Figure 5.8: Mean switching field of bilayer islands depending on the thickness of the ferrimagnetic soft layer for different island diameters ($d = 20$ nm, 60 nm and 100 nm). The standard deviation of the intrinsic switching field distribution is depicted as a shade in the respective color. The thin vertical line marks the theoretical width δ_{FI} of the domain wall in the FI-layer pinned at the interface.

island diameters d : 20 nm, 60 nm and 100 nm. The standard deviation $\pm\sigma_{\text{int}}$ for the 100 simulation runs is shown as a shading for each curve in the respective color and illustrates the intrinsic switching field distribution. Here the switching field is that of the magnetically harder FM layer, since this is the one which stores the bit in a storage medium application.

The curves in Figure 5.8 show again a decreasing switching field with increasing dot diameter. As found in Section 5.2.1, this is due to a change of reversal mechanism from a quasi uniform rotation for small diameters to the nucleation and expansion of a reversed domain in larger diameters. The mean switching field \bar{H}_{sw} decreases with increasing t_{FI} as expected, but only up to a certain value ($t_{\text{FI}} = 15$ nm for $d = 20$ nm) for our set of parameters. This threshold is determined by whether the thickness of the soft ferrimagnetic layer supports the formation of a domain wall [49]. For very thin soft ferrimagnetic layers the bilayers reverse their magnetization at the nucleation field [134] of

$$H_{\text{n}} = 2 \frac{t_{\text{FM}}K_{\text{u}}^{\text{FM}} + t_{\text{FI}}K_{\text{u}}^{\text{FI}}}{t_{\text{FM}}J_{\text{s}}^{\text{FM}} + t_{\text{FI}}J_{\text{s}}^{\text{FI}}}. \quad (5.4)$$

When increasing the thickness t_{FI} , a domain wall is formed in the FI-layer and gets pinned at the interface between the two layers. Therefore the switching field is now

determined by the pinning field [70, 141]

$$H_p = \frac{2K_u^{\text{FM}}}{J_s^{\text{FM}}} \frac{1 - \varepsilon_K \varepsilon_A}{(1 + \sqrt{\varepsilon_J \varepsilon_A})^2}, \quad (5.5)$$

where

$$\varepsilon_K = \frac{K_u^{\text{FI}}}{K_u^{\text{FM}}}, \quad \varepsilon_A = \frac{A_x^{\text{FI}}}{A_x^{\text{FM}}} \quad \text{and} \quad \varepsilon_J = \frac{J_s^{\text{FI}}}{J_s^{\text{FM}}}. \quad (5.6)$$

In a thin single layer film the required thickness to form a domain wall would be approximated by the width of a Néel wall (as given in (2.61)). But in an exchange coupled film the domain wall width is determined by the pinning field which pushes the wall against the interface. Thus, the required thickness of the ferrimagnetic layer to support the formation of a domain wall can be approximated by

$$\delta_{\text{FI}} = \pi \sqrt{\frac{A_x^{\text{FI}}}{J_s^{\text{FI}} H_p}}. \quad (5.7)$$

This theoretical domain wall thickness is also shown in Figure 5.8 as a vertical thin line and proves to be a good approximation for the transition between incoherent nucleation and domain wall depinning. The highest reductions in switching field can be seen before the thickness of the ferrimagnetic layer reaches the critical domain wall width δ_{FI} .

For islands with a diameter of $d = 20$ nm, a 40% decrease of the mean switching field can be achieved by adding the ferrimagnetic layer. At the same time this also improves the intrinsic switching field distribution up to a thickness of around $t_{\text{FI}} = 20$ nm but the intrinsic switching field distribution shows a slight increase again above this point. For the case of a dot with a diameter of $d = 20$ nm, the hard magnetic layer consists only of two grains whereas the FM-layer of an island with $d = 100$ nm is divided in 69 grains. This, of course, leads to a narrower switching field distribution for the larger dot, because the overall experienced anisotropy is more uniform from dot to dot. However, the reduction of the standard deviation due to the added ferrimagnetic layer is much more pronounced for small diameters.

To investigate the dependency of the magnetization reversal on the thickness of the ferrimagnetic layer more closely, models with a FI-thickness below and above δ_{FI} are selected: $t_{\text{FI}} = 5$ nm and 20 nm. In Figure 5.9 on page 78 the demagnetization curves of bilayer islands with diameters $d = 20$ nm and 100 nm are compared with the two values for t_{FI} . The thickness of the ferromagnetic layer for all four designs $t_{\text{FM}} = 5$ nm. Additionally Figure 5.10 on page 78 shows two magnetic configuration states during magnetization reversal for each of the four island designs. The labels on the curves in Figure 5.9 correspond to those in Figure 5.10.

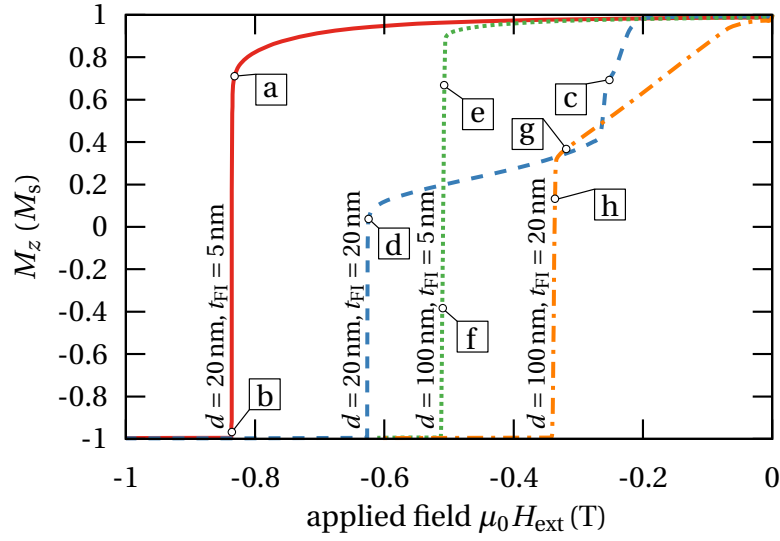


Figure 5.9: Demagnetization curves of bilayer islands with diameter $d = 20$ nm and 100 nm and thickness of soft ferrimagnetic layer of $t_{\text{FI}} = 5$ nm and 20 nm. The thickness of the hard ferromagnetic layer is kept constant at $t_{\text{FM}} = 5$ nm. The labels **a** to **h** correspond to the magnetic states in Figure 5.10, two for each island design.

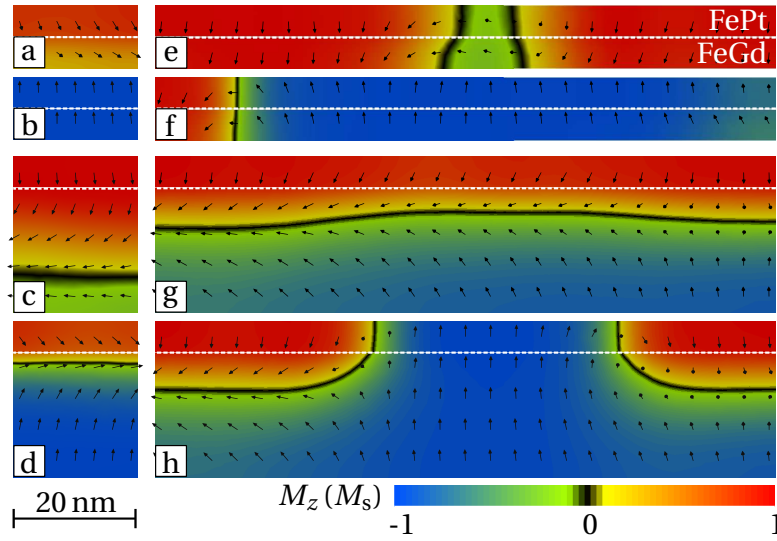


Figure 5.10: Magnetic configuration during magnetization reversal of four different bilayer designs. The interface between the layers is the white dashed line. Left: $d = 20$ nm with $t_{\text{FI}} = 5$ nm (**a**, **b**) and $t_{\text{FI}} = 20$ nm (**c**, **d**). Right: $d = 100$ nm with $t_{\text{FI}} = 5$ nm (labels **e**, **f**) and $t_{\text{FI}} = 20$ nm (labels **g**, **h**). The labels **a** to **h** correspond to the markers in Figure 5.9.

Again, as seen before in Section 5.2.1, in Figure 5.9 dots with larger diameter have a reduced switching field compared to dots with a small diameter, due to the change in reversal mechanism. The small dots show the quasi uniform rotation of the harder ferromagnetic layer, while the larger dots show a nucleation and expansion of a reversed domain in Figure 5.10. For a small dot diameter with larger t_{FI} , a domain wall is formed in the soft ferrimagnetic layer. However, the reversal of the hard layer is still by quasi uniform rotation (Figure 5.10 [c] and [d]). Nonuniform reversal modes have a lower nucleation field [13]. When the diameter is increased the numerical results show nonuniform reversal of the hard layer (Figure 5.10 [g] and [h]).

The demagnetization curves with $t_{\text{FI}} = 5 \text{ nm}$ show a single step reversal regardless of the diameter. The thin ferrimagnetic layer does not support the formation of a domain wall and the switching is determined by the reversal of the harder ferromagnetic layer. The reversal curves for $t_{\text{FI}} = 20 \text{ nm}$ show a two-step reversal behavior. Here, a domain wall can be formed in the soft layer, which creates the first step in the curves. When considering both diameter and thickness of the ferrimagnetic layer, the reversal process can be described as follows:

- small diameter / thin FI-layer (Figure 5.10 [a] and [b]): There is no domain wall formed, the FM-layer reverses coherently in a single step. The FI-layer reduces the switching field, but tightly follows the FM-layer.
- small diameter / thick FI-layer (Figure 5.10 [c] and [d]): A domain wall is formed in the FI layer and pushed against the interface with the FM-layer. The latter switches then coherently in a single step.
- large diameter / thin FI-layer (Figure 5.10 [e] and [f]): A bubble domain is formed in the FI-layer which then expands into the FM-layer. Both layers are then laterally reversed.
- large diameter / thick FI-layer (Figure 5.10 [g] and [h]): A domain wall is formed in the FI-layer and pushed against the interface until the FM-layer switches laterally.

As described previously in Section 5.2.2 the switching behavior of the bilayer dots can also be tuned by the exchange coupling strength between the ferrimagnetic and the ferromagnetic layer. In Figure 5.11 the effect of the exchange coupling strength on the mean switching field is revisited for two different thicknesses of the ferrimagnetic layer. The same bilayer dots as in Figure 5.9 and Figure 5.10 are used: FePt (5 nm) / FeGd (5 nm) and FePt (5 nm) / FeGd (20 nm), both with a dot diameter of $d = 20 \text{ nm}$ and $d = 100 \text{ nm}$. In order to reuse some results from Section 5.2.2 the additional simulations have to be done with the same parameter set given in Table 5.1. This means that the switching fields will not fit those of Figure 5.9, but still will be

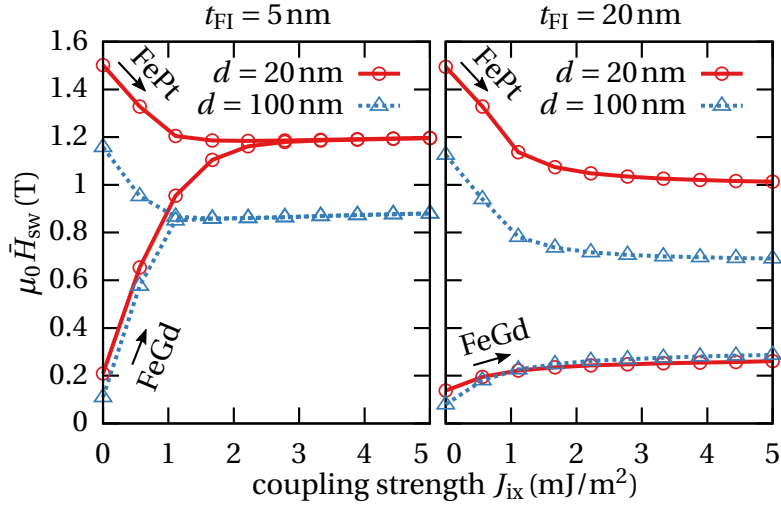


Figure 5.11: Switching fields of FePt and FeGd layer of dots with varying exchange coupling strength J_{ix} between the layers. The mean switching field is shown for diameters 20 nm (red solid line), and 100 nm (blue dotted line) and different thickness of the soft FeGd layer: 5 nm (left) and 20 nm (right).

qualitatively representative. On the left hand side of Figure 5.11 the mean switching field of dots with $t_{FI} = 5$ nm are shown, on the right hand side are the field curves for the thicker dots with $t_{FI} = 20$ nm. The switching fields are shown for both layers, FePt and FeGd, marked by the arrows and the respective description. Generally, with increasing exchange coupling strength the switching field of the harder FePt layer gets reduced and that of the softer FeGd layer increased. In case of the thinner soft layer ($t_{FI} = 5$ nm Figure 5.11 left hand side) the two switching field curves of both layers eventually merge. This means, that for weakly coupled layers the dot reverses in two steps, whereas with increased coupling strength a single step reversal is observed. For thicker soft layers ($t_{FI} = 20$ nm Figure 5.11 right hand side) the switching fields don't merge, because a domain wall is formed in the FeGd layer, and therefore a simultaneous switching, even for high values of J_{ix} is prevented. It can be stated, that regardless of the soft layer thickness, big reductions of the dot's switching field in the order of 100 mT can already be achieved at a low coupling strength. Further increase of the coupling strength yields no or only little improvement.

5.3 Switching field distribution

One of the challenges on the way towards BPM is to reduce the switching field distribution (SFD) of the dot array to ensure a low bit error rate (BER) [121]. The switching

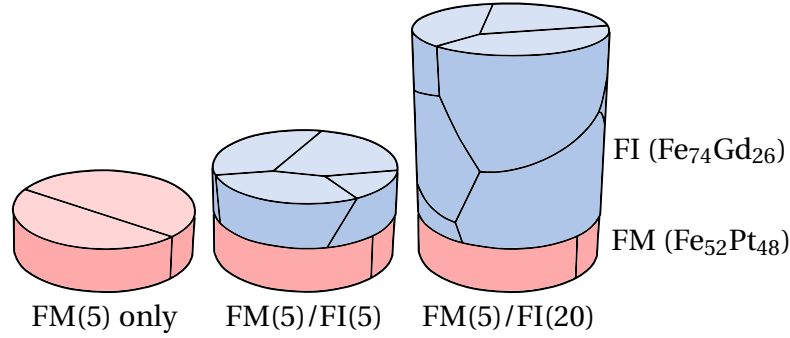


Figure 5.12: Three dot designs for the investigation of switching field distribution. For the calculations, 100 variations of each design with respect to the granular structure, patch structure and magnetocrystalline anisotropy properties are created.

field distribution origins of dots can be categorized into intrinsic contributions and stray-field contributions. While the latter deals with the dipolar field interactions between neighboring dots [53, 110, 119], the intrinsic part stems from the variation of magnetic properties, shape and size of the dots [146, 111, 78]. Obviously, the development of suitable fabrication processes for BPM plays an important role in improving the intrinsic switching field distribution.

In this section, however, the influence of an exchange-coupled ferrimagnetic layer on the switching field distribution is investigated. Due to the changed magnetization reversal process of exchange spring media and also the amorphous structure of ferrimagnetic materials, this crucial property might be improved significantly [59, 68]. Therefore, the distributions of the intrinsic and dipolar interaction field contribution are computed separately. To quantify the effect of both contributions, the bit error rate for writing is computed, taking into account the switching field distribution only and neglecting other contributions like the head field gradient.

In the following, the investigations are reduced to three dot designs, all with a diameter of $d = 20$ nm as pictured in Figure 5.12:

- *FM(5) only*: single phase FePt dots with a thickness of $t_{\text{FM}} = 5$ nm.
- *FM(5)/FI(5)*: bilayer dots with equally thick hard and soft phase $t_{\text{FM}} = t_{\text{FI}} = 5$ nm.
- *FM(5)/FI(20)*: bilayer dots with a FePt layer of $t_{\text{FM}} = 5$ nm thickness and a soft FeGd phase with $t_{\text{FI}} = 20$ nm.

With these three configurations, single phase and exchange coupled composite dots, and also bilayer dots with increased soft-layer thickness can be compared. First, in Section 5.3.1, the intrinsic switching field distribution of these dot designs are presented. Then, the dipolar interaction field distribution is calculated in Section 5.3.2.

The calculations are done for two array types, a square patterned array and a triangular patterned array. The bit error rates of the different bit patterned media are compared in Section 5.3.3.

5.3.1 Intrinsic switching field distribution

In order to get the intrinsic switching field distribution, one hundred reversal curves of each of the three dot designs, *FM(5) only*, *FM(5)/FI(5)* and *FM(5)/FI(20)*, are computed. Each dot differs only in the randomly generated microstructure and amorphous structure, and the anisotropic properties. Therefore, other contributions like variation in dot diameter or damage due to patterning are not considered. In order to reuse former simulation data the properties listed in Table 5.2 are applied. The coupling strength is set to $J_{\text{ix}} = 5 \text{ mJ/m}^2$. In Figure 5.13 the calculated switching fields of the magnetically harder FM-layer are compiled into histograms. The intrinsic switching field distribution of the dots can be described with a Gaussian fit, with the mean switching field $\bar{H}_{\text{sw}}^{\text{FM}}$ and the standard deviation σ_{int} :

$$f(h) = \frac{1}{\sigma_{\text{int}}\sqrt{2\pi}} \exp\left(-\left(\frac{h - \bar{H}_{\text{sw}}^{\text{FM}}}{\sigma_{\text{int}}\sqrt{2}}\right)^2\right). \quad (5.8)$$

The intrinsic standard deviation σ_{int} as defined in (5.3) is computed for the $n = 100$ switching field values $H_{\text{sw}}^{\text{FM}}$. Again the switching field is defined as the external field which is needed to reduce the z-component of the magnetization to zero: $M_z^{\text{FM}}(H_{\text{sw}}^{\text{FM}}) = 0$. As seen before in Section 5.2.3 the mean switching field is reduced by adding an exchange coupled ferrimagnetic soft layer. More over, the fitted curves clearly show an improvement of the switching field distribution when the ferrimagnetic layer is added. The intrinsic standard deviation is reduced by 59% for a FI-layer with $t_{\text{FI}} = 20 \text{ nm}$ from $\sigma_{\text{int}} = 110 \text{ mT}$ to $\sigma_{\text{int}} = 45 \text{ mT}$. The coupling with the $t_{\text{FI}} = 5 \text{ nm}$ layer still gives a 34% reduction of σ_{int} compared to the *FM(5) only* dot. It can be stated that adding a ferrimagnetic soft layer reduces the switching field and the intrinsic switching field distribution. Both effects imply an improvement of the bit patterned media.

One might argue that a thicker FI-layer improves the switching field distribution at the expense of thermal stability. The energy barrier of the various dots was calculated using the nudged elastic band method [22]. The results show that the energy barrier for all systems is dominated by the barrier of the hard FePt (FM) layer. The calculated energy barriers at $T = 300 \text{ K}$ are $211 k_{\text{B}}T$, $207 k_{\text{B}}T$ and $234 k_{\text{B}}T$ for *FM(5) only*, *FM(5)/FI(5)* and *FM(5)/FI(20)* respectively, where k_{B} is the Boltzmann constant. This is in qualitative agreement with the results shown by Suess *et al.* [139]. Hard-soft bilayer dots show a higher attempt frequency than single phase dots [19, 151]. With energy barriers greater than $200 k_{\text{B}}T$ even high attempt frequencies in the THz-regime give reasonable bit lifetimes.

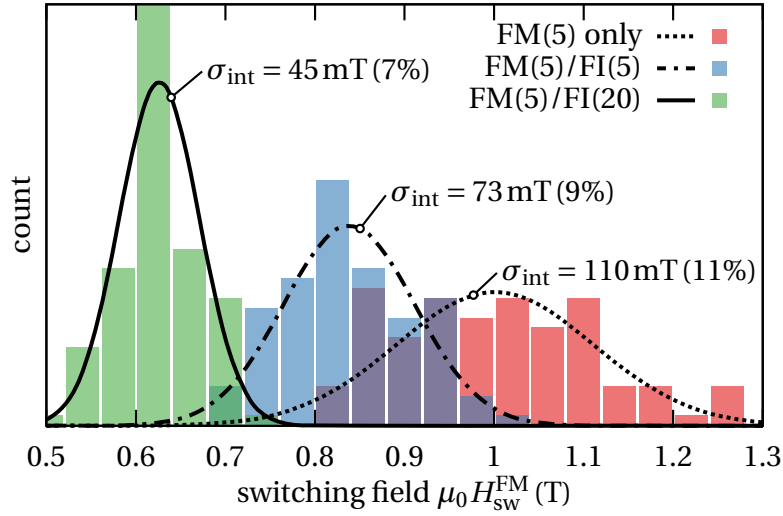


Figure 5.13: Intrinsic switching field distribution of the three dot designs shown in Figure 5.12. Gaussian fits are shown for all three designs. The standard deviation σ_{int} is given in absolute values and percentage of the respective mean switching field $\mu_0 \bar{H}_{\text{sw}}^{\text{FM}}$.

In the recording process an external head field \mathbf{H}_{head} is turned on to switch the dots. This field is applied either parallel or tilted by θ_h with respect to the out-of-plane axis of the medium. The switching field of a dot also depends on the angle of the head (writing) field. Therefore, it would be necessary to simulate the magnetization reversal for all dots with the head field applied at different angles. The distribution curves in Figure 5.13 show the switching fields in case the external field is applied perpendicular to the medium. So if, for example, a perpendicular head field of $\|\mathbf{H}_{\text{head}}\| = 0.8\text{T}$ is chosen, all of the *FM(5)/FI(20)* dots would have been switched. But only less than half of the *FM(5)/FI(5)* dots and none of the *FM(5) only* dots. If the head field with the same magnitude is applied at $\theta_h = 10^\circ$, the switching fields are decreased. This means the distribution curves would shift to the left side and more of the *FM(5)/FI(5)* dots and the *FM(5) only* dots would be switched at $\|\mathbf{H}_{\text{head}}\| = 0.8\text{T}$. In terms of evaluating the number of switched dots, this is equivalent to keeping the perpendicular switching fields of the dots, but scaling (increasing) the used head field. Hence, for Figure 5.13 when changing the writing angle θ_h , one can either shift the distribution curves along the x -axis and keep the limiting head field constant, or keep the curves constant and shift the head field along the x -axis. The latter approach requires only the reversal simulations for a perpendicular head field and a correction function $c(\theta_h)$, which scales the head field according to its angle. Henceforth, the scaled head field is called effective field H_{head}^* .

For single phase dots, H_{head}^* can be calculated by using the Stoner-Wohlfarth

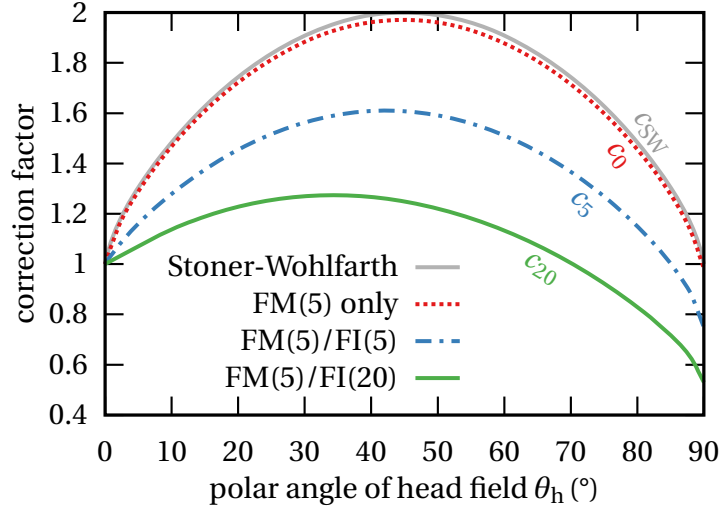


Figure 5.14: Correction functions for the angular variation of the switching field. The gray solid curve is the evaluated Stoner-Wohlfarth function c_{SW} in (5.9). The functions labeled according to the FI-layer thickness of the different island designs c_0 , c_5 and c_{20} are calculated numerically.

model [132, 136] described in Section 2.3.2. Hereby \mathbf{H}_{head} is scaled by the correction function c_{SW} derived from (2.54). The scaling depends on the angle θ_h between the applied head field and the anisotropic easy axis of the dots (out-of-plane):

$$c_{SW}(\theta_h) = (\sin^{2/3} \theta_h + \cos^{2/3} \theta_h)^{3/2}. \quad (5.9)$$

For the bilayer systems different angular dependencies are to be expected. Therefore, the micromagnetic model for FI/FM bilayer is used again to calculate the switching field at different angles θ_h and also express this angular dependence as correction functions. Since the functions also depend on the thickness of the FI-layer t_{FI} , the corresponding correction functions are labeled as $c_{t_{FI}}$. Figure 5.14 depicts the analytic Stoner-Wohlfarth correction function c_{SW} from (5.9) in gray and the simulated correction functions of three island designs. The effective head field is calculated by scaling the magnitude of \mathbf{H}_{head} with the respective correction function.

$$H_{\text{head}}^* = c_{t_{FI}}(\theta_h) \|\mathbf{H}_{\text{head}}\| \quad (5.10)$$

The numerically calculated correction function for the single ferromagnetic layer c_0 is very close to the theoretical c_{SW} . When adding the exchange coupled FI-layer the correction factor is generally reduced and even below 1 at higher angles. This means the switching field is less reduced by a tilted head field compared to single phase media or even increases at higher tilting angles. For bilayer islands the maxima of the

correction functions move to lower θ_h . In other words, for soft-hard bilayer structures the minimum switching field resides at lower angles than for single phase dots. This approach of an effective head field is used in Section 5.3.3 to calculate the switching probability and bit error rate of bit patterned media.

5.3.2 Dipolar interaction field in bit patterned media

For bit patterned media the bilayer dots need to be arranged in a periodic array. A single dot in this array does not only experience the field of a writing head, but also the stray field of all the other dots in the array. Naturally, the closer a neighboring dot is, the higher is the influence of its stray field on the examined dot. Therefore, with increasing areal density this field contribution can not be neglected and influences the performance of a recording medium [97]. The interaction field acting on a single dot is determined by the magnetic states, *i.e.* the stored bits, of all its neighbors. Hence, this field contribution is subject to fluctuations with a certain distribution. This dipolar interaction field distribution can be calculated by simulating the stray field of a dot array with randomly assigned magnetic configurations. In the center of the array a dot is left out where the interaction field is measured. By repeating this simulation, each time with a new randomly assigned initial magnetization, a histogram can be compiled. Fitting the histogram with a Gaussian curve reveals a dipolar interaction field distribution with a certain standard deviation σ_{dip} .

In order to set up the simulation for the stray field computation, arrays consisting of 11×11 dots are generated with the software Salome [124]. For this purpose the microstructure and the amorphous structure of the dots can be neglected since we are not interested in the switching of a dot but the stray field created by its magnetization. Therefore, for each dot design, arrays of equivalent dots are modelled with both layers having a perfect out-of-plane anisotropic easy axis. The ferrimagnetic layers are still exchange coupled. The intrinsic properties A_x , K_u and J_s are kept as defined in Table 5.2.

In the center of the 11×11 dot array one dot is left out. This gap marks the position where the dipolar interaction field \mathbf{H}_{dip} is measured. The dipolar field of these 120 dots is calculated by letting the system relax after randomly assigning an initial magnetization to each dot. To compile a histogram of the interaction fields, the simulation is repeated 500 times, assigning each time a new random initial magnetization. The simulation arrangement is illustrated in Figure 5.15 with two neighboring dots, their exerted stray field and the probe point in the gap, where \mathbf{H}_{dip} is determined. Of course the dipolar interaction field is strongly dependent on the density and pattern of the array. In this thesis arrays of quadratic and triangular distributed dots are investigated. For the quadratic patterned array the distance between two neighboring dots (pitch) in x - and y -direction is 40 nm. This array design was chosen to roughly resemble the dot arrays fabricated by our project partners at the Paul Scherrer Institute (PSI) in

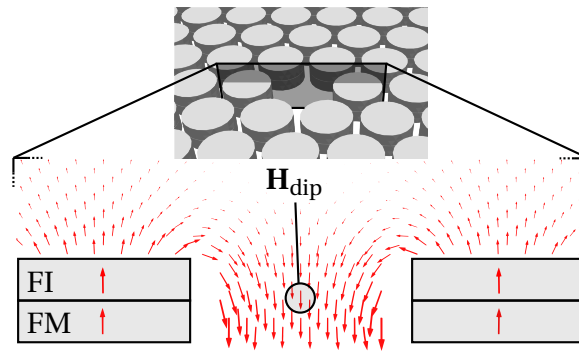


Figure 5.15: Schematic of the geometric simulation model to determine the dipolar interaction field \mathbf{H}_{dip} acting on a dot in an array of bilayer dots.

Switzerland [154]. It also matches the pitch reached by e-beam patterned exchange coupled composite square lattices reported in [4]. These dimensions translate to a 62 Gb/cm^2 ($\sim 400 \text{ Gb/in}^2$) recording medium. The triangular patterned array resembles bit patterned media with 220 Gb/cm^2 ($\sim 1.4 \text{ Tb/in}^2$) and has a x-pitch of 19.5 nm and a y-pitch of 22.5 nm .

A section of each bit array design with a virtual dot in the center is shown as an inset in Figure 5.16. The interaction field \mathbf{H}_{dip} is determined at the center of the virtual dot (the gap) at the position of the interface between the ferromagnetic and the ferrimagnetic layer. This choice of position is justified by the reversal mechanism in exchange coupled composite media, where the critical process is the expansion of a reversed domain into the hard magnetic phase (see Section 4.2). In Figure 5.16 the dipolar interaction field distributions for both array types and the three dot designs are shown. To ensure readability, the histograms are omitted and only the Gaussian fits of the out-of-plane component of the distributions h_{dip}^z are depicted.

Still, one example of a histogram is shown at the bottom inset to show the actual shape. The peaks in the histogram originate from the six closest neighboring dots, which have the highest influence on the dipolar field. The peaks correspond to certain magnetization configurations of these closest neighbors. This pattern dependent feature was also reported by Muraoka *et al.* [97]. When dot position jitter and dot size variation is introduced in the simulation, the peaks are less prominent and the distribution comes closer to the Gaussian fit. Each distribution is compiled from the result of 500 simulations. Here the out-of-plane (z -) component of the interaction field distribution was chosen, since this is presumed to be the dominant one. When the randomly magnetized dots in the array are relaxed, each dot has either an up or down state. Since these states are completely random, the stray fields cancel themselves out when averaging over 500 simulations. Hence, the resulting interaction fields in the virtual dot distribute around a mean value of zero.

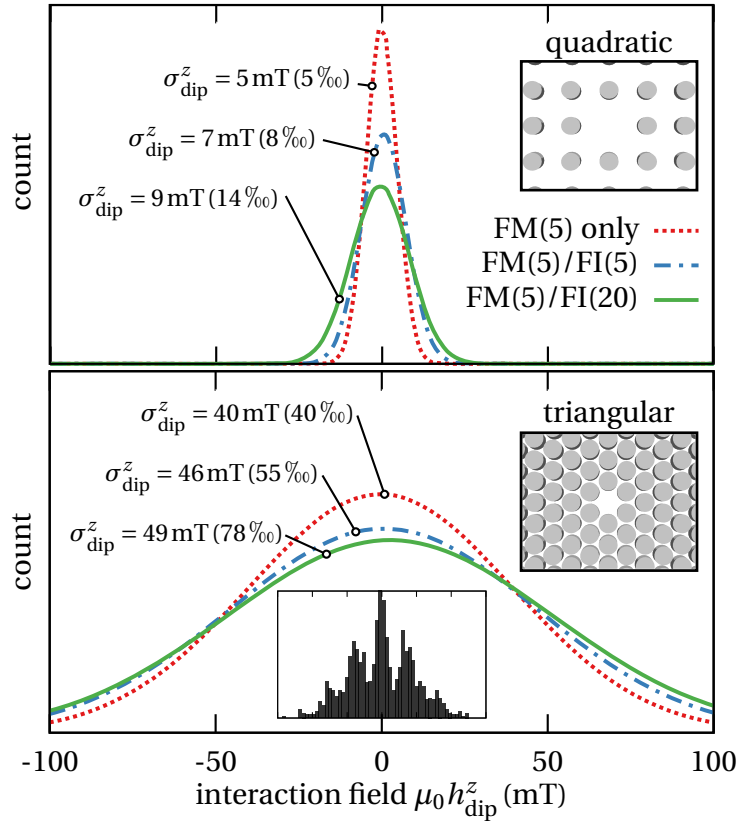


Figure 5.16: Gaussian fits of the dipolar interaction field component h_{dip}^z distribution for quadratic dot arrays (top) and triangular dot arrays (bottom) for the three dot designs shown in Figure 5.12. The standard deviation σ_{dip}^z is given in absolute values and as per mill of the respective mean switching field $\mu_0 \bar{H}_{\text{sw}}^z$. An example of a histogram is shown in the inset of the bottom graph.

For both patterns, quadratic and triangular, it can be seen that the interaction field distribution gets broadened with increasing FI-layer thickness. This can be attributed to the increased height of the magnetic dots when the soft FI-layer is added. The change of the dot shape increases the stray field acting on a neighboring dot. When adding the FI-layer, an increase in σ_{dip}^z of up to 23% (9 mT) can be observed for the triangular pattern. The increase for the quadratic patterned media is up to 80% (4 mT). Still, all the calculated values for σ_{dip}^z are below 9% of their respective mean switching field, for the quadratic pattern even below 2%. Of course, the interaction field values, and therefore the standard deviation values of the triangular patterned array are higher since the neighboring dots are much closer to each other. Hence, the stray field measured in the virtual dot is increased.

To test the influence of the number of considered neighboring dots, the 500 simu-

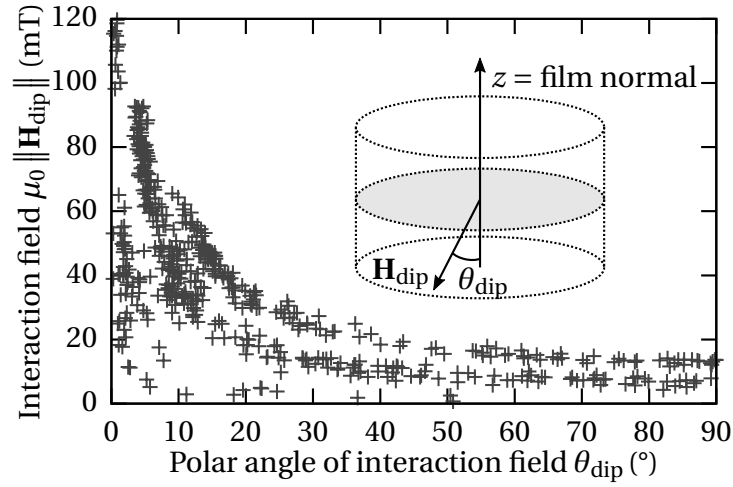


Figure 5.17: Magnitude of the interaction field plotted against the respective polar angle θ_{dip} for 500 simulation runs of $FM(5)/FI(5)$ dot arrays with random initial magnetization.

lations with random initial magnetization were also done for a 17×17 triangular array with the same pitches. The maximum deviation of σ_{dip}^z due to the larger array was found to be 0.55 mT for $FM(5)/FI(20)$ dots. Therefore, the choice of 11×11 -arrays is considered sufficient in order to save computing time while still obtaining meaningful distribution values.

In Figure 5.16 only the out-of-plane component of all 500 probe points of the stray field simulations is considered to fit a distribution curve. It remains to investigate the influence of the interaction field at other angles. In Figure 5.17 the relation between the polar angle of the interaction fields θ_{dip} and its magnitude $\|\mathbf{H}_{\text{dip}}\|$ is plotted. Only the 500 dipolar field vectors of the $FM(5)/FI(5)$ dot arrays are depicted. The inset shows the virtual dot, where the dipolar field with its deviation angle is measured at the interface of the two layers.

In general, higher interaction fields can be observed at smaller angles. The results indicate, that in a configuration that leads to an interaction field with a high angle, the field is small. Further, the most points in Figure 5.17 are located in the range from 0° to 20° . This means that field vectors with a dominant z -component have a higher magnitude and therefore contribute more to the dipolar interaction field distribution. Hence, the distributions and standard deviations for h_{dip}^z shown in Figure 5.16 might already be a sufficient approximation to characterize the dipolar field contribution of bit patterned media.

Nonetheless, for further calculations, especially for bit error rates in Section 5.3.3, all three orthogonal components of \mathbf{H}_{dip} should be considered. As described in previous Section 5.3.1 a head field needs to be applied to write (*i.e.* switch) the dots. When

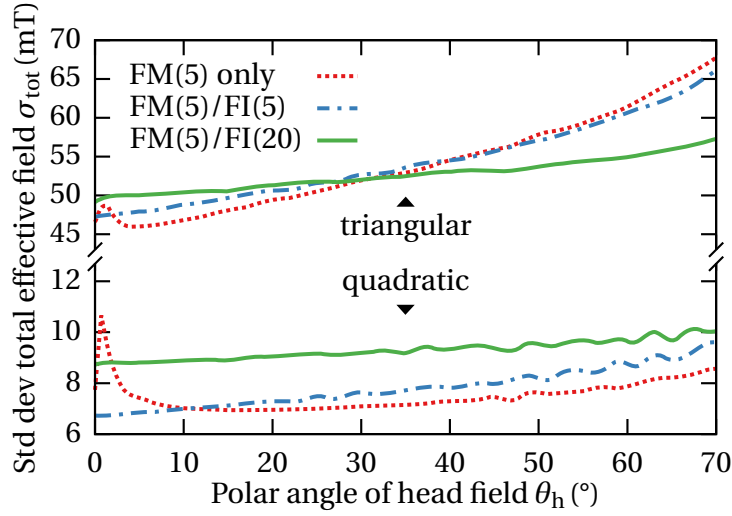


Figure 5.18: Standard deviation σ_{tot} of the total effective field H_{tot}^* depending on the polar angle of the head field θ_h for both patterns, triangular (top three curves) and quadratic (bottom three curves), and all three dot designs.

the dipolar interaction field is included in the calculation, the field acting on one dot is changed. Instead of just the head field from the writing head, it is now the sum of the current head field and the interaction field.

$$\mathbf{H}_{tot} = \mathbf{H}_{head} + \mathbf{H}_{dip} \quad (5.11)$$

Again, either the perpendicular component of the total field can be used [26], or it can be corrected by the angular variation of the switching field [121, 47] obtaining a total effective field:

$$H_{tot}^* = c_{t_{FI}}(\theta_{tot}) \|\mathbf{H}_{head} + \mathbf{H}_{dip}\| \quad (5.12)$$

Here θ_{tot} is the angle between the total field \mathbf{H}_{tot} and the anisotropic easy axis of the dots. The total field is scaled by the correction function $c_{t_{FI}}$ introduced in Section 5.3.1 and depicted in Figure 5.14. Because the dipolar interaction field is incorporated, the total effective field H_{tot}^* has the distribution of \mathbf{H}_{dip} imprinted. From the 500 previously calculated \mathbf{H}_{dip} , for each head field angle θ_h 500 total fields \mathbf{H}_{tot} can be computed. Using (5.12) the field values can be scaled according to their angle θ_{tot} to gain the effective field. Subsequently, for each θ_h a standard deviation of the 500 H_{tot}^* values can be calculated. This procedure is done for both media patterns and the three individual dot designs. In Figure 5.18 the standard deviation of the total effective field σ_{tot} is plotted against the head field angle θ_h .

The much denser triangular patterned medium (top curves) has a much higher standard deviation of the effective field, regardless of the polar angle of the head field,

Table 5.3: Minimal and maximal standard deviation σ_{tot} depending on the head field angle θ_h (values in brackets) from Figure 5.18.

		dot design	σ_{tot} (mT) (at θ_h (°))		
			min	max	
quadratic	<i>FM(5) only</i>	7	(16)	11	(1)
	<i>FM(5)/FI(5)</i>	7	(1)	10	(70)
	<i>FM(5)/FI(20)</i>	9	(0)	10	(67)
triangular	<i>FM(5) only</i>	46	(5)	68	(70)
	<i>FM(5)/FI(5)</i>	47	(0)	66	(70)
	<i>FM(5)/FI(20)</i>	49	(0)	57	(70)

compared to the quadratic array (bottom curves). Generally it can be stated, that with increasing polar angle the standard deviation σ_{tot} increases. The thicker the ferrimagnetic layer gets, the lesser is the change of σ_{tot} with increasing θ_h . This is true for all dot designs and array designs with the exception of the range $\theta_h = 0$ to 10° for the *FM(5) only* dots. For both patterns the standard deviation increases in this range noticeably. By adding the ferrimagnetic layer these peaks are removed. In Table 5.3 the maxima and minima of σ_{tot} with the respective head field angle are listed for each pattern and dot design.

The values of σ_{dip}^z presented in Figure 5.16 are very close to the effective standard deviation values σ_{tot} in Table 5.3. Also, the maximum deviation of σ_{tot} that can be created by tilting the head field was 4 mT for the quadratic pattern and 22 mT for the triangular pattern, in both cases for the *FM(5) only* design. Compared to the switching field of 1 T, these values are very small and indicate that often an approximation with the distribution of the out-of-plane component σ_{dip}^z is sufficient.

5.3.3 Bit error rate of bilayer dot arrays

There are many sources of error in bit patterned media recording and it is hard to meet requirements for the fabrication process. For example, the dot array will have position jitter, since not all dots reside in the perfect position of the pattern. Also the dots might not all have the exact same size, which again introduces some noise [131]. In the currently used perpendicular magnetic recording (PMR) media a bit is stored on a cluster of about 20-50 magnetic grains. With decreasing number of grains per bit, read back errors increase due to decreasing signal to noise ratio (SNR). For bit patterned media, where a bit is stored on just a single dot, the SNR depends only on the variation of the dot properties. Read back errors are often called *soft errors*, because they can be

eliminated by employing error-correcting codes to a certain degree. *Hard errors*, on the other hand, are errors due to incorrectly written bits, which are far more difficult to correct for. Studies show, that the recording performance of bit patterned media is dominated by these written-in errors [122]. A final bit error rate has to consider all possible sources of noise, starting from the fabrication process, over recording process and also the read back process [122, 120]. Acceptable bit error rates are in the range of 10^{-4} to 10^{-2} [26, 4].

In this section however, a bit error rate is defined to merely characterize the simulated media with the three different dot designs and the two array patterns. The goal is to compare performance of the exchange coupled dots to the single phase dot and look at the influence of the array pattern. Only the switching field distribution and the dipolar interaction field distribution are considered. Moreover, the head field angle dependence is investigated. Therefore, the simulation results from previous sections 5.3.1 and 5.3.2 can be used.

The probability of switching a single dot can be calculated using the intrinsic switching field distribution, fitted by a Gaussian curve (5.8). With the respective effective head field H_{head}^* as upper limit, the probability of switching the dots is given by [96]:

$$p_{\text{sw}} = \frac{1}{\sigma_{\text{int}}\sqrt{2\pi}} \int_{-\infty}^{H_{\text{head}}^*} \exp\left(-\left(\frac{h - \bar{H}_{\text{sw}}}{\sigma_{\text{int}}\sqrt{2}}\right)^2\right) dh \quad (5.13)$$

$$= \frac{1}{2} \left(1 + \operatorname{erf}\left(\frac{H_{\text{head}}^* - \bar{H}_{\text{sw}}}{\sigma_{\text{int}}\sqrt{2}}\right) \right). \quad (5.14)$$

The bit error rate for a set of isolated dots with an intrinsic switching field distribution of σ_{int} is $p_{\text{err}}^{\text{int}} = 1 - p_{\text{sw}}$ or

$$p_{\text{err}}^{\text{int}} = \frac{1}{2} \left(1 - \operatorname{erf}\left(\frac{H_{\text{head}}^* - \bar{H}_{\text{sw}}}{\sigma_{\text{int}}\sqrt{2}}\right) \right). \quad (5.15)$$

The diagram in Figure 5.19 shows the Gaussian function that can be used to fit the intrinsic switching field distribution $f(h)$ (solid line) from (5.8) and the applied effective field H_{head}^* . Dots with a switching field $H_{\text{sw}} > H_{\text{head}}^*$ (hatched area) cannot be switched and cause bit errors. The corresponding bit error rate $p_{\text{err}}^{\text{int}}$ depending on H_{head}^* from (5.15) is shown as a dashed line.

The intrinsic bit error rate might already be a good first estimate for the performance of a bit pattern medium. It is the error rate of perfectly isolated dots with variations only in microstructure and anisotropy properties of the dots. However, with increasing areal density the dots cannot be considered isolated any more. The dipolar interaction field exerted by each dot influences the switching behavior of the other

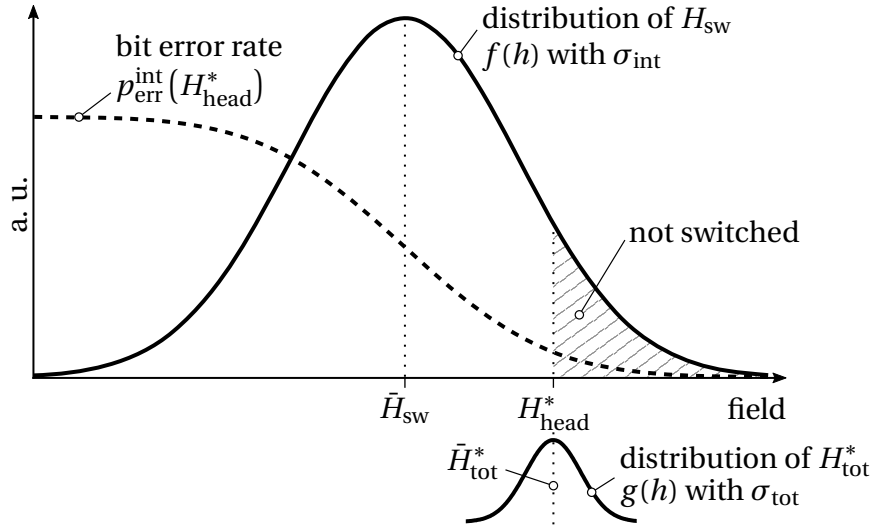


Figure 5.19: Schematic of the bit error rate calculation. If the dipolar field is neglected the intrinsic switching field distribution (solid line) and the applied field H_{head}^* determine the bit error rate p_{err}^{int} (dashed line) according to (5.15), since islands with $H_{sw} > H_{head}^*$ can not be switched (hatched area). When also taking into account the dipolar field, H_{tot}^* is applied with the distribution of the dipolar field $g(h)$.

dots in the array. In Section 5.3.2 the dipolar interaction field \mathbf{H}_{dip} acting on a dot is calculated for 500 different randomized magnetic configurations of the dot array. By combining the dipolar field values with the applied effective head field H_{head}^* , a distribution of the total effective field H_{tot}^* is calculated. This distribution again can be approximated by a Gaussian fit:

$$g(h) = \frac{1}{\sigma_{tot}\sqrt{2\pi}} \exp\left(-\left(\frac{h - \bar{H}_{tot}^*}{\sigma_{tot}\sqrt{2}}\right)^2\right). \quad (5.16)$$

Now, instead of applying the effective head field H_{head}^* , the total effective field H_{tot}^* is applied. Contrary to H_{head}^* , the total effective field carries the distribution $g(h)$ of the dipolar interaction field (smaller distribution curve in Figure 5.19). By integrating over the product of the total effective distribution $g(h)$ and the bit error rate of isolated islands p_{err}^{int} , the overall bit error rate p_{err}^{tot} can be computed.

$$p_{err}^{tot} = \int_{-\infty}^{\infty} \frac{g(h)}{2} \left(1 - \operatorname{erf}\left(\frac{h - \bar{H}_{sw}}{\sigma_{int}\sqrt{2}}\right)\right) dh \quad (5.17)$$

As described in Section 5.3.1 and Section 5.3.2 it can be stated, that adding the FI-layer narrows the intrinsic switching field distribution but broadens the distribution of the

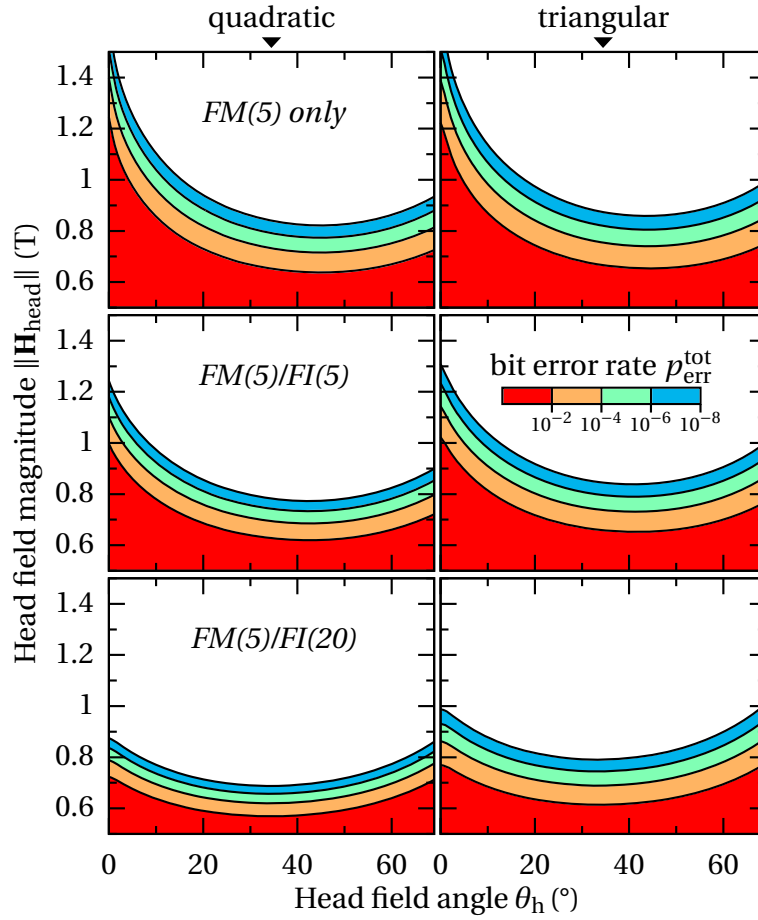


Figure 5.20: Total bit error rate $p_{\text{err}}^{\text{tot}}$ (iso-lines and color code) depending on head field magnitude (y-axis) and head field angle (x-axis). The error rate is depicted with a logarithmic scale for the two array patterns (columns) and the three dot designs (rows). White areas are for bit error rates $< 10^{-8}$.

interaction field acting on a dot. Calculating the total bit error rate considers both distributions and expresses the performance of the media in a single value. Moreover, $p_{\text{err}}^{\text{tot}}$ also incorporates the angular variation of the head field. The calculations are again done for the three island configurations: single FM-layer with 5 nm thickness (*FM(5) only*) and exchange coupled bilayers with 5 nm (*FM(5)/FI(5)*) and 20 nm FI-layer (*FM(5)/FI(20)*) on top of the FM-layer. In Figure 5.20 the total bit error rate is depicted, depending on the head fields magnitude $\|\mathbf{H}_{\text{head}}\|$ and its field angle θ_h . The colors of the bit error rate are scaled logarithmically (see color key bar), values smaller than 10^{-8} are represented by white areas. The diagrams are for the three dot designs (rows) and the two array patterns (columns). The axes scales are kept equal for all six

diagrams to make them visually comparable.

The angular dependence of the required head field for a certain bit error rate $p_{\text{err}}^{\text{tot}}$ can be clearly seen in all six diagrams. This behavior is mainly governed by the correction functions shown in Figure 5.14 (p. 84). With increasing FI-layer thickness, the influence of θ_h is less pronounced. This is true for both array patterns and caused by the reduced switching field of bilayer dots. Using the triangular pattern and a bit error rate of 10^{-4} , the head field can be reduced by a maximum of 650 mT for *FM(5) only* dots, but by just 170 mT for *FM(5)/FI(20)* dots by only adjusting the angle. Adding the ferrimagnetic layer the minima of the required head field for a certain bit error rate shifts towards lower angles. In the just given example, the minimum shifts from 44° (740 mT) for *FM(5) only* dots to 33° (690 mT) for *FM(5)/FI(20)* dots. This shift could already be observed in the maximums of the calculated correction functions in Figure 5.14. The influence of the dipolar interaction field can be seen when comparing the graphs of the quadratic pattern (left column) with those of the triangular pattern (right column). Since the triangular pattern has a higher areal density, the acting dipolar field as well as its standard deviation is increased. Therefore, to achieve the same total bit error rate, the applied head field must be higher for triangular patterned media. To achieve a bit error rate of 10^{-4} at the optimal angle the head field has to be increased by 24 mT when moving from a quadratic to the denser triangular pattern of *FM(5) only* dots. If a 20 nm thick FI-layer is added, an increase of 65 mT in H_{head} is needed, due to the increased dipolar interaction field. In order to look specifically at the influence of the dipolar field, the two previously described bit error rates $p_{\text{err}}^{\text{int}}$ and $p_{\text{err}}^{\text{tot}}$ are computed separately:

$p_{\text{err}}^{\text{int}}$ The dipolar interaction field is neglected and therefore an array of isolated dots is assumed. An effective field (5.10) is applied and $p_{\text{err}}^{\text{int}}$ is calculated according to (5.15).

$p_{\text{err}}^{\text{tot}}$ The dipolar interaction field is incorporated by imprinting its distribution onto the effective field using (5.12). The total bit error rate $p_{\text{err}}^{\text{tot}}$ is then calculated according to (5.17).

In Figure 5.21 $p_{\text{err}}^{\text{int}}$ is plotted along the total bit error rate $p_{\text{err}}^{\text{tot}}$ for $\theta_h = 0^\circ$ and 40° against the effective head field. Because H_{head}^* is used on the x -axis, the angular dependence of the switching field is removed from the curves and only the influence of the dipolar interaction field can be compared. Hence, even though Figure 5.21 and Figure 5.20 are compiled from the same data, the $p_{\text{err}}^{\text{tot}}$ -curves cannot be compared directly. For $p_{\text{err}}^{\text{int}}$, a change in θ_h only changes H_{head}^* and therefore does not alter the curves.

As shown in Section 5.3.1, the switching field is decreased when adding the exchange coupled FI-layer. Therefore a strong reduction of the bit error rate is observed for a given effective head field H_{head}^* with increasing t_{FI} , regardless of the array pattern.

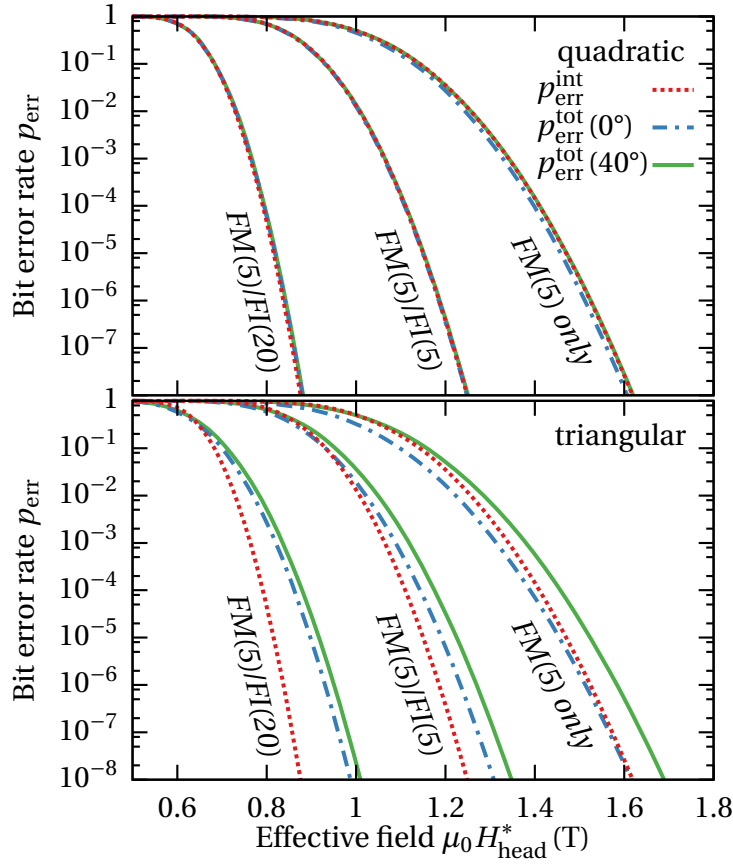


Figure 5.21: Calculated bit error rates for the three dot designs and two array patterns quadratic (top) and triangular (bottom). The bit error rate without dipolar field contribution $p_{\text{err}}^{\text{int}}$ is shown as red dotted line. The bit error rate incorporating the dipolar field contribution $p_{\text{err}}^{\text{tot}}$ is calculated for a perpendicular head field ($\theta_{\text{h}} = 0^\circ$) (blue dash-dotted line) and for $\theta_{\text{h}} = 40^\circ$ (green solid line).

The reduction of the switching field by such a bilayer dot design clearly plays the dominating role in reducing the bit error rate.

The bit error rate curves $p_{\text{err}}^{\text{int}}$ and $p_{\text{err}}^{\text{tot}}$ (for both angles) for the quadratic array pattern (top graph) show almost equal values along the whole effective field range, for each dot design. This means, that there is almost no influence of the dipolar interaction field as previously suggested because of the relatively high pitch of 40 nm, *i.e.* low areal density. However, the curves for the triangular array pattern (bottom graph) suggest that the dipolar interaction field has a significant impact. Since the $p_{\text{err}}^{\text{int}}$ curves (red dotted lines) only incorporate the intrinsic switching field distribution, they are equal for the two array patterns. The discrepancy between the $p_{\text{err}}^{\text{int}}$ curves and the $p_{\text{err}}^{\text{tot}}$ curves increases with increasing FI-layer thickness t_{FI} . This is because

Table 5.4: Switching field distribution and bit error rate for the three island designs: *FM(5) only*, *FM(5)/FI(5)* and *FM(5)/FI(20)* bilayer in triangular patterned arrays. The lines with $p_{\text{err}}^{\text{int}}$ give the minimum required head field when the dipolar interactions are neglected, while the lines with $p_{\text{err}}^{\text{tot}}$ take the dipolar interactions into account. The required head fields are listed for a bit error rate of $p_{\text{err}} = 10^{-6}$ at two different head field angles $\theta_h = 0^\circ$ and 40° .

		FM(5)/FI(t_{FI})	(nm)	0	5	20
		$\mu_0 \bar{H}_{\text{sw}}$	(mT)	1001	838	626
		σ_{int}	(mT)	110	73	45
		σ_{dip}^z	(mT)	40	46	49
$p_{\text{err}} = 10^{-6}$	0°	$\mu_0 \ \mathbf{H}_{\text{head}}\ (p_{\text{err}}^{\text{int}})$	(mT)	1524	1186	838
		$\mu_0 \ \mathbf{H}_{\text{head}}\ (p_{\text{err}}^{\text{tot}})$	(mT)	1513	1234	931
		σ_{tot}	(mT)	47	47	49
	40°	$\mu_0 \ \mathbf{H}_{\text{head}}\ (p_{\text{err}}^{\text{int}})$	(mT)	765	741	665
		$\mu_0 \ \mathbf{H}_{\text{head}}\ (p_{\text{err}}^{\text{tot}})$	(mT)	808	790	750
		σ_{tot}	(mT)	54	54	53

σ_{int} decreases while σ_{dip} , and consequently σ_{tot} , increases slightly and contributes more to the total bit error rate. For example, the *FM(5)/FI(20)* dot design at an effective head field of $H_{\text{head}}^* = 838 \text{ mT}$ shows a bit error rate of $p_{\text{err}}^{\text{int}} = 10^{-6}$, but a much higher bit error rate of $p_{\text{err}}^{\text{tot}} = 10^{-3}$ when the dipolar interaction field is incorporated. From Figure 5.18 it is known, that with increasing head field angle θ_h the standard deviation of the total effective write field σ_{tot} increases owing to dipolar interactions. Moreover, with increasing thickness of the FI-layer, a change of θ_h has less influence on σ_{tot} . Both effects can also be seen in Figure 5.21. At a head field angle of $\theta_h = 40^\circ$ the total bit error rate (green solid line) is always higher than $p_{\text{err}}^{\text{tot}}$ at $\theta_h = 0^\circ$ (blue dash-dotted line). The difference between the two $p_{\text{err}}^{\text{tot}}$ curves decreases with increasing t_{FI} . Therefore, for higher values of t_{FI} the difference might be negligible.

In Table 5.4 results of the investigation of switching field distribution in triangular bit patterned media are summarized. The table gives the minimum required head field to reach a bit error rate of $p_{\text{err}} = 10^{-6}$. A table for the quadratic patterned arrays is omitted, since the dipolar interaction field barely affects the bit error rate. The standard deviation of the intrinsic and the dipolar contribution to the switching field distribution as well as the switching fields are listed for the three island designs.

Moreover, the respective minimum required head field magnitudes and effective head fields for a given bit error rate of $p_{\text{err}}^{\text{int}} = p_{\text{err}}^{\text{tot}} = 10^{-6}$ are shown for a perpendicular head field ($\theta_h = 0^\circ$) and a head field angle of $\theta_h = 40^\circ$.

From this point of view, if the dipolar field is neglected, the required head field for $p_{\text{err}}^{\text{int}} = 10^{-6}$ at $\theta_h = 0^\circ$ is reduced by 686 mT (from 1524 mT to 838 mT) when a 20 nm FI-layer is added. At a writing angle of $\theta_h = 40^\circ$ the required head field is generally lower and only reduced by up to 100 mT by the additional FI-layer. If the dipolar field is incorporated in the bit error rate calculation $p_{\text{err}}^{\text{tot}} = 10^{-6}$, the required head field is reduced to 931 mT at $\theta_h = 0^\circ$ or to 750 mT at $\theta_h = 40^\circ$ by the coupled FI-layer. In other words, when taking the dipolar field into account, a significant reduction of the required writing field can still be seen, but only by 38% (at 0°) or by just 7% (at 40°) as opposed to the 45% (at 0°), or 13% (at 40°) gained when neglecting \mathbf{H}_{dip} . While the standard deviation of the dipolar field is about half of the intrinsic standard deviation for *FM(5) only* dot arrays, for the *FM(5)/FI(20)* dot arrays the two contributions are equally affecting the bit error rate.

5.4 Further characterization of dots in bit patterned media

Even though the fabrication of bit patterned media has been improved significantly [4], there are still challenges ahead to finally make the technology ready for the consumer market. In order to achieve low bit error rates with bit patterned media, it is important to have highly uniform switching field over all dots. The intrinsic switching field of the dots and its distribution is discussed in Section 5.3.1, where microstructural and anisotropic property variations are considered. However, there are additional sources which increase the standard deviation of the switching field [111]. In this section two of these sources are investigated to evaluate their impact: redeposited material at the sidewalls of the dots during the fabrication process and irregularly shaped dot edges. At the PSI in Switzerland, Weber *et al.* investigated new approaches to fabricate high-density bilayer dot arrays with highly uniform properties [154]. Their work provided the basis to model dots with rough edges and redeposited material.

5.4.1 Switching field reduction by redeposition

In the work of Weber *et al.* [154] the dot arrays are produced by masking a thin FePt/FeGd bilayer film on a MgO substrate with a C-Si mask, and structure the film by Ar ion beam etching (IBE). The mask is removed by reactive ion etching (RIE) using SF₆ plasma. Finally, the array is coated with a Pt layer to protect from oxidation. Figure 5.22 shows scanning electron transmission (SEM) images of bilayer dots in an

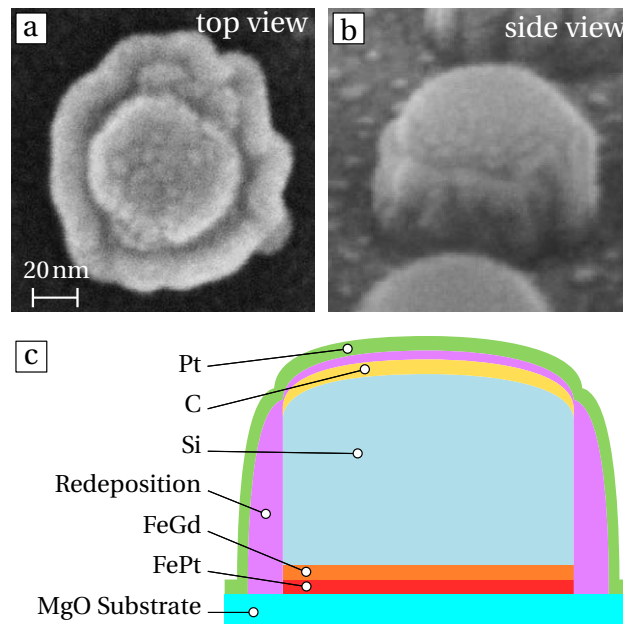


Figure 5.22: Top [a](#) and side view [b](#) of bilayer dots with a diameter of about $d = 70$ nm in arrays fabricated at PSI (SEM images are courtesy of A. Weber and E. Kirk). The schematic [c](#) shows the setup of the imaged dots.

array fabricated at PSI, a top view [a](#) and a side view at an 45° angle [b](#). A schematic of the imaged dots is shown in [c](#).

For the imaged dots the mask removal was not successful due to redeposition on the mask during IBE. Therefore the dots in Figure 5.22 [a](#) and [b](#) show the setup depicted in the schematic [c](#): The C-Si mask is still intact because of the redeposition on top of it and the whole dot is covered in Pt. However, significant amount of redeposited material at the sidewall of the dot can be seen in the SEM images. Eventually, by etching at 30° for a sufficient amount of time (about 6 min) the mask and redeposited material can be removed, but it still remains some redeposited material at the sidewalls of the bilayer dots.

The actual material composition of the redeposition is unknown, but an estimate can be made. The material will be mostly redeposited Si from the mask and FePt and FeGd from the bilayer. To model the problem in the simulation a worst case scenario was chosen with 40% FePt, 40% FeGd and 20% nonmagnetic material. The redeposited material is assumed to be ferromagnetic with zero magnetocrystalline anisotropy and $J_s = 0.6$ T, $A_x = 3.8$ pJ/m. The magnetic properties for the bilayer dot are kept as listed in Table 5.2. A model for a bilayer dot is reused from previous investigations in Section 5.3 with a diameter of $d = 20$ nm and layer thickness of $t_{FI} = t_{FM} = 5$ nm ($FM(5)/FI(5)$ in Figure 5.12). A redeposition layer of varying thickness

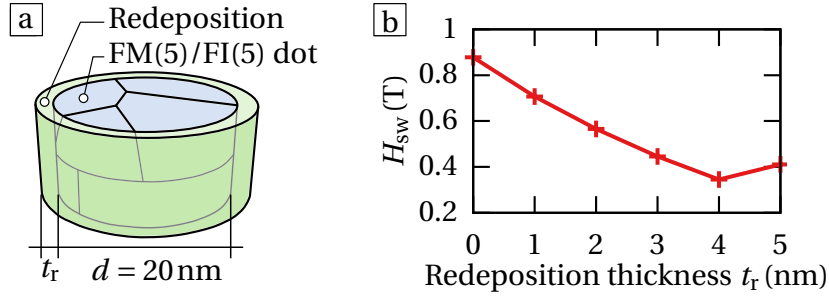


Figure 5.23: Schematic of the used bilayer dot model with a layer for redeposited material at the sidewalls [a] and the reduction of the switching field due to the redeposition [b].

$t_r = 1$ to 5 nm is wrapped around the sidewalls of this bilayer dot. The redeposited material is exchange coupled to the FePt and FeGd in the dot. A schematic of the model is shown in Figure 5.23 [a].

The reversal curves of dots with different thickness of redeposition layer t_r are calculated. In Figure 5.23 [b] the switching field $H_{sw} := H_{ext}(M_z = 0)$ is plotted against t_r . Redeposited material at a thickness of $t_r = 4$ nm reduces the switching field by 60% from 878 mT to 345 mT. At $t_r = 5$ nm the switching field increases slightly. This is due to a change in reversal mode. At $t_r \lesssim 4$ nm the dot and the redeposited material exhibit a quasi simultaneous reversal. At higher t_r a 90° domain wall is formed at the interface of the dot and the redeposition ring. In other words, while the magnetization of the dot is still pointing out-of-plane, the redeposition ring's magnetization is in-plane until the whole model switches with increasing external field H_{ext} .

Although the simulated scenarios are believed to be the worst case, it can be assumed that any redeposition has significant effect on the switching field. Generally, a reduction of the switching field is not a disadvantage, since this is actually a main reason to add a FI layer in the first place. If the amount of redeposited material during the fabrication process of the dot arrays can be controlled, the switching field of the array could be tailored to fit specific needs. The significant influence also shows, that an uniform redeposition across the whole array is important. Otherwise, the switching field distribution would increase drastically.

5.4.2 Effect of dot edge roughness

In this section the effect of irregularly shaped dots on the switching field distribution of dot arrays is investigated. In the SEM images of fabricated dots in Figure 5.22 the roughness of a dot's edge cannot be directly seen because of the redeposited material.

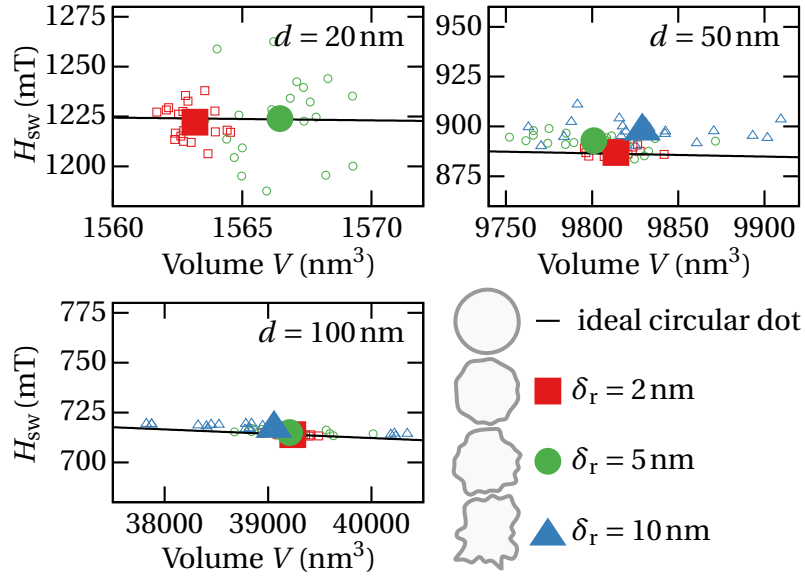


Figure 5.24: Switching field distribution due to dot edge roughness for three different dot diameters $d = 20$ nm, 50 nm and 100 nm. The switching field H_{sw} for ideal circular dots is depicted as the solid lines, while the different roughness degrees are marked by the colored symbols shown in the key at the bottom right. For each roughness degree an example of the dot edge shape is given in the key. The big full markers show the mean values of the respective 20 H_{sw} values depicted as smaller open markers.

Still, one can assume some roughness on the sidewalls, since also the redeposited material clearly shows an irregular shaped edge.

In order to estimate the influence of the dot edge roughness, new models of dots have to be generated with Salome [124]. For simplicity, the FI layer is omitted and only a $t_{FM} = 5$ nm thick FePt layer is used for the simulation. The edge roughness is created by adding a random deviation $\pm\delta_r$ to the radius r_{ideal} of an ideal circular dot every 4 nm along the perimeter. To avoid too drastic changes of the radius, the radius of every deviating point is weighted with the radius of the previous point: $r^{i+1} = 0.7(r_{ideal} + \text{random}(-\delta_r, \delta_r)) + 0.3r^i$. Here $\text{random}(a, b)$ is a uniformly distributed number from the interval (a, b) . A B-spline is then interpolated onto the set of points to form the rough edge. The spline is closed and transformed into a face which is subsequently extruded in height by 5 nm to a solid representing the FePt-dot. Examples of dots with different degree of roughness are shown at the bottom right hand side of Figure 5.24. A finite element mesh of the dot is generated [126] with a mesh size of 1 nm. The whole generation process is automated by a Python script [113] to easily prepare and launch high numbers of simulations.

The properties for the FePt single-layer dots are taken from Table 5.2. Magnetization reversal curves for three dot diameters are computed: $d = 20$ nm, 50 nm and 100 nm. For each of this diameters different degrees of roughness are applied: $\delta_r = 2$ nm, 5 nm and 10 nm. Per diameter and δ_r , 20 dots are generated with random roughness. Dots with $d = 20$ nm and $\delta_r = 10$ nm are omitted, since the maximal deviation is equal to the radius of the dot and therefore too big. For each dot the switching field is evaluated by computing the reversal curve. In Figure 5.24 for each dot diameter a diagram with the switching fields is depicted.

Because the introduction of edge roughness comes with a volume change of the dot, the switching fields are plotted against their respective dot volume. The height of the dot is fixed to 5 nm. Changes in volume thus reflect a change in the effective diameter. The switching field axis (y-axis) of the three diagrams have the same scaling, but are in different field ranges. The solid black lines mark the H_{sw} of the ideal circular dots at the respective volume. The 20 different switching fields for each roughness degree are shown as open markers. Their respective mean values are marked with the big filled symbols.

The deviations of the switching fields of irregularly shaped dots from the fields of circular dots are within a range of 40 mT for $d = 20$ nm and decrease with increasing dot diameter. Also, as one would expect, the switching field distribution is increasingly broader with increasing δ_r . Generally, it cannot be said that dots with a rough edge have a higher or lower H_{sw} compared to a circular dot with the same volume. The switching fields can be found above and below the solid line. But for dots with $d = 50$ nm and $d = 100$ nm most switching fields are slightly higher with increasing roughness.

In order to calculate a standard deviation of the switching field distribution caused by roughness, the influence of the volume is eliminated. Of course, volume distribution among the dots is also a source of the switching field distribution, but here only the influence of the edge roughness is investigated. The difference $H_{sw,i}^\Delta$ between the calculated switching fields $H_{sw,i}^r$ and their corresponding switching field of the circular dot at the same volume V_i are used to calculate the standard deviation σ_r as in (5.19). In Table 5.5 the statistic results are summarized.

$$H_{sw,i}^\Delta = H_{sw,i}^r(V_i) - H_{sw}(V_i) \quad (5.18)$$

$$\sigma_r = \sqrt{\frac{1}{n-1} \sum_{i=1}^n \left(H_{sw,i}^\Delta - \bar{H}_{sw}^\Delta \right)^2} \quad (5.19)$$

Compared to the intrinsic standard deviation σ_{int} and the distribution of the dipolar interaction field σ_{dip} , the standard deviation of the switching field caused by the dot roughness σ_r is low. For a *FM(5)/FI(5)* bilayer dot with $d = 20$ nm, the standard deviations $\sigma_{int} = 73$ mT and $\sigma_{dip}^z = 46$ mT were calculated and $\sigma_r = 21$ mT in case of $\delta_r = 5$ nm. σ_r is expected to be even lower, since only a single FePt layer was modeled

Table 5.5: Standard deviations σ_r and maximal deviations $H_{sw,max}^\Delta$ for the three diameters and roughness degrees δ_r are given in absolute values and per mill of the ideal circular dot's switching field H_{sw} .

dot diameter d		(nm)	20	50	100
ideal	H_{sw}	(mT)	1223	886	714
$\delta_r = 2$	σ_r	(mT)	9	2	0.2
		(‰)	7	2	0.3
	$H_{sw,max}^\Delta$	(mT)	18	5	0.4
		(‰)	14	5	0.6
$\delta_r = 5$	σ_r	(mT)	21	4	0.9
		(‰)	17	4	1.3
	$H_{sw,max}^\Delta$	(mT)	39	12	3.0
		(‰)	32	14	4.2
$\delta_r = 10$	σ_r	(mT)	-	5	0.9
		(‰)	-	6	1.3
	$H_{sw,max}^\Delta$	(mT)	-	25	4.8
		(‰)	-	28	6.7

and δ_r is not expected to be that high in reality. Therefore the dot edge roughness has only less than half the influence on the switching field distribution than the dipolar interaction field, and may be neglected in most cases.

5.5 Read back field of bilayer dots

In Section 5.3.3 it was already mentioned, that read back errors play a vital role in the overall bit error rate of recording media. When a soft ferrimagnetic layer is added on top of the hard magnetic storage layer (usually FePt) the exerted magnetic field is expected to be reduced due to the ferrimagnet's lower magnetization. Naturally, this decreases the signal to noise ratio (SNR) during readback. The SNR also depends on the read head design and noise sources like dot position jitter or dot size variation. In order to assess the the read back performance of the bit patterned media, read back calculations can be done with a reciprocity reader approach [27, 131]. However, here the investigation is limited to the exerted stray field of the three dot designs, *FM(5) only*, *FM(5)/FI(20)* and *FM(5)/FI(20)*, to evaluate the effect of the added FI-layer. The properties for dots in the simulation are kept as listed in Table 5.2.

Using *FEMME* [128], the field above the dots is computed, where the read head

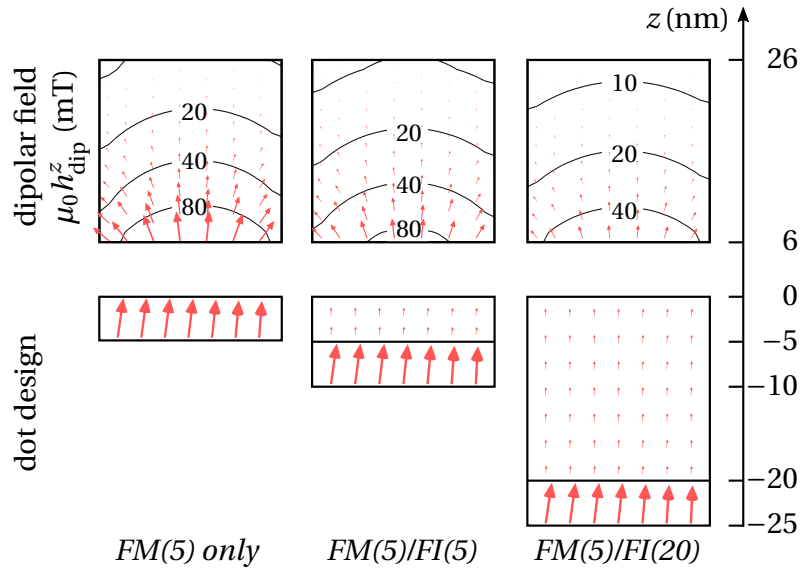


Figure 5.25: Calculated stray field (upper boxes) of three single dot designs (lower boxes) with a diameter of $d = 20\text{ nm}$ experienced by a read head with a magnetic spacing of 6 nm . The magnetic moments in the dots layers and the stray field above the dots are shown as red arrows. The iso-lines in the field boxes show the stray field in mT.

would be positioned. A non-magnetic spacing between medium and read head of 6 nm is assumed. The upper boxes in Figure 5.25 show a map of the perpendicular magnetic field component h_{dip}^z using iso-lines, corresponding to the respective dot below each box. The actual magnetostatic field direction is depicted by the red arrows in the boxes. The magnetization configurations in the two layers is also shown by arrows.

As expected the field decreases with increasing ferrimagnetic layer thickness. This is because the distance to the FM-layer with high magnetization is increased and the added ferrimagnetic FeGd has low magnetization indicated by the small arrows in the FI-layers. The maximum perpendicular field component h_{dip}^z is 135 mT at the bottom of the field box for a *FM(5) only* dot. For the *FM(5)/FI(20)* dot, the maximal h_{dip}^z is 60 mT . So, the perpendicular field which would get picked up by the read head from the dot with the thickest FI-layer, is less than half of the field from the single phase dot. However, the fields from the dots are large enough to be detected by modern read heads [52, p. 13] [79]. As learned when investigating the effect of FI-layer thickness on the switching field in Section 5.2.3, a ferrimagnetic layer as thick as 20 nm will probably not be necessary to reduce the switching field sufficiently (see Figure 5.8).

5.6 Summary

A micromagnetic model for the simulation of exchange coupled ferri-/ferromagnetic bilayer dots was presented in Section 5.1. A series of simulations has been performed with this model to investigate the magnetization reversal of cylindrical dots with a soft ferrimagnetic FeGd(20 nm) layer and a hard ferromagnetic FePt(5 nm) layer. In order to get a switching field distribution, for each parameter set the model meshes were generated anew with randomized microstructure and anisotropic properties.

With decreasing dot diameter, from 120 nm to 5 nm, an increase in the switching field was observed because below a certain diameter the reversal mode changes from the multi-domain regime to a single domain regime. The increase of switching field comes with a broadening of the switching field distribution, since smaller diameters imply fewer grains in the hard ferromagnetic phase. Dots with small diameters exhibit homogeneous switching behavior, only interrupted when in the ferrimagnet a domain wall close to the exchange coupled interface is created and is slowly pushed towards it. Dots with larger diameters reverse more heterogeneously, building an in-plane orientation configuration and show a lateral domain wall movement in the hard magnetic phase.

The switching field and its distribution can also be controlled by the exchange coupling strength at the interface. With increasing exchange coupling, from $J_{ix} = 0$ to 5 mJ/m^2 , the ferromagnetic switching field is reduced by 30 % for 5 nm dots and 40 % for 120 nm dots. The switching field distribution is improved to a relative standard deviation of 7 % for 5 nm dots and 2 % for 120 nm dots. A significant reduction of switching field distribution can already be achieved with a relatively low interface exchange coupling strength of $J_{ix} = 2 \text{ mJ/m}^2$.

The reversal mode of bilayer dots can be influenced by varying the thickness of the soft magnetic FI-layer. For thin FI-layers the reversal happens very homogeneously, in the sense that the soft layer follows tightly the hard layer. This greatly reduces the switching field, in the case of a 20 nm diameter dot by 40 %. With increasing thickness of the FI-layer the reversal gets more inhomogeneous since a domain wall can be formed in the soft layer. After this change in reversal mode, the reduction of switching field slows down significantly when the FI-layer thickness is further increased.

The dot reversal investigations in Section 5.2 show, that increasing dot diameter, interface exchange coupling strength and FI-layer thickness decrease the switching field. For high density bit patterned media a small dot diameter is needed, which implies a higher switching field. Relatively small values of FI-layer thickness ($t_{FI} = 5 \text{ nm}$) and interface exchange coupling ($J_{ix} = 2 \text{ mJ/m}^2$) can significantly reduce the switching field, for a dot with 20 nm diameter by already more than 20%. The switching field distribution increases with decreasing dot diameter and decreases with increasing interface exchange coupling strength and FI-layer thickness.

The intrinsic switching field contribution stemming from anisotropy properties and microstructural variations is computed for three dot designs: A single layer dot of hard-magnetic FePt of 5 nm thickness, a bilayer with FePt(5 nm)/FeGd(5 nm) and a bilayer with a thicker ferrimagnet FePt(5 nm)/FeGd(20 nm). Adding a 20 nm thick FI-layer reduces the standard deviation of the switching field distribution by 59%, a 5 nm thick FI-layer still shows a 34% reduction. A correction function for all three dot designs was calculated to reflect the dependency of the switching field on the angle of the applied field and compared to the Stoner-Wolfarth correction function. While the single layer dot shows an angular dependency of the switching field close to the Stoner-Wolfarth model, the bilayer dots are less affected by a tilted applied field. At low angles the switching field of a bilayer is not as much reduced, and at higher angles $> 60^\circ$ it even increases.

The dipolar interaction field contribution was simulated in quadratic and triangular patterned 11×11 dot arrays of the three dot designs. In the denser triangular pattern, representing a $\sim 1.4 \text{ Tb/in}^2$ medium, the dipolar field acting on a dot has a standard deviation between 40 mT and 49 mT. With increasing FI-layer thickness and angle of the applied field the standard deviation increases.

A method is proposed to compute the media bit error rate (BER) incorporating the intrinsic switching field and the dipolar field contribution and also the angle of the writing field. The results show, that the angular correction function greatly affects the bit error rate but is less pronounced with increasing FI-layer thickness. Since the dipolar field in the denser triangular patterned array is higher, the head field required to switch the dots is higher than in the quadratic patterned array to reach the same bit error rate. In order to reach a bit error rate of 10^{-6} , dots with an exchange coupled FI-layer do not require such a high head field. With increasing FI-layer thickness, the influence of the dipolar field gets more relevant since the intrinsic standard deviation decreases. For an array with FePt(5 nm)/FeGd(20 nm) dots, the two contributions equally affect the bit error rate.

Adding an exchange coupled ferrimagnetic (FI) soft layer decreases the switching field and its distribution significantly. This also greatly reduces the bit error rate of bit patterned media. Both the switching field and its distribution decrease with increasing thickness of the ferrimagnetic soft layer, especially up to a thickness which then allows the formation of a domain wall. But with increasing thickness of the FI layer and increasing areal density the influence of the dipolar interaction field becomes more important and has to be taken into account.

The effect of redeposited material at the dot sidewalls during the fabrication process of patterned arrays was investigated by simulation. Using estimated properties for the redeposition based on SEM images, it was revealed, that a redeposition thickness of 4 nm can reduce the switching field of a FePt(5 nm)/FeGd(5 nm) dot by 60%. This huge impact suggests, that the properties of the redeposition have to be taken into

account when designing dots for a specific switching field range. To ensure a low switching field distribution, the redeposition has to be as uniform as possible across the array.

Irregularly shaped dots, observed in SEM images of fabricated dot arrays, were modeled and simulated. While there is no clear trend for an increase or decrease of the switching field of dots with rough edges, the switching field distribution increases with increasing roughness. The worst simulated case was a dot with a diameter of 20 nm and a maximal deviation of ± 5 nm from the radius of a perfectly circular dot. Here the resulting standard deviation of the switching field distribution was only 1.7% of the circular dots switching field. With increasing diameter the standard deviation is in the order of a few permil. These low values suggest, that dot edge roughness can be neglected in most cases.

The read back field was calculated 6 nm above the bilayer dots where the read head would be positioned. Dots with a 20 nm thick FeGd-layer on top of the FePt-layer will emit above its center only half of the field a pure FePt-layer would.

Conclusion and Outlook

Contents

6.1	Conclusion.....	107
6.2	Outlook.....	108

6.1 Conclusion

In this thesis

- a finite element model for amorphous ferrimagnets is developed, implemented and validated;
- the computed domain patterns qualitatively match those of amorphous ferrimagnets obtained in experiments;
- the model is extended by an exchange coupled ferromagnet and used to simulate the magnetization reversal of ferri-/ferromagnetic multi-layers;
- the reversal and the domain wall movement within the multi-layers are numerically visualized and the determining processes exposed;
- a new model for bit error rate of bit patterned media is developed which takes into account both the strength and the direction of the magnetostatic interaction field;
- the bit error rate of simulated ferri-/ferromagnetic bilayer dot media is computed as a function of key design parameters;

6.2 Outlook

While the comparison of the simulations results with real experiments from project partners look very promising, more can certainly be done to improve the micromagnetic model. One assumption of the ferrimagnetic model is a very strong antiparallel coupling between the magnetic moments of the sublattices. It would be of much interest to understand for which conditions this assumption is indeed sufficient to replicate real magnetic behavior, especially at elevated temperatures. Atomistic simulation methods could be used to deepen the understanding of inter-lattice phenomena.

Atomistic simulations could also help to gain better input parameters for the micromagnetic simulations [152, 31, 155]. In this thesis the input parameters are derived from and fitted to experiments which often only allow indirect approximations of magnetic input properties. A next step could be to perform atomistic simulations at the interface between a ferri- and a ferromagnetic layer to gain a better insight into the spatial distribution of magnetic properties close to the interface.

A major asset of ferrimagnetic material in exchange coupled composites is the possibility to tune the magnetic properties by composition and also exploit their thermal compensation point. In terms of magnetic recording it is necessary to investigate the ferrimagnetic behavior in micromagnetic simulations including rapid heating and cooling of the medium. In heat assisted magnetic recording bits are addressed for writing by the intersection of the magnetic write field with a heat spot. By careful design of the magnetic write field profile single islands can be addressed [66]. With regard to heat assisted magnetic recording, the exchange coupled ferrimagnetic soft layer should be designed to be at its compensation point, exerting no dipolar interaction field. Only bilayer islands irradiated by the laser heat spot will have a reduced switching field. Moreover, these dots will only experience the interaction field of the neighboring hard phase of the dots. By using this scheme, the advantage of exchange spring media can be exploited while keeping the magnetostatic interaction field low. The media bit error rate calculation proposed in this thesis can be used to find the optimal thickness of the ferrimagnetic layer for certain parameters of head field, head field angle and a desired bit error rate.

List of Figures

2.1	Angular and magnetic moments of an electron.....	6
2.2	Ferro- and Ferrimagnetic lattice.....	11
2.3	Uniaxial magnetocrystalline energy density.....	16
2.4	Motion terms of the Landau-Lifshitz-Gilbert equation.....	19
2.5	Tetrahedral finite element.....	20
2.6	Dependence of the demagnetization curve on the mesh size.....	22
2.7	Domain wall motion for different mesh sizes.....	22
2.8	Hysteresis loop of a magnet.....	24
2.9	Stoner-Wohlfarth particle.....	25
2.10	Angular dependence of Stoner-Wohlfarth nucleation.....	26
2.11	Nucleation field depending on particle size.....	28
2.12	Bloch and Néel domain wall.....	29
2.13	Domain wall pinning.....	31
2.14	Magnetic hard disk drive (HDD).....	32
3.1	Substitution of the magnetic moments of sublattices in ferrimagnetic thin films.....	36
3.2	Geometric model for a ferrimagnet.....	40
3.3	Fresnel images and simulations of remanent states for Permalloy and FeGd.....	42
3.4	Measured and simulated vortex core movement in ferrimagnetic elements.....	45
3.5	Domain patterns during vortex core movement in a ferrimagnetic element.....	46
3.6	Domain pattern in large ferrimagnetic squares.....	47
3.7	Domain wall movement in a ferrimagnetic film.....	49
3.8	Pinning events on the demagnetization curve of a ferrimagnetic layer....	50
4.1	Model of a ferri-/ferromagnetic bilayer system.....	54
4.2	Reversal curves of a ferri-/ferromagnetic bilayer.....	56
4.3	Averaged magnetization reversal curve of a ferri-/ferromagnetic bilayer.....	58
4.4	Minor reversal curves of a ferri-/ferromagnetic bilayer.....	58

4.5	Pinning sites in ferri-/ferromagnetic bilayer.	59
4.6	Cone angle and anisotropy constant distribution in magnetization reversal.	61
4.7	Magnetization reversal by domain wall pinning.	63
5.1	Geometric model for a bilayer dot.	67
5.2	Reversal curves of dot arrays.	69
5.3	Examples of reversal curves for different dot diameters.	70
5.4	Magnetization reversal of a dot (5 nm diameter).	72
5.5	Magnetization reversal of a dot (120 nm diameter).	72
5.6	Switching field depending on diameter and interface exchange coupling.	73
5.7	Switching field standard deviation of bilayer dots.	74
5.8	Switching field of bilayer dots depending on FI-layer thickness.	76
5.9	Reversal curves of dots depending on diameter and FI-thickness.	78
5.10	Magnetization configuration of bilayer dots during magnetization reversal, depending on diameter and soft layer thickness.	78
5.11	Switching field of bilayer dots depending on layer thickness and coupling strength.	80
5.12	Dot designs for investigating switching field distribution.	81
5.13	Intrinsic switching field distribution of BPM dots.	83
5.14	Correction functions for angular variation of switching field.	84
5.15	Model to determine the dipolar interaction field.	86
5.16	Distribution of dipolar interaction field.	87
5.17	Magnitude vs. angle of dipolar interaction field.	88
5.18	Standard deviation of total effective field depending on the head field angle.	89
5.19	Schematic of bit error rate calculation.	92
5.20	Bit error rate for different bit patterned media.	93
5.21	Influence of dipolar field on the bit error rate.	95
5.22	Fabricated bilayer dots.	98
5.23	Effect of redeposition at dot sidewalls.	99
5.24	Switching field distribution due to dot edge roughness.	100
5.25	Calculated stray field above different dot designs.	103

List of Tables

3.1	Properties for continuous Permalloy and ferrimagnetic element.	43
3.2	Properties of ferrimagnetic layer at $T = 70$ K investigated in [130].	48
4.1	Properties of ferri-/ferromagnetic heterostructure at $T = 70$ K investigated in [130].	56
5.1	Properties of the FM/FI-bilayer islands for reversal investigation.	68
5.2	Properties of the FM/FI-bilayer islands fitted to experiments.	75
5.3	Standard deviation depending on the head field angle	90
5.4	Switching field distribution and bit error rate of bit patterned media.	96
5.5	Standard deviation and maximal deviations of irregular shaped dots.	102

List of Symbols

- a* Distance between two spins in a cubic lattice. 14, 15, 55
- A* Area of a 2D-object. 40
- A_x Exchange stiffness constant. 14, 15, 18, 27, 28, 29, 30, 37, 41, 43, 48, 55, 60, 66, 67, 68, 75, 76, 77, 85, 98
- B** Magnetic field, Magnetic flux density. 7, 17, 19, 38
- \hbar Reduced Plank constant, $\hbar \approx 1.055 \times 10^{-34}$ Js. 6
- c* Angular correction factor for write head field. 82, 84, 83, 84, 89
- d* Diameter of circular dots in bit patterned media. 67, 70, 73, 74, 75, 76, 77, 79, 81, 97, 98, 100, 101, 102
- D* Demagnetization factor. 24, 25
- d_{coherent} Critical diameter of a sphere to change from coherent reversal to curling reversal. 27
- d_{single} Critical diameter of a sphere to change from single to multidomain regime. 28
- e* Charge of an electron. 5, 7
- E** Electric field. 38
- E_{ani} Magnetocrystalline anisotropy energy. 14, 15
- E_{dmag} Demagnetizing energy or dipolar interaction energy. 14, 16
- E_{ext} Zeeman energy. 14, 17
- E_{ix} Interface exchange energy. 54, 55, 66
- E_{tot} Gibbs free energy. 14, 18

E_x Exchange coupling energy. 14

f_0 Attempt frequency. 27

\mathbf{F}_L Lorentz force. 38

g_i Grains of a ferromagnetic material. 66, 114

g_L Landé factor. 6

H Magnetic field strength. 7, 35, 36

$H_{90\%}$ Required field to magnetize a sample to 90% of its saturation magnetization M_s . 61, 62

H_{ani} Magnitude of anisotropy field. 10, 25, 26

\mathbf{H}_{ani} Anisotropy field. 36, 37, 54

H_c Coercive field. 23, 26, 28, 30

\mathbf{H}_{dmag} Demagnetizing field or stray field. 16, 17, 18, 36, 37, 54

h_{dip} Component of the dipolar interaction field. 86, 88, 102, 103

\mathbf{H}_{dip} Dipolar interaction field. 85, 86, 88, 89, 91, 97, 114

\mathbf{H}_{eff} Effective magnetic field. 18, 19, 18, 19, 36, 37, 54, 66

H_{ext} Magnitude of an externally applied field. 7, 21, 23, 25, 44, 49, 55, 57, 61, 62, 69, 68, 70, 69, 71, 77, 99

\mathbf{H}_{ext} Externally applied field. 17, 18, 24, 25, 30, 36, 37, 44, 48, 54, 55, 59

\mathcal{H} Heisenberg Hamiltonian for localized electrons. 9

\mathbf{H}_{head} Field of the write head to write bits onto a medium. 82, 83, 84, 89, 92, 94, 96, 114

H_{head}^* Field of the write head scaled by angular correction factor. 82, 83, 84, 91, 92, 94, 95

\mathbf{H}_{ix} Interface exchange field. 53, 54, 66

H_n Nucleation field. 25, 26, 27, 28, 30, 76

H_p Pinning field. 49, 60, 76, 77

- H_{sw} Switching field. 69, 73, 74, 75, 82, 91, 98, 99, 100, 101
- $H_{\text{sw},i}^{\Delta}$ Difference between the switching field of an irregularly shaped dot and a perfectly circular dot with the same volume. 101, 114
- $H_{\text{sw,max}}^{\Delta}$ Maximum of the switching field deviations $H_{\text{sw},i}^{\Delta}$ caused by rough dot edges. 101
- \bar{H}_{sw} Mean switching field. 73, 74, 73, 74, 75, 76, 79, 82, 86, 91, 92, 96
- $\bar{H}_{\text{sw}}^{\Delta}$ Mean of the switching field differences $H_{\text{sw},i}^{\Delta}$. 101
- $H_{\text{sw},i}^{\text{f}}$ Switching field of an irregularly shaped dot. 101
- \mathbf{H}_{tot} The total field is the sum of the write head field \mathbf{H}_{head} and the dipolar interaction field \mathbf{H}_{dip} . 89, 118
- H_{tot}^* The total effective field is the sum of the head field and the dipolar field, scaled by a correction factor for angular dependence of the dots switching field. 89, 91, 92, 114
- \bar{H}_{tot}^* Mean total effective field H_{tot}^* . 91, 92
- \mathbf{H}_{x} Exchange field. 36, 37, 54
- \mathcal{J} Exchange integral. 9, 14, 15, 55
- \mathbf{j} Angular moment of an electron. 5
- \mathbf{J} Total angular moment of a multi-electron system. 6, 7
- J_{ix} Interface exchange coupling strength. 55, 57, 66, 69, 71, 73, 71, 74, 75, 79, 82, 104
- J_{s} Magnetic saturation polarization. 7, 16, 17, 18, 28, 30, 41, 43, 48, 55, 60, 66, 67, 68, 75, 76, 77, 85, 98
- \mathbf{k} Unit vector of an anisotropic easy axis. 15, 18, 24, 25, 37, 39, 53, 74
- K_2 Magnetocrystalline anisotropy constant of 2nd order. 9, 15
- k_{B} Boltzmann constant, $k_{\text{B}} \approx 1.38 \times 10^{-23}$ J/K. 27, 82
- \mathbf{k}_i Unit vector of anisotropic easy axis of a patch p_i or a grain g_i . 39, 40, 53, 66
- K_{u} Uniaxial magnetocrystalline anisotropy constant. 9, 10, 15, 18, 25, 27, 28, 29, 30, 37, 39, 48, 49, 60, 62, 74, 76, 85

$K_{u,i}$ Uniaxial magnetocrystalline anisotropy constant of a patch p_i or grain g_i . 39, 48, 49, 53, 66

\bar{K}_u Mean of the assigned uniaxial magnetocrystalline anisotropy constants. 41, 43, 48, 55, 60, 61, 62, 66, 68, 75

l Orbital moment of an electron. 5

L Sublattice of a ferrimagnetic material. 35, 36

l_c Characteristic length of a magnetic material. 21, 68

m Unit vector of a magnetic moment. 13, 14, 15, 16, 17, 18, 35, 36, 37, 55, 66

M Macroscopic magnetic moment. 7, 13, 16, 17, 18, 19, 24, 25, 30, 35, 36, 37, 54, 66, 115

M Magnitude of the magnetic moment. 7, 21, 23, 35, 36, 37, 49

m_e Mass of an electron. 5, 6, 7

m_l Magnetic moment due to orbital moment. 5

m_{tot} Total magnetic moment. 6, 7, 17

M_r Remanent magnetization. 7, 23, 69

m_s Magnetic moment due to spin moment. 5

M_s Saturation magnetization. 7, 10, 13, 18, 19, 21, 23, 24, 25, 27, 28, 44, 49, 55, 57, 61, 62, 69, 70, 69, 70, 77, 113

M_y y-component of the magnetic moment **M**. 44

M_z z-component of the magnetic moment **M**. 23, 55, 57, 61, 62, 69, 70, 73, 77, 82, 99

n Unit normal vector of a surface. 17

n Number of simulation runs. 73

N Number of atoms per unit volume. 7

n_c Number of atoms per unit cell. 14, 15

n_p Number of patches in a ferrimagnetic model. 40, 67

p_i Patches of a ferrimagnetic material. 39, 40, 53, 66, 67, 114

$p_{\text{err}}^{\text{int}}$ Bit error rate calculated from the intrinsic switching field distribution of bit patterned media dots. 91, 92, 94, 95, 96, 95, 96, 97

p_{sw} Probability to switch a dot. 91

$p_{\text{err}}^{\text{tot}}$ Bit error rate calculated from the intrinsic switching field distribution of bit patterned media dots also considering the dipolar interaction field distribution. 92, 94, 95, 96, 95, 96, 97

q Charge of an electron. 38

s Spin moment of an electron. 5, 6

\bar{s} Average approximated grain or patch size. 40, 41, 43, 48, 55, 66, 67, 68, 75

S Spin quantum number. 14, 55

t Time. 18, 19, 35

T Temperature. 27, 47, 48, 55, 82, 111

t_{FI} thickness of the ferrimagnetic layer. 67, 69, 75, 76, 77, 79, 81, 82, 84, 94, 95, 96, 95, 98, 104

t_{FM} thickness of the ferromagnetic layer. 69, 75, 76, 77, 81, 98, 100

t_{r} thickness of redeposition at dot sidewalls. 98, 99

v Velocity. 38

V Volume of an object. 27, 40, 67, 100, 101

\bar{V} Mean volume of a number of objects. 40

α Damping parameter. 19, 20, 35, 36

α_{eff} Effective damping parameter. 36, 48, 68

χ Magnetic susceptibility. 7

δ_{BW} Width of a Bloch type domain wall. 21, 29

δ_{NW} Width of a Néel type domain wall. 21, 29, 30

δ_{r} Dot edge roughness defined by the maximal deviation from the ideal dot radius. 100, 101

δ Width of domain wall. 75, 77
 ϵ_{ani} Anisotropy energy density. 9, 15, 25
 ϵ_{tot} Gibb's free energy density. 25
 γ Gyromagnetic ratio. 7, 18, 19, 35, 36
 Γ Interface between layers. 53, 54, 55, 66, 70
 γ_{BW} Domain wall energy per unit wall area. 29
 γ_{eff} Effective gyromagnetic ratio. 36
 λ Phenomenological Landau-Lifshitz damping constant. 18, 19, 20
 \mathbf{m}_e Magnetic moment of an electron. 5
 μ_{B} Bohr magneton, $\mu_{\text{B}} \approx 9.274 \times 10^{-24} \text{ A/m}^2$. 6
 μ_0 Permeability of vacuum: $4\pi \times 10^{-7} \text{ Vs/(Am)}$. 7, 10, 16, 17, 19, 21, 23, 24, 25, 27, 28, 30, 44, 49, 54, 55, 57, 61, 62, 66, 69, 70, 69, 73, 75, 77, 79, 82, 86, 88, 94, 96, 102
 Ω^{FI} Ferrimagnetic layer. 53, 54, 55, 59, 61, 66, 67, 69, 71, 70, 73, 75
 Ω^{FM} Ferromagnetic layer. 53, 54, 55, 59, 61, 66, 69, 71, 70, 73, 75
 ϕ Scalar potential. 16, 17
 $\varphi_{i,j}$ Angle between two neighboring spins i and j . 14
 ρ Magnetic volume charge. 17
 σ Magnetic surface charge. 17
 σ_{dip} Standard deviation of the dipolar interaction field distribution. 85, 86, 87, 90, 96, 95, 101
 σ_{int} Standard deviation of the intrinsic switching field distribution. 73, 74, 73, 74, 75, 82, 91, 92, 96, 95, 101
 σ_K Relative standard deviation of magnetocrystalline anisotropy constant. 40, 41, 43, 48, 55, 60, 61, 60, 61, 62, 68, 75
 σ_r Standard deviation of the switching field due to dot edge roughness. 101
 σ_{tot} Standard deviation of the total effective field distribution. 89, 90, 91, 92, 96, 95

- τ Life time of a magnetic state. 27
- θ Deviation angle between magnetization direction and anisotropic easy axis. 9, 15, 24, 25
- θ_{dip} Deviation angle between film normal and dipolar interaction field. 88
- θ_{h} Deviation angle between anisotropic easy axis and applied field. 24, 25, 26, 25, 26, 82, 84, 83, 84, 89, 92, 94, 96, 95, 96, 97
- θ_{max} Maximum deviation angle between film normal and anisotropic easy axis. 40, 41, 43, 48, 55, 60, 61, 60, 61, 62, 66, 68, 75
- θ_{tot} Deviation angle between anisotropic easy axis (film normal) and total field \mathbf{H}_{tot} . 89

Bibliography

- [1] C. Abert. *magnum.fe*. SuessCo KG. URL: www.micromagnetics.org. Last visited on 5/04/2018.
- [2] A. Aharoni. *Introduction to the Theory of Ferromagnetism*. 2nd ed. Oxford, New York: Oxford University Press, Sept. 2007.
- [3] M. Albrecht, C. T. Rettner, A. Moser, M. E. Best, and B. D. Terris. „Recording performance of high-density patterned perpendicular magnetic media“. In: *Applied Physics Letters* 81.15 (2002), p. 2875. DOI: [10.1063/1.1512946](https://doi.org/10.1063/1.1512946).
- [4] T. R. Albrecht, H. Arora, V. Ayanoor-Vitikkate, J.-M. Beaujour, D. Bedau, D. Berman, A. L. Bogdanov, Y.-A. Chapuis, J. Cushen, E. E. Dobisz, G. Doerk, He Gao, M. Grobis, B. Gurney, W. Hanson, O. Hellwig, T. Hirano, P.-O. Jubert, D. Kercher, J. Lille, Zuwei Liu, C. M. Mate, Y. Obukhov, K. C. Patel, K. Rubin, R. Ruiz, M. Schabes, Lei Wan, D. Weller, Tsai-Wei Wu, and En Yang. „Bit-Patterned Magnetic Recording: Theory, Media Fabrication, and Recording Performance“. In: *IEEE Transactions on Magnetics* 51.5 (May 2015), pp. 1–42. DOI: [10.1109/TMAG.2015.2397880](https://doi.org/10.1109/TMAG.2015.2397880).
- [5] C. Andreas, S. Gliga, and R. Hertel. „Numerical micromagnetism of strong inhomogeneities“. In: *Journal of Magnetism and Magnetic Materials* 362 (Aug. 2014), pp. 7–13. DOI: [10.1016/j.jmmm.2014.02.097](https://doi.org/10.1016/j.jmmm.2014.02.097). arXiv: [arXiv:1402.1142](https://arxiv.org/abs/1402.1142).
- [6] J. N. Armstrong, S. Z. Hua, and H. D. Chopra. „Cooperative motion of domain walls in magnetic multilayers“. In: *Physical Review B* 83.5 (Feb. 2011), p. 054426. DOI: [10.1103/PhysRevB.83.054426](https://doi.org/10.1103/PhysRevB.83.054426).
- [7] *ASTC Technology Roadmap*. URL: <http://idema.org/wp-content/plugins/download-monitor/download.php?id=2456>. Last visited on 17/07/2018.
- [8] U. Atxitia, P. Nieves, and O. Chubykalo-Fesenko. „Landau-Lifshitz-Bloch equation for ferrimagnetic materials“. In: *Physical Review B* 86.10 (Sept. 2012), p. 104414. DOI: [10.1103/PhysRevB.86.104414](https://doi.org/10.1103/PhysRevB.86.104414). arXiv: [1206.6672](https://arxiv.org/abs/1206.6672).
- [9] L. Bañas, A. Prohl, and M. Slodička. „Modeling of Thermally Assisted Magneto-dynamics“. In: *SIAM Journal on Numerical Analysis* 47.1 (Jan. 2009), pp. 551–574. DOI: [10.1137/070694995](https://doi.org/10.1137/070694995).

- [10] S. Bance, H. Oezelt, T. Schrefl, M. Winklhofer, G. Hrkac, G. Zimanyi, O. Gutfleisch, R. F. L. Evans, R. W. Chantrell, T. Shoji, M. Yano, N. Sakuma, A. Kato, and A. Manabe. „High energy product in Battenberg structured magnets“. In: *Applied Physics Letters* 105.19 (Nov. 2014), p. 192401. DOI: [10.1063/1.4897645](https://doi.org/10.1063/1.4897645).
- [11] G. Bertero, G. Guo, S. Dahandeh, and A. Krishnan. „Hard Disk Drives: Fundamentals and Perspectives“. In: *Ultra-High-Density Magnetic Recording*. Ed. by G. Varvaro and F. Casoli. 1st ed. Vol. 1. New York: Pan Stanford, 2016. Chap. 2, pp. 51–131.
- [12] S. Blundell. *Magnetism in Condensed Matter*. New York: Oxford University Press, 2001.
- [13] W. F. Brown. „Micromagnetics, Domains, and Resonance“. In: *Journal of Applied Physics* 30.4 (1959), S62–S69. DOI: [10.1063/1.2185970](https://doi.org/10.1063/1.2185970).
- [14] F. Casoli, F. Albertini, L. Nasi, S. Fabbri, R. Cabassi, F. Bolzoni, and C. Bocchi. „Strong coercivity reduction in perpendicular FePt/Fe bilayers due to hard/soft coupling“. In: *Applied Physics Letters* 92.14 (2008), p. 142506. DOI: [10.1063/1.2905294](https://doi.org/10.1063/1.2905294).
- [15] F. Casoli, L. Nasi, F. Albertini, and P. Lupo. „Exchange-Coupled Composite Media“. In: *Ultrahigh-Density Magnetic Recording. Storage Materials and Media Designs*. Ed. by G. Varvaro and F. Casoli. 1st ed. Vol. 1. New York: Pan Stanford, 2016. Chap. 6, pp. 279–326.
- [16] J. M. D. Coey. *Magnetism and Magnetic Materials*. Cambridge: Cambridge University Press, 2010. DOI: [10.1017/CBO9780511845000](https://doi.org/10.1017/CBO9780511845000).
- [17] M. Cordano, D. Tang, J. George, B. Collins, and J. Zhu. *Technology of the Future. Western Digital Announces MAMR for Next Generation HDDs*. Western Digital Corporation. Oct. 2017. URL: <https://www.youtube.com/watch?v=6iEOGxF7gLk>. Last visited on 30/04/2018.
- [18] J. Daval and B. Bechevet. „Rare earth transition metal alloys for magneto-optical recording“. In: *Journal of Magnetism and Magnetic Materials* 129.1 (Jan. 1994), pp. 98–107. DOI: [10.1016/0304-8853\(94\)90434-0](https://doi.org/10.1016/0304-8853(94)90434-0).
- [19] J. Dean, M. A. Bashir, A. Goncharov, G. Hrkac, S. Bance, T. Schrefl, A. Cazacu, M. Gubbins, R. W. Lamberton, and D. Suess. „Thermally induced adjacent track erasure in exchange spring media“. In: *Applied Physics Letters* 92.14 (2008), p. 142505. DOI: [10.1063/1.2905292](https://doi.org/10.1063/1.2905292).
- [20] J. Dean, A. Kovacs, A. Kohn, A. Goncharov, M. A. Bashir, G. Hrkac, D. A. Allwood, and T. Schrefl. „Exchange bias interactions in polycrystalline/amorphous bilayers“. In: *Applied Physics Letters* 96.7 (2010), p. 072504. DOI: [10.1063/1.3294637](https://doi.org/10.1063/1.3294637).

- [21] C. Dietrich, R. Hertel, M. Huber, D. Weiss, R. Schäfer, and J. Zweck. „Influence of perpendicular magnetic fields on the domain structure of permalloy microstructures grown on thin membranes“. In: *Physical Review B - Condensed Matter and Materials Physics* 77.17 (May 2008), p. 174427. DOI: [10.1103/PhysRevB.77.174427](https://doi.org/10.1103/PhysRevB.77.174427).
- [22] R. Dittrich, T. Schrefl, D. Suess, W. Scholz, H. Forster, and J. Fidler. „A path method for finding energy barriers and minimum energy paths in complex micromagnetic systems“. In: *Journal of Magnetism and Magnetic Materials* 250 (Sept. 2002), pp. 12–19. DOI: [10.1016/S0304-8853\(02\)00388-8](https://doi.org/10.1016/S0304-8853(02)00388-8).
- [23] M. J. Donahue. „A variational approach to exchange energy calculations in micromagnetics“. In: *Journal of Applied Physics* 83.11 (1998), p. 6491. DOI: [10.1063/1.367690](https://doi.org/10.1063/1.367690).
- [24] M. J. Donahue and R. D. McMichael. „Exchange energy representations in computational micromagnetics“. In: *Physica B: Condensed Matter* 233.4 (June 1997), pp. 272–278. DOI: [10.1016/S0921-4526\(97\)00310-4](https://doi.org/10.1016/S0921-4526(97)00310-4).
- [25] M. J. Donahue and D. G. Porter. *The Object Oriented MicroMagnetic Framework project (OOMMF)*. National Institute of Standards and Technology, Gaithersburg, US. URL: <https://math.nist.gov/oommf>. Last visited on 5/04/2018.
- [26] Y. Dong and R. H. Victora. „Micromagnetic Specification for Bit Patterned Recording at 4 Tbit/in²“. In: *IEEE Transactions on Magnetics* 47.10 (Oct. 2011), pp. 2652–2655. DOI: [10.1109/TMAG.2011.2148112](https://doi.org/10.1109/TMAG.2011.2148112).
- [27] Y. Dong and R. H. Victora. „Micromagnetic Study of Medium Noise Plateau“. In: *IEEE Transactions on Magnetics* 45.10 (Oct. 2009), pp. 3714–3717. DOI: [10.1109/TMAG.2009.2025258](https://doi.org/10.1109/TMAG.2009.2025258).
- [28] D. A. Dunavant. „High degree efficient symmetrical Gaussian quadrature rules for the triangle“. In: *International Journal for Numerical Methods in Engineering* 21.6 (June 1985), pp. 1129–1148. DOI: [10.1002/nme.1620210612](https://doi.org/10.1002/nme.1620210612).
- [29] J. W. Eaton, D. Bateman, S. Hauberg, and R. Wehbring. *GNU Octave version 4.2.0 manual: a high-level interactive language for numerical computations*. 2016. URL: www.gnu.org/software/octave/doc/interpreter.
- [30] A. Einstein. „Experimenteller Nachweis der Ampéreschen Molekularströme“. In: *Die Naturwissenschaften* 3.19 (May 1915), pp. 237–238. DOI: [10.1007/BF01546392](https://doi.org/10.1007/BF01546392).
- [31] R. F. L. Evans, W. J. Fan, P. Chureemart, T. A. Ostler, M. O. A. Ellis, and R. W. Chantrell. „Atomistic spin model simulations of magnetic nanomaterials“. In: *Journal of Physics: Condensed Matter* 26.10 (Mar. 2014), p. 103202. DOI: [10.1088/0953-8984/26/10/103202](https://doi.org/10.1088/0953-8984/26/10/103202). arXiv: [1310.6143](https://arxiv.org/abs/1310.6143).

- [32] R. F. L. Evans, T. A. Ostler, R. W. Chantrell, I. Radu, and T. Rasing. „Ultrafast thermally induced magnetic switching in synthetic ferrimagnets“. In: *Applied Physics Letters* 104.8 (Feb. 2014), p. 082410. DOI: [10.1063/1.4867015](https://doi.org/10.1063/1.4867015).
- [33] H. Fangohr, T. Fischbacher, and M. Franchin. *Nmag micromagnetic simulation package*. University of Southampton, UK. URL: <http://nmag.soton.ac.uk>. Last visited on 5/04/2018.
- [34] J. Fidler, R. Chantrell, T. Schrefl, and M. Wongsam. „Micromagnetics: Basic Principles“. In: *Encyclopedia of Materials: Science and Technology*. Ed. by K. J. Buschow, R. W. Cahn, M. C. Flemings, B. Ilschner, E. J. Kramer, S. Mahajan, and P. Veysière. 2nd ed. Oxford: Elsevier, 2001, pp. 5642–5650. DOI: [10.1016/B0-08-043152-6/00984-0](https://doi.org/10.1016/B0-08-043152-6/00984-0).
- [35] J. Fidler and T. Schrefl. „Micromagnetic modelling - the current state of the art“. In: *Journal of Physics D: Applied Physics* 33.15 (Aug. 2000), R135–R156. DOI: [10.1088/0022-3727/33/15/201](https://doi.org/10.1088/0022-3727/33/15/201).
- [36] H. Fu, R. Giles, and M. Mansuripur. „Coercivity mechanisms in magneto-optical recording media“. In: *Computers in Physics* 8.1 (1994), p. 80. DOI: [10.1063/1.168516](https://doi.org/10.1063/1.168516).
- [37] E. E. Fullerton, J. S. Jiang, M. Grimsditch, C. H. Sowers, and S. D. Bader. „Exchange-spring behavior in epitaxial hard/soft magnetic bilayers“. In: *Physical Review B* 58.18 (Nov. 1998), pp. 12193–12200. DOI: [10.1103/PhysRevB.58.12193](https://doi.org/10.1103/PhysRevB.58.12193).
- [38] J. M. García, A. Thiaville, J. Miltat, K. J. Kirk, J. N. Chapman, and F. Alouges. „Quantitative interpretation of magnetic force microscopy images from soft patterned elements“. In: *Applied Physics Letters* 79.5 (July 2001), pp. 656–658. DOI: [10.1063/1.1389512](https://doi.org/10.1063/1.1389512).
- [39] C. Geuzaine and J.-F. Remacle. „Gmsh: A 3-D finite element mesh generator with built-in pre- and post-processing facilities“. In: *International Journal for Numerical Methods in Engineering* 79.11 (Sept. 2009), pp. 1309–1331. DOI: [10.1002/nme.2579](https://doi.org/10.1002/nme.2579).
- [40] T. L. Gilbert. „A Lagrangian formulation of the gyromagnetic equation of the magnetization field“. In: *Physical Review* 100 (1955), p. 1243.
- [41] R. Giles and M. Mansuripur. „Dynamics of magnetization reversal in amorphous films of rare earth-transition metal alloys“. In: *Journal of the Magnetism Society of Japan* 15.S1 (1991), pp. 299–306. DOI: [10.3379/jmsjmag.15.S1_299](https://doi.org/10.3379/jmsjmag.15.S1_299).
- [42] R. Giles and M. Mansuripur. „Possible sources of coercivity in thin films of amorphous rare earth-transition metal alloys“. In: *Computers in Physics* 5.2 (1991), p. 204. DOI: [10.1063/1.168409](https://doi.org/10.1063/1.168409).

- [43] *GIMP: GNU Image Manipulation Program – The Free & Open Source Image Editor*. URL: www.gimp.org. Last visited on 14/02/2018.
- [44] C.-K. Goh, Z.-M. Yuan, and B. Liu. „Magnetization reversal in enclosed composite pattern media structure“. In: *Journal of Applied Physics* 105.8 (Apr. 2009), p. 083920. DOI: [10.1063/1.3109243](https://doi.org/10.1063/1.3109243).
- [45] O. Gomonay, T. Jungwirth, and J. Sinova. „Concepts of antiferromagnetic spintronics“. In: *Physica Status Solidi - Rapid Research Letters* 11.4 (Jan. 2017), pp. 1–8. DOI: [10.1002/pssr.201700022](https://doi.org/10.1002/pssr.201700022). arXiv: [1701.06556](https://arxiv.org/abs/1701.06556).
- [46] A. Goncharov, T. Schrefl, G. Hrkac, J. Dean, S. Bance, D. Suess, O. Ertl, F. Dorfbauer, and J. Fidler. „Recording simulations on graded media for area densities of up to 1 Tbit/in²“. In: *Applied Physics Letters* 91.22 (2007), p. 222502. DOI: [10.1063/1.2804609](https://doi.org/10.1063/1.2804609).
- [47] S. J. Greaves, Y. Kanai, and H. Muraoka. „Magnetic Recording in Patterned Media at 5-10 Tb/in²“. In: *IEEE Transactions on Magnetics* 44.11 (Nov. 2008), pp. 3430–3433. DOI: [10.1109/TMAG.2008.2002365](https://doi.org/10.1109/TMAG.2008.2002365).
- [48] O. Gutfleisch, M. A. Willard, E. Brück, C. H. Chen, S. G. Sankar, and J. P. Liu. „Magnetic Materials and Devices for the 21st Century: Stronger, Lighter, and More Energy Efficient“. In: *Advanced Materials* 23.7 (Feb. 2011), pp. 821–842. DOI: [10.1002/adma.201002180](https://doi.org/10.1002/adma.201002180).
- [49] F. B. Hagedorn. „Analysis of exchange-coupled magnetic thin films“. In: *Journal of Applied Physics* 41.6 (1970), pp. 2491–2502. DOI: [10.1063/1.1659251](https://doi.org/10.1063/1.1659251).
- [50] R. A. Hajjar, T. H. Wu, and M. Mansuripur. „Measurement of anisotropy energy for magneto-optical media“. In: *Journal of Applied Physics* 71.2 (Jan. 1992), pp. 813–820. DOI: [10.1063/1.351299](https://doi.org/10.1063/1.351299).
- [51] T. Hauet, E. Dobisz, S. Florez, J. Park, B. Lengsfeld, B. D. Terris, and O. Hellwig. „Role of reversal incoherency in reducing switching field and switching field distribution of exchange coupled composite bit patterned media“. In: *Applied Physics Letters* 95.26 (Dec. 2009), p. 262504. DOI: [10.1063/1.3276911](https://doi.org/10.1063/1.3276911).
- [52] J. Heidmann and A. M. Taratorin. „Magnetic Recording Heads“. In: *Handbook of Magnetic Materials*. Ed. by K. H. J. Buschow. 1st ed. Vol. 19. Amsterdam, Oxford: Elsevier, 2011. Chap. 1, pp. 1–105. DOI: [10.1016/B978-0-444-53780-5.00001-6](https://doi.org/10.1016/B978-0-444-53780-5.00001-6).
- [53] O. Hellwig, A. Berger, T. Thomson, E. Dobisz, Z. Z. Bandic, H. Yang, D. S. Kercher, and E. E. Fullerton. „Separating dipolar broadening from the intrinsic switching field distribution in perpendicular patterned media“. In: *Applied Physics Letters* 90.16 (2007), p. 162516. DOI: [10.1063/1.2730744](https://doi.org/10.1063/1.2730744).

- [54] R. Hertel, O. Fruchart, S. Cherifi, P.-O. Jubert, S. Heun, A. Locatelli, and J. Kirschner. „Three-dimensional magnetic-flux-closure patterns in mesoscopic Fe islands“. In: *Physical Review B* 72.21 (Dec. 2005), p. 214409. DOI: [10.1103/PhysRevB.72.214409](https://doi.org/10.1103/PhysRevB.72.214409). arXiv: [0507119](https://arxiv.org/abs/0507119).
- [55] L. J. Heyderman, S. Czekaj, F. Nolting, E. Müller, P. Fischer, P. Gasser, and L. López-Díaz. „Photoemission electron microscopy study of remanent magnetic domain states in ferromagnetic wedge films deposited on substrates with micrometer-sized square plateaus“. In: *Journal of Applied Physics* 99.6 (2006), p. 063904. DOI: [10.1063/1.2174119](https://doi.org/10.1063/1.2174119).
- [56] S. Hirose, M. Nishino, and S. Miyashita. „Perspectives for high-performance permanent magnets: applications, coercivity, and new materials“. In: *Advances in Natural Sciences: Nanoscience and Nanotechnology* 8.1 (Mar. 2017), p. 013002. DOI: [10.1088/2043-6254/aa597c](https://doi.org/10.1088/2043-6254/aa597c).
- [57] *Inkscape: Open Source Scalable Vector Graphics Editor*. URL: www.inkscape.org. Last visited on 14/02/2018.
- [58] D. Jenkins, W. Clegg, J. Windmill, S. Edmund, P. Davey, D. Newman, C. D. Wright, M. Loze, M. Armand, R. Atkinson, B. Hendren, and P. Nutter. „Advanced optical and magneto-optical recording techniques: a review“. In: *Microsystem Technologies* 10.1 (Dec. 2003), pp. 66–75. DOI: [10.1007/s00542-003-0307-x](https://doi.org/10.1007/s00542-003-0307-x).
- [59] A. Kikitsu. „Prospects for bit patterned media for high-density magnetic recording“. In: *Journal of Magnetism and Magnetic Materials* 321.6 (Mar. 2009), pp. 526–530. DOI: [10.1016/j.jmmm.2008.05.039](https://doi.org/10.1016/j.jmmm.2008.05.039).
- [60] A. V. Kimel, A. Kirilyuk, P. A. Usachev, R. V. Pisarev, A. M. Balbashov, and T. Rasing. „Ultrafast non-thermal control of magnetization by instantaneous photomagnetic pulses.“ In: *Nature* 435.7042 (June 2005), pp. 655–657. DOI: [10.1038/nature03564](https://doi.org/10.1038/nature03564).
- [61] A. Kirilyuk, A. V. Kimel, and T. Rasing. „Ultrafast optical manipulation of magnetic order“. In: *Reviews of Modern Physics* 82.3 (Sept. 2010), pp. 2731–2784. DOI: [10.1103/RevModPhys.82.2731](https://doi.org/10.1103/RevModPhys.82.2731).
- [62] K. J. Kirk, J. N. Chapman, and C. D. W. Wilkinson. „Lorentz microscopy of small magnetic structures (invited)“. In: *Journal of Applied Physics* 85.8 (Apr. 1999), pp. 5237–5242. DOI: [10.1063/1.369955](https://doi.org/10.1063/1.369955).
- [63] E. F. Kneller and R. Hawig. „The exchange-spring magnet: a new material principle for permanent magnets“. In: *IEEE Transactions on Magnetics* 27.4 (July 1991), pp. 3588–3560. DOI: [10.1109/20.102931](https://doi.org/10.1109/20.102931).
- [64] T. R. Koehler. „Hybrid FEM-BEM method for fast micromagnetic calculations“. In: *Physica B: Condensed Matter* 233.4 (June 1997), pp. 302–307. DOI: [10.1016/S0921-4526\(97\)00314-1](https://doi.org/10.1016/S0921-4526(97)00314-1).

- [65] T. Kosub, M. Kopte, R. Hühne, P. Appel, B. Shields, P. Maletinsky, R. Hübner, M. O. Liedke, J. Fassbender, O. G. Schmidt, and D. Makarov. „Purely antiferromagnetic magnetoelectric random access memory“. In: *Nature Communications* 8 (Jan. 2017), p. 13985. DOI: [10.1038/ncomms13985](https://doi.org/10.1038/ncomms13985). arXiv: [1611.07027](https://arxiv.org/abs/1611.07027).
- [66] A. Kovacs, H. Oezelt, M. E. Schabes, and T. Schrefl. „Numerical optimization of writer and media for bit patterned magnetic recording“. In: *Journal of Applied Physics* 120.1 (July 2016), p. 013902. DOI: [10.1063/1.4954888](https://doi.org/10.1063/1.4954888). arXiv: [1603.09493](https://arxiv.org/abs/1603.09493).
- [67] A. Kovacs, J. Fischbacher, H. Oezelt, T. Schrefl, A. Kaidatzis, R. Salikhov, M. Farle, G. Giannopoulos, and D. Niarchos. „Micromagnetic Simulations for Coercivity Improvement Through Nano-Structuring of Rare-Earth-Free L1 0-FeNi Magnets“. In: *IEEE Transactions on Magnetism* 53.11 (Nov. 2017), pp. 1–5. DOI: [10.1109/TMAG.2017.2701418](https://doi.org/10.1109/TMAG.2017.2701418). arXiv: [1703.03684](https://arxiv.org/abs/1703.03684).
- [68] P. Krone, D. Makarov, T. Schrefl, and M. Albrecht. „Correlation of magnetic anisotropy distributions in layered exchange coupled composite bit patterned media“. In: *Journal of Applied Physics* 109.10 (2011), p. 103901. DOI: [10.1063/1.3583653](https://doi.org/10.1063/1.3583653).
- [69] P. Krone, D. Makarov, T. Schrefl, and M. Albrecht. „Exchange coupled composite bit patterned media“. In: *Applied Physics Letters* 97.8 (2010), p. 082501. DOI: [10.1063/1.3481668](https://doi.org/10.1063/1.3481668).
- [70] H. Kronmüller and D. Goll. „Micromagnetic theory of the pinning of domain walls at phase boundaries“. In: *Physica B: Condensed Matter* 319.1-4 (July 2002), pp. 3–10. DOI: [10.1016/S0921-4526\(02\)01113-4](https://doi.org/10.1016/S0921-4526(02)01113-4).
- [71] H. Kronmüller and H. R. Hilzinger. „Incoherent nucleation of reversed domains in Co₅Sm permanent magnets“. In: *Journal of Magnetism and Magnetic Materials* 2.1-3 (Dec. 1975), pp. 3–10. DOI: [10.1016/0304-8853\(75\)90097-9](https://doi.org/10.1016/0304-8853(75)90097-9).
- [72] H. Kronmüller and M. Fähnle. *Micromagnetism and the Microstructure of Ferromagnetic Solids*. 1st ed. Cambridge: Cambridge University Press, 2003, p. 448.
- [73] M. H. Kryder. „Magneto-optic recording technology“. In: *Journal of Applied Physics* 57.8 (1985), p. 3913. DOI: [10.1063/1.334915](https://doi.org/10.1063/1.334915).
- [74] M. Kryder, E. Gage, T. McDaniel, W. Challener, R. Rottmayer, Ganping Ju, Yiao-Tee Hsia, and M. Erden. „Heat Assisted Magnetic Recording“. In: *Proceedings of the IEEE* 96.11 (Nov. 2008), pp. 1810–1835. DOI: [10.1109/JPROC.2008.2004315](https://doi.org/10.1109/JPROC.2008.2004315).
- [75] M. Lakshmanan. „The fascinating world of the Landau-Lifshitz-Gilbert equation: an overview“. In: *Philosophical Transactions of the Royal Society A: Mathematical, Physical and Engineering Sciences* 369.1939 (Mar. 2011), pp. 1280–1300. DOI: [10.1098/rsta.2010.0319](https://doi.org/10.1098/rsta.2010.0319). arXiv: [1101.1005](https://arxiv.org/abs/1101.1005).

- [76] L. D. Landau and L. M. Lifshitz. „On the theory of the dispersion of magnetic permeability in ferromagnetic bodies“. In: *Physikalische Zeitschrift der Sowjetunion* 8 (1935), p. 153.
- [77] J. W. Lau, M. Beleggia, and Y. Zhu. „Common reversal mechanisms and correlation between transient domain states and field sweep rate in patterned Permalloy structures“. In: *Journal of Applied Physics* 102.4 (2007), p. 043906. DOI: [10.1063/1.2769779](https://doi.org/10.1063/1.2769779).
- [78] J. Lee, C. Brombacher, J. Fidler, B. Dymerska, D. Suess, and M. Albrecht. „Contribution of the easy axis orientation, anisotropy distribution and dot size on the switching field distribution of bit patterned media“. In: *Applied Physics Letters* 99.6 (2011), p. 062505. DOI: [10.1063/1.3623752](https://doi.org/10.1063/1.3623752).
- [79] D. Litvinov and S. Khizroev. „Perpendicular magnetic recording: Playback“. In: *Journal of Applied Physics* 97.7 (Apr. 2005), p. 071101. DOI: [10.1063/1.1880449](https://doi.org/10.1063/1.1880449).
- [80] A. Lyberatos. „Switching speed limitations in perpendicular magnetic recording media“. In: *Journal of Applied Physics* 93.10 (May 2003), pp. 6199–6207. DOI: [10.1063/1.1567801](https://doi.org/10.1063/1.1567801).
- [81] D. Makarov, J. Lee, C. Brombacher, C. Schubert, M. Fuger, D. Suess, J. Fidler, and M. Albrecht. „Perpendicular FePt-based exchange-coupled composite media“. In: *Applied Physics Letters* 96.6 (Feb. 2010), p. 062501. DOI: [10.1063/1.3309417](https://doi.org/10.1063/1.3309417).
- [82] J. C. Mallinson. „On damped gyromagnetic precession“. In: *IEEE Transactions on Magnetics* 23.4 (July 1987), pp. 2003–2004. DOI: [10.1109/TMAG.1987.1065181](https://doi.org/10.1109/TMAG.1987.1065181).
- [83] S. Mangin, F. Montaigne, and A. Schuhl. „Interface domain wall and exchange bias phenomena in ferrimagnetic/ferrimagnetic bilayers“. In: *Physical Review B* 68.14 (Oct. 2003), p. 140404. DOI: [10.1103/PhysRevB.68.140404](https://doi.org/10.1103/PhysRevB.68.140404).
- [84] M. Mansuripur. „Magnetization reversal dynamics in the media of magneto-optical recording“. In: *Journal of Applied Physics* 63.12 (1988), p. 5809. DOI: [10.1063/1.340320](https://doi.org/10.1063/1.340320).
- [85] M. Mansuripur. *The Physical Principles of Magneto-optical Recording*. Cambridge: Cambridge University Press, 1995. DOI: [10.1017/CBO9780511622472](https://doi.org/10.1017/CBO9780511622472).
- [86] M. Mansuripur and R. Giles. „Demagnetizing field computation for dynamic simulation of the magnetization reversal process“. In: *IEEE Transactions on Magnetics* 24.6 (1988), pp. 2326–2328. DOI: [10.1109/20.92100](https://doi.org/10.1109/20.92100).
- [87] M. Mansuripur and R. Giles. „Simulation of the magnetization-reversal dynamics on the Connection Machine“. In: *Computers in Physics* 4.3 (1990), p. 291. DOI: [10.1063/1.168369](https://doi.org/10.1063/1.168369).

- [88] M. Mansuripur, R. Giles, and G. Patterson. „Coercivity of domain-wall motion in thin films of amorphous rare-earth–transition-metal alloys“. In: *Journal of Applied Physics* 69.8 (1991), p. 4844. DOI: [10.1063/1.348250](https://doi.org/10.1063/1.348250).
- [89] Y. Marechal, G. Meunier, J. Coulomb, and H. Magnin. „A general purpose tool for restoring inter-element continuity“. In: *IEEE Transactions on Magnetics* 28.2 (Mar. 1992), pp. 1728–1731. DOI: [10.1109/20.124037](https://doi.org/10.1109/20.124037).
- [90] D. C. Mattis. *The Theory of Magnetism Made Simple. An Introduction to Physical Concepts and to Some Useful Mathematical Methods*. World Scientific Publishing Co. Pte. Ltd., Mar. 2006. DOI: [10.1142/5372](https://doi.org/10.1142/5372).
- [91] W. H. Meiklejohn and C. P. Bean. „New Magnetic Anisotropy“. In: *Physical Review* 105.3 (Feb. 1957), pp. 904–913. DOI: [10.1103/PhysRev.105.904](https://doi.org/10.1103/PhysRev.105.904). arXiv: [arXiv:1011.1669v3](https://arxiv.org/abs/1011.1669v3).
- [92] C. Mellor. *Western Dig’s MAMR is so phat, it’ll store 100TB on a hard drive by 2032. Using microwaves to fry bits into submission*. The Register. Oct. 2017. URL: https://www.theregister.co.uk/2017/10/12/wdc_mamr_tech. Last visited on 26/04/2018.
- [93] Y. Mimura, N. Imamura, T. Kobayashi, A. Okada, and Y. Kushiro. „Magnetic properties of amorphous alloy films of Fe with Gd, Tb, Dy, Ho, or Er“. In: *Journal of Applied Physics* 49.3 (1978), p. 1208. DOI: [10.1063/1.325008](https://doi.org/10.1063/1.325008).
- [94] K. Mitsuzuka, T. Shimatsu, H. Muraoka, H. Aoi, N. Kikuchi, and O. Kitakami. „Magnetic properties of Co-Pt/Co hard/soft stacked dot arrays“. In: *Journal of Applied Physics* 103.7 (Apr. 2008), p. 07C504. DOI: [10.1063/1.2833308](https://doi.org/10.1063/1.2833308).
- [95] P. Mohn. *Magnetism in the Solid State*. Ed. by M. Cardona, P. Fulde, K. von Klitzing, H.-J. Queisser, R. Merlin, and H. Störmer. 2nd ed. Heidelberg: Springer, 2006.
- [96] H. Muraoka and S. J. Greaves. „Statistical Modeling of Write Error Rates in Bit Patterned Media for 10Tb/in² Recording“. In: *IEEE Transactions on Magnetics* 47.1 (Jan. 2011), pp. 26–34. DOI: [10.1109/TMAG.2010.2080354](https://doi.org/10.1109/TMAG.2010.2080354).
- [97] H. Muraoka, S. J. Greaves, and Y. Kanai. „Modeling and Simulation of the Writing Process on Bit-Patterned Perpendicular Media“. In: *IEEE Transactions on Magnetics* 44.11 (Nov. 2008), pp. 3423–3429. DOI: [10.1109/TMAG.2008.2001654](https://doi.org/10.1109/TMAG.2008.2001654).
- [98] O. Muthsam, C. Vogler, and D. Suess. „Noise reduction in heat-assisted magnetic recording of bit-patterned media by optimizing a high/low T_c bilayer structure“. In: *Journal of Applied Physics* 122.21 (Dec. 2017), p. 213903. DOI: [10.1063/1.5004244](https://doi.org/10.1063/1.5004244).

- [99] P. Nieves, U. Atxitia, R. W. Chantrell, and O. Chubykalo-Fesenko. „The classical two-sublattice Landau–Lifshitz–Bloch equation for all temperatures“. In: *Low Temperature Physics* 41.9 (Sept. 2015), pp. 739–744. DOI: [10.1063/1.4930973](https://doi.org/10.1063/1.4930973).
- [100] J. Nogués and I. K. Schuller. „Exchange bias“. In: *Journal of Magnetism and Magnetic Materials* 192.2 (Feb. 1999), pp. 203–232. DOI: [10.1016/S0304-8853\(98\)00266-2](https://doi.org/10.1016/S0304-8853(98)00266-2).
- [101] H. Oezelt, E. Kirk, P. Wohlhüter, E. Müller, L. J. Heyderman, A. Kovacs, and T. Schrefl. „Vortex motion in amorphous ferrimagnetic thin film elements“. In: *AIP Advances* 7.5 (May 2017), p. 056001. DOI: [10.1063/1.4973295](https://doi.org/10.1063/1.4973295).
- [102] H. Oezelt, A. Kovacs, J. Fischbacher, P. Matthes, E. Kirk, P. Wohlhüter, L. J. Heyderman, M. Albrecht, and T. Schrefl. „Switching field distribution of exchange coupled ferri-/ferromagnetic composite bit patterned media“. In: *Journal of Applied Physics* 120.9 (Sept. 2016), p. 093904. DOI: [10.1063/1.4962213](https://doi.org/10.1063/1.4962213). arXiv: [1606.01874](https://arxiv.org/abs/1606.01874).
- [103] H. Oezelt, A. Kovacs, F. Reichel, J. Fischbacher, S. Bance, M. Gusenbauer, C. Schubert, M. Albrecht, and T. Schrefl. „Micromagnetic simulation of exchange coupled ferri-/ferromagnetic heterostructures“. In: *Journal of Magnetism and Magnetic Materials* 381 (May 2015), pp. 28–33. DOI: [10.1016/j.jmmm.2014.12.045](https://doi.org/10.1016/j.jmmm.2014.12.045).
- [104] H. Oezelt, A. Kovacs, P. Wohlhüter, E. Kirk, D. Nissen, P. Matthes, L. J. Heyderman, M. Albrecht, and T. Schrefl. „Micromagnetic simulation of exchange coupled ferri-/ferromagnetic composite in bit patterned media“. In: *Journal of Applied Physics* 117.17 (May 2015), 17E501. DOI: [10.1063/1.4906288](https://doi.org/10.1063/1.4906288). arXiv: [1604.01180](https://arxiv.org/abs/1604.01180).
- [105] R. C. O’Handley. *Modern Magnetic Materials - Principles and Applications*. 1st ed. New York: John Wiley & Sons, Inc., 1999, p. 768.
- [106] T. A. Ostler, J. Barker, R. F. L. Evans, R. W. Chantrell, U. Atxitia, O. Chubykalo-Fesenko, S. El Moussaoui, L. Le Guyader, E. Mengotti, L. J. Heyderman, F. Nolting, A. Tsukamoto, A. Itoh, D. Afanasiev, B. A. Ivanov, A. M. Kalashnikova, K. Vahaplar, J. Mentink, A. Kirilyuk, T. Rasing, and A. V. Kimel. „Ultrafast heating as a sufficient stimulus for magnetization reversal in a ferrimagnet“. In: *Nature Communications* 3.1 (Jan. 2012), p. 666. DOI: [10.1038/ncomms1666](https://doi.org/10.1038/ncomms1666). arXiv: [arXiv:1011.1669](https://arxiv.org/abs/1011.1669).
- [107] J. O. Oti. „A micromagnetic model of dual-layer magnetic-recording thin films“. In: *IEEE Transactions on Magnetics* 29.2 (Mar. 1993), pp. 1265–1275. DOI: [10.1109/20.250631](https://doi.org/10.1109/20.250631).
- [108] *ParaView: an open-source, multi-platform data analysis and visualization application*. Kitware Inc. URL: www.paraview.org. Last visited on 14/02/2018.

- [109] C. Peng, S. K. Lee, and S. G. Kim. „Computer simulation of thermomagnetic recording process in exchange-coupled magneto-optical bilayer films“. In: *IEEE Transactions on Magnetics* 31.6 (1995), pp. 3268–3270. DOI: [10.1109/20.490345](https://doi.org/10.1109/20.490345).
- [110] B. Pfau, C. M. Günther, E. Guehrs, T. Hauet, T. Hennen, S. Eisebitt, and O. Hellwig. „Influence of stray fields on the switching field distribution for bit patterned media based on pre-patterned substrates“. In: *Applied Physics Letters* 105.13 (Sept. 2014), p. 132407. DOI: [10.1063/1.4896982](https://doi.org/10.1063/1.4896982).
- [111] B. Pfau, C. M. Günther, E. Guehrs, T. Hauet, H. Yang, L. Vinh, X. Xu, D. Yaney, R. Rick, S. Eisebitt, and O. Hellwig. „Origin of magnetic switching field distribution in bit patterned media based on pre-patterned substrates“. In: *Applied Physics Letters* 99.6 (2011), p. 062502. DOI: [10.1063/1.3623488](https://doi.org/10.1063/1.3623488).
- [112] S. Piramanayagam and K. Srinivasan. „Recording media research for future hard disk drives“. In: *Journal of Magnetism and Magnetic Materials* 321.6 (Mar. 2009), pp. 485–494. DOI: [10.1016/j.jmmm.2008.05.007](https://doi.org/10.1016/j.jmmm.2008.05.007).
- [113] *Python: Interpreted High-Level Programming Language*. URL: www.python.org. Last visited on 20/03/2017.
- [114] R. Quey, P. Dawson, and F. Barbe. „Large-scale 3D random polycrystals for the finite element method: Generation, meshing and remeshing“. In: *Computer Methods in Applied Mechanics and Engineering* 200.17-20 (Apr. 2011), pp. 1729–1745. DOI: [10.1016/j.cma.2011.01.002](https://doi.org/10.1016/j.cma.2011.01.002).
- [115] I. Radu, K. Vahaplar, C. Stamm, T. Kachel, N. Pontius, H. A. Dürr, T. A. Ostler, J. Barker, R. F. L. Evans, R. W. Chantrell, A. Tsukamoto, A. Itoh, A. Kirilyuk, T. Rasing, and A. V. Kimel. „Transient ferromagnetic-like state mediating ultrafast reversal of antiferromagnetically coupled spins“. In: *Nature* 472.7342 (Apr. 2011), pp. 205–208. DOI: [10.1038/nature09901](https://doi.org/10.1038/nature09901).
- [116] W. Rave and A. Hubert. „Magnetic ground state of a thin-film element“. In: *IEEE Transactions on Magnetics* 36.6 (Nov. 2000), pp. 3886–3899. DOI: [10.1109/20.914337](https://doi.org/10.1109/20.914337).
- [117] W. Rave, K. Ramstöck, and A. Hubert. „Corners and nucleation in micromagnetics“. In: *Journal of Magnetism and Magnetic Materials* 183.3 (Mar. 1998), pp. 329–333. DOI: [10.1016/S0304-8853\(97\)01086-X](https://doi.org/10.1016/S0304-8853(97)01086-X).
- [118] M. Re. *HAMR. The next leap forward is now*. Western Digital Corporation. URL: <https://blog.seagate.com/craftsman-ship/hamr-next-leap-forward-now>. Last visited on 30/04/2018.
- [119] V. Repain. „Magnetic interactions in dot arrays with perpendicular anisotropy“. In: *Journal of Applied Physics* 95.5 (2004), p. 2614. DOI: [10.1063/1.1645973](https://doi.org/10.1063/1.1645973).

- [120] H. J. Richter. „The transition from longitudinal to perpendicular recording“. In: *Journal of Physics D: Applied Physics* 40.9 (May 2007), R149–R177. DOI: [10.1088/0022-3727/40/9/R01](https://doi.org/10.1088/0022-3727/40/9/R01).
- [121] H. J. Richter, A. Y. Dobin, O. Heinonen, K. Z. Gao, R. J. M. v. d. Veerdonk, R. T. Lynch, J. Xue, D. Weller, P. Asselin, M. F. Erden, and R. M. Brockie. „Recording on Bit-Patterned Media at Densities of 1 Tb/in² and Beyond“. In: *IEEE Transactions on Magnetics* 42.10 (Oct. 2006), pp. 2255–2260. DOI: [10.1109/TMAG.2006.878392](https://doi.org/10.1109/TMAG.2006.878392).
- [122] H. J. Richter, A. Y. Dobin, R. T. Lynch, D. Weller, R. M. Brockie, O. Heinonen, K. Z. Gao, J. Xue, R. J. M. V. D. Veerdonk, P. Asselin, and M. F. Erden. „Recording potential of bit-patterned media“. In: *Applied Physics Letters* 88.22 (May 2006), p. 222512. DOI: [10.1063/1.2209179](https://doi.org/10.1063/1.2209179).
- [123] S. Romer, M. A. Marioni, K. Thorwarth, N. R. Joshi, C. E. Corticelli, H. J. Hug, S. Oezer, M. Parlinska-Wojtan, and H. Rohrmann. „Temperature dependence of large exchange-bias in TbFe-Co/Pt“. In: *Applied Physics Letters* 101.22 (2012), p. 222404. DOI: [10.1063/1.4767142](https://doi.org/10.1063/1.4767142).
- [124] *Salomé: The Open Source Integration Platform for Numerical Simulation*. URL: www.salome-platform.org. Last visited on 20/03/2017.
- [125] R. Sbiaa, K. O. Aung, S. N. Piramanayagam, E. Tan, and R. Law. „Patterned media with composite structure for writability at high areal recording density“. In: *Journal of Applied Physics* 105.7 (2009), p. 073904. DOI: [10.1063/1.3093699](https://doi.org/10.1063/1.3093699).
- [126] J. Schöberl. „NETGEN An advancing front 2D/3D-mesh generator based on abstract rules“. In: *Computing and Visualization in Science* 1.1 (1997), pp. 41–52. DOI: [10.1007/s007910050004](https://doi.org/10.1007/s007910050004).
- [127] T. Schrefl, T. Shoji, M. Winklhofer, H. Oezelt, M. Yano, and G. Zimanyi. „First order reversal curve studies of permanent magnets“. In: *Journal of Applied Physics* 111.7 (2012), 07A728. DOI: [10.1063/1.3678434](https://doi.org/10.1063/1.3678434).
- [128] T. Schrefl and D. Suess. *FEMME: Finite Element MicroMagnEtics*. SuessCo KG. URL: www.suessco.com/simulations. Last visited on 21/02/2018.
- [129] T. Schrefl, G. Hrkac, S. Bance, D. Suess, O. Ertl, and J. Fidler. „Numerical Methods in Micromagnetics (Finite Element Method)“. In: *Handbook of Magnetism and Advanced Magnetic Materials*. Ed. by H. Kronmüller and S. Parkin. Chichester, UK: John Wiley & Sons, Ltd, Dec. 2007, pp. 1–30. DOI: [10.1002/9780470022184.hmm203](https://doi.org/10.1002/9780470022184.hmm203).
- [130] C. Schubert, B. Hebler, H. Schletter, A. Liebig, M. Daniel, R. Abrudan, F. Radu, and M. Albrecht. „Interfacial exchange coupling in Fe-Tb/[Co/Pt] heterostructures“. In: *Physical Review B* 87.5 (Feb. 2013), p. 054415. DOI: [10.1103/PhysRevB.87.054415](https://doi.org/10.1103/PhysRevB.87.054415).

- [131] Y. Shi, P. W. Nutter, B. D. Belle, and J. J. Miles. „Error Events Due to Island Size Variations in Bit Patterned Media“. In: *IEEE Transactions on Magnetics* 46.6 (June 2010), pp. 1755–1758. DOI: [10.1109/TMAG.2010.2041047](https://doi.org/10.1109/TMAG.2010.2041047).
- [132] A. Shukh. „Writability of Perpendicular Recording Heads“. In: *IEEE Transactions on Magnetics* 40.4 (July 2004), pp. 2585–2587. DOI: [10.1109/TMAG.2004.829315](https://doi.org/10.1109/TMAG.2004.829315).
- [133] R. Skomski. *Simple Models of Magnetism*. Oxford, New York: Oxford University Press, Jan. 2008. DOI: [10.1093/acprof:oso/9780198570752.001.0001](https://doi.org/10.1093/acprof:oso/9780198570752.001.0001).
- [134] R. Skomski and J. M. D. Coey. „Giant energy product in nanostructured two-phase magnets“. In: *Physical Review B* 48.21 (Dec. 1993), pp. 15812–15816. DOI: [10.1103/PhysRevB.48.15812](https://doi.org/10.1103/PhysRevB.48.15812).
- [135] C. Stanciu, F. Hansteen, A. Kimel, A. Kirilyuk, A. Tsukamoto, A. Itoh, and T. Rasing. „All-Optical Magnetic Recording with Circularly Polarized Light“. In: *Physical Review Letters* 99.4 (July 2007), p. 047601. DOI: [10.1103/PhysRevLett.99.047601](https://doi.org/10.1103/PhysRevLett.99.047601).
- [136] E. C. Stoner and E. P. Wohlfarth. „A Mechanism of Magnetic Hysteresis in Heterogeneous Alloys“. In: *Philosophical Transactions of the Royal Society A: Mathematical, Physical and Engineering Sciences* 240.826 (May 1948), pp. 599–642. DOI: [10.1098/rsta.1948.0007](https://doi.org/10.1098/rsta.1948.0007).
- [137] D. Suess, M. Fuger, C. Abert, F. Bruckner, and C. Vogler. „Superior bit error rate and jitter due to improved switching field distribution in exchange spring magnetic recording media“. In: *Scientific Reports* 6.1 (July 2016), p. 27048. DOI: [10.1038/srep27048](https://doi.org/10.1038/srep27048). arXiv: [1510.04403](https://arxiv.org/abs/1510.04403).
- [138] D. Suess, J. Lee, J. Fidler, and T. Schrefl. „Exchange-coupled perpendicular media“. In: *Journal of Magnetism and Magnetic Materials* 321.6 (Mar. 2009), pp. 545–554. DOI: [10.1016/j.jmmm.2008.06.041](https://doi.org/10.1016/j.jmmm.2008.06.041).
- [139] D. Suess, T. Schrefl, S. Fähler, M. Kirschner, G. Hrkac, F. Dorfbauer, and J. Fidler. „Exchange spring media for perpendicular recording“. In: *Applied Physics Letters* 87.1 (2005), p. 012504. DOI: [10.1063/1.1951053](https://doi.org/10.1063/1.1951053).
- [140] D. Suess, C. Vogler, C. Abert, F. Bruckner, R. Windl, L. Breth, and J. Fidler. „Fundamental limits in heat-assisted magnetic recording and methods to overcome it with exchange spring structures“. In: *Journal of Applied Physics* 117.16 (Apr. 2015), p. 163913. DOI: [10.1063/1.4918609](https://doi.org/10.1063/1.4918609).
- [141] D. Süß. „Micromagnetics of exchange spring media: Optimization and limits“. In: *Journal of Magnetism and Magnetic Materials* 308.2 (Jan. 2007), pp. 183–197. DOI: [10.1016/j.jmmm.2006.05.021](https://doi.org/10.1016/j.jmmm.2006.05.021).

- [142] K. M. Tako, T. Schrefl, M. A. Wongsam, and R. W. Chantrell. „Finite element micromagnetic simulations with adaptive mesh refinement“. In: *Journal of Applied Physics* 81.8 (Apr. 1997), pp. 4082–4084. DOI: [10.1063/1.365086](https://doi.org/10.1063/1.365086).
- [143] R. C. Taylor. „Magnetic properties of amorphous Gd-Fe films prepared by evaporation“. In: *Journal of Applied Physics* 47.3 (1976), p. 1164. DOI: [10.1063/1.322698](https://doi.org/10.1063/1.322698).
- [144] B. D. Terris, T. Thomson, and G. Hu. „Patterned media for future magnetic data storage“. In: *Microsystem Technologies* 13.2 (Nov. 2006), pp. 189–196. DOI: [10.1007/s00542-006-0144-9](https://doi.org/10.1007/s00542-006-0144-9).
- [145] *Texmaker: Free cross-platform LaTeX editor*. URL: www.xmlmath.net/texmaker. Last visited on 14/02/2018.
- [146] T. Thomson, G. Hu, and B. D. Terris. „Intrinsic Distribution of Magnetic Anisotropy in Thin Films Probed by Patterned Nanostructures“. In: *Physical Review Letters* 96.25 (June 2006), p. 257204. DOI: [10.1103/PhysRevLett.96.257204](https://doi.org/10.1103/PhysRevLett.96.257204).
- [147] K. Vahaplar, A. M. Kalashnikova, A. V. Kimel, D. Hinzke, U. Nowak, R. Chantrell, A. Tsukamoto, A. Itoh, A. Kirilyuk, and T. Rasing. „Ultrafast Path for Optical Magnetization Reversal via a Strongly Nonequilibrium State“. In: *Physical Review Letters* 103.11 (Sept. 2009), p. 117201. DOI: [10.1103/PhysRevLett.103.117201](https://doi.org/10.1103/PhysRevLett.103.117201).
- [148] A. Vansteenkiste. *mumax³ GPU-accelerated micromagnetism*. Dynamics of Functional Nano Materials, Ghent University, Belgium. URL: <https://mumax.github.io>. Last visited on 5/04/2018.
- [149] R. H. Victora, X. Jianhua, and M. Patwari. „Areal density limits for perpendicular magnetic recording“. In: *IEEE Transactions on Magnetics* 38.5 (Sept. 2002), pp. 1886–1891. DOI: [10.1109/TMAG.2002.802791](https://doi.org/10.1109/TMAG.2002.802791).
- [150] R. H. Victora and X. Shen. „Composite media for perpendicular magnetic recording“. In: *IEEE Transactions on Magnetics* 41.2 (Feb. 2005), pp. 537–542. DOI: [10.1109/TMAG.2004.838075](https://doi.org/10.1109/TMAG.2004.838075).
- [151] R. Victora and X. Shen. „Exchange Coupled Composite Media“. In: *Proceedings of the IEEE* 96.11 (Nov. 2008), pp. 1799–1809. DOI: [10.1109/JPROC.2008.2004314](https://doi.org/10.1109/JPROC.2008.2004314).
- [152] C. Vogler, C. Abert, F. Bruckner, and D. Suess. „Landau-Lifshitz-Bloch equation for exchange-coupled grains“. In: *Physical Review B* 90.21 (Dec. 2014), p. 214431. DOI: [10.1103/PhysRevB.90.214431](https://doi.org/10.1103/PhysRevB.90.214431). arXiv: [1410.6066](https://arxiv.org/abs/1410.6066).
- [153] C. Vogler, C. Abert, F. Bruckner, D. Suess, and D. Praetorius. „Heat-assisted magnetic recording of bit-patterned media beyond 10 Tb/in²“. In: *Applied Physics Letters* 108.10 (Mar. 2016), p. 102406. DOI: [10.1063/1.4943629](https://doi.org/10.1063/1.4943629). arXiv: [1510.02400](https://arxiv.org/abs/1510.02400).

- [154] A. Weber, E. Kirk, P. Matthes, D. Nissen, H. Oezelt, T. Schrefl, M. Albrecht, and J. L. Heyderman. *Development of technological platform for Argon ion beam etching to achieve perpendicular sidewalls*. 41st Micro and Nano Engineering Conference, The Hague, Netherlands. Poster presentation. Sept. 2015.
- [155] S. Westmoreland, R. Evans, G. Hrkac, T. Schrefl, G. Zimanyi, M. Winklhofer, N. Sakuma, M. Yano, A. Kato, T. Shoji, A. Manabe, M. Ito, and R. Chantrell. „Multiscale model approaches to the design of advanced permanent magnets“. In: *Scripta Materialia* 148 (Apr. 2018), pp. 56–62. DOI: [10.1016/j.scriptamat.2018.01.019](https://doi.org/10.1016/j.scriptamat.2018.01.019).
- [156] S. Wienholdt, D. Hinzke, K. Carva, P. M. Oppeneer, and U. Nowak. „Orbital-resolved spin model for thermal magnetization switching in rare-earth-based ferrimagnets“. In: *Physical Review B* 88.2 (July 2013), p. 020406. DOI: [10.1103/PhysRevB.88.020406](https://doi.org/10.1103/PhysRevB.88.020406).
- [157] T. Williams and C. Kelley. *gnuplot: An Interactive Plotting Program*. Version 5.0. URL: www.gnuplot.info. Last visited on 21/02/2018.
- [158] Y. Yamada, M. Yoshihiro, N. Ohta, H. Sakeda, T. Niihara, and H. Fujiwara. „Highly power sensitive and field sensitive MO disk for 8 MB/s data transfer“. In: *Journal of the Magnetics Society of Japan* 15.MORIS91 (1991), pp. 417–420. DOI: [10.3379/jmsjmag.15.S1_417](https://doi.org/10.3379/jmsjmag.15.S1_417).
- [159] J.-G. Zhu, X. Zhu, and Y. Tang. „Microwave Assisted Magnetic Recording“. In: *IEEE Transactions on Magnetics* 44.1 (Jan. 2008), pp. 125–131. DOI: [10.1109/TMAG.2007.911031](https://doi.org/10.1109/TMAG.2007.911031).

Study hard what interests you the most in the most undisciplined, irreverent and original manner possible.

— Richard P. Feynman

Ok... Well, sometimes science is more art than science, Morty.

A lot of people don't get that.

— Rick and Morty (Rick Potion #9 - Episode)

Rick, are you really a musician?

Who's not a musician, Morty?

Me!

Yeah, not with that attitude.

— Rick and Morty (Get Schwifty - Episode)

Harald Özelt

Curriculum Vitae

Department for Integrated Sensor Systems
Danube University Krems
Viktor Kaplan Str. 2E
2700 Wiener Neustadt, Austria

Tel: +43 (0)2622 23420 56
Email: harald.oezelt@donau-uni.ac.at
Web: www.donau-uni.ac.at/diss
ORCID: [0000-0002-3754-3565](https://orcid.org/0000-0002-3754-3565)

Personal

Name	Ing. Harald Özelt, MSc.
Place of birth	St. Pölten, Austria
Citizenship	Austria

Research Interests

Micromagnetic modelling, simulation and optimization

- ▶ for heat assisted magnetic recording
- ▶ for exchange coupled composite materials
- ▶ for rare-earth efficient permanent magnets

Education

02/2013–today	Doctoral candidate Vienna University of Technology, Austria. Doctoral program in technical sciences at the Institute of Solid State Physics Thesis: <i>Exchange-coupled ferri-/ferromagnetic composite nanomagnets</i>
09/2010–06/2012	Master of Science in Engineering, with distinction, University of Applied Sciences St. Pölten, Austria. Master degree course for Industrial Simulation Thesis: <i>Characterization of NdFeB permanent magnets</i>
10/2007–06/2010	Bachelor of Science in Engineering, with distinction, University of Applied Sciences St. Pölten, Austria. Bachelor degree course for Communications & Simulation Engineering Thesis: <i>First order reversal curves</i>
09/1997–06/2002	Matura (Austrian high school diploma), Federal Higher Technical Institute for Educating and Experimenting (HTBLuVA) St. Pölten, Austria. Electrical Engineering – Energy Engineering and Power Electronics

Professional Experience

07/2015–today	Research Associate , Danube University Krems, Department for Integrated Sensor Systems <i>FE-micromagnetic simulations for heat assisted magnetic recording and critical material free permanent magnets</i>
07/2012–06/2015	Research Associate , St. Pölten Univ. of Applied Sciences <i>Modelling and simulation of ferri-/ferromagnetic heterostructures</i> <i>Administration of a computer cluster</i> <i>Supervision of Bachelor student projects</i>
07/2010–08/2010	Research visit , University of California, Davis, USA <i>Setup and administration of a computer cluster</i> <i>Characterization of NdFeB magnets for hybrid cars</i>
05/2010–06/2012	Research Assistant , St. Pölten Univ. of Applied Sciences <i>Characterization and optimization of permanent magnets</i> <i>Setup of a computer cluster</i>
06/2003–09/2007	Electrical Engineer , Klenk&Meder GmbH, St. Pölten <i>Project management and execution</i>
09/2002–04/2003	Military Driver , Basic military service PZSTBB 3, St. Pölten <i>Assistance deployment at the border of Burgenland</i>

Research Projects

	Responsible for modelling activities in the following projects
01/2018–09/2019	Novel, critical materials free, high anisotropy phases for permanent magnets (Novamag EU H2020 Grant No. 686056)
01/2015–07/2018	Thermally controlled magnetization dynamics (WWTF MA14-44)
07/2012–12/2015	Novel exchange-coupled composite Nanomagnets (FWF I821)
05/2010–today	Rare-earth efficient permanent magnets (Toyota Motor Corp.)

Scientific Activities

23 Publications in peer-reviewed journals

4 Talks at International Conferences (Intermag, IEEE AIM, MMM, HMM)

3 Poster presentations at International Conferences (JEMS, MMM, Intermag)

Reviewer for Physica B: Condensed Matter and IEEE: Transactions on Magnetics

Scientific Collaborations

Simon Bance, Seagate Technology, Research and Development, United Kingdom

Laura Heyderman, PSI, Lab. for Multiscale Materials Experiments, Switzerland

Manfred Albrecht, University of Augsburg, Institute of Physics, Germany

Gino Hrkac, University of Exeter, College of Engineering, United Kingdom

Gergely Zimanyi, University of California Davis, Department of Physics, USA

Michael Winklhofer, University of Oldenburg, IBU, Germany

Akira Kato, Toyota Motor Corporation, Japan

Dirk Praetorius, Vienna UT, Inst. for Analysis a. Scientific Computing, Austria

Dieter Suess, University of Vienna, Physics of Functional Materials, Austria

Chronological list of peer-reviewed publications

- [1] L. Exl, J. Fischbacher, A. Kovacs, H. Oezelt, M. Gusenbauer, and T. Schrefl. „Preconditioned nonlinear conjugate gradient method for micromagnetic energy minimization“. In: *Computer Physics Communications* (Sept. 2018). DOI: [10.1016/j.cpc.2018.09.004](https://doi.org/10.1016/j.cpc.2018.09.004). arXiv: [1801.03690](https://arxiv.org/abs/1801.03690).
- [2] J. Fischbacher, A. Kovacs, M. Gusenbauer, H. Oezelt, L. Exl, S. Bance, and T. Schrefl. „Micromagnetics of rare-earth efficient permanent magnets“. In: *Journal of Physics D: Applied Physics* 51.19 (May 2018), p. 193002. DOI: [10.1088/1361-6463/aab7d1](https://doi.org/10.1088/1361-6463/aab7d1).
- [3] J. Fischbacher, A. Kovacs, H. Oezelt, M. Gusenbauer, T. Schrefl, L. Exl, D. Givord, N. M. Dempsey, G. Zimanyi, M. Winklhofer, G. Hrkac, R. Chantrell, N. Sakuma, M. Yano, A. Kato, T. Shoji, and A. Manabe. „On the limits of coercivity in permanent magnets“. In: *Applied Physics Letters* 111.7 (Aug. 2017), p. 072404. DOI: [10.1063/1.4999315](https://doi.org/10.1063/1.4999315). arXiv: [1708.01880](https://arxiv.org/abs/1708.01880).
- [4] J. Fischbacher, A. Kovacs, H. Oezelt, M. Gusenbauer, D. Suess, and T. Schrefl. „Effective uniaxial anisotropy in easy-plane materials through nanostructuring“. In: *Applied Physics Letters* 111.19 (Nov. 2017), p. 192407. DOI: [10.1063/1.4997816](https://doi.org/10.1063/1.4997816). arXiv: [1711.03144](https://arxiv.org/abs/1711.03144).
- [5] J. Fischbacher, A. Kovacs, H. Oezelt, T. Schrefl, L. Exl, J. Fidler, D. Suess, N. Sakuma, M. Yano, A. Kato, T. Shoji, and A. Manabe. „Nonlinear conjugate gradient methods in micromagnetics“. In: *AIP Advances* 7.4 (Apr. 2017), p. 045310. DOI: [10.1063/1.4981902](https://doi.org/10.1063/1.4981902).
- [6] A. Kovacs, J. Fischbacher, H. Oezelt, T. Schrefl, A. Kaidatzis, R. Salikhov, M. Farle, G. Giannopoulos, and D. Niarchos. „Micromagnetic Simulations for Coercivity Improvement Through Nano-Structuring of Rare-Earth-Free L1 0 -FeNi Magnets“. In: *IEEE Transactions on Magnetics* 53.11 (Nov. 2017), pp. 1–5. DOI: [10.1109/TMAG.2017.2701418](https://doi.org/10.1109/TMAG.2017.2701418). arXiv: [1703.03684](https://arxiv.org/abs/1703.03684).
- [7] H. Oezelt, E. Kirk, P. Wohlhüter, E. Müller, L. J. Heyderman, A. Kovacs, and T. Schrefl. „Vortex motion in amorphous ferrimagnetic thin film elements“. In: *AIP Advances* 7.5 (May 2017), p. 056001. DOI: [10.1063/1.4973295](https://doi.org/10.1063/1.4973295).
- [8] H. Oezelt, A. Kovacs, J. Fischbacher, S. Bance, M. Gubbins, and T. Schrefl. „Transition Jitter in Heat-Assisted Magnetic Recording by Micromagnetic Simulation“. In: *IEEE Transactions on Magnetics* 53.11 (Nov. 2017), pp. 1–5. DOI: [10.1109/TMAG.2017.2709840](https://doi.org/10.1109/TMAG.2017.2709840). arXiv: [1703.03688](https://arxiv.org/abs/1703.03688).
- [9] S. Bance, J. Fischbacher, A. Kovacs, H. Oezelt, F. Reichel, and T. Schrefl. „Thermal activation in permanent magnets“. In: *JOM* 67.6 (Mar. 2016), pp. 1350–1356. DOI: [10.1007/s11837-015-1415-7](https://doi.org/10.1007/s11837-015-1415-7). arXiv: [1603.08365](https://arxiv.org/abs/1603.08365).
- [10] S. Bance, H. Oezelt, T. Schrefl, G. Ciuta, N. M. Dempsey, D. Givord, M. Winklhofer, G. Hrkac, G. Zimanyi, O. Gutfleisch, T. G. Woodcock, T. Shoji, M. Yano, A. Kato, and A. Manabe. „Influence of defect thickness on the angular dependence of coercivity in rare-earth permanent magnets“. In: *Applied Physics Letters* 104.18 (Mar. 2016), p. 182408. DOI: [10.1063/1.4876451](https://doi.org/10.1063/1.4876451). arXiv: [1603.08248](https://arxiv.org/abs/1603.08248).

- [11] A. Kovacs, H. Oezelt, M. E. Schabes, and T. Schrefl. „Numerical optimization of writer and media for bit patterned magnetic recording“. In: *Journal of Applied Physics* 120.1 (July 2016), p. 013902. DOI: [10.1063/1.4954888](https://doi.org/10.1063/1.4954888). arXiv: [1603.09493](https://arxiv.org/abs/1603.09493).
- [12] H. Oezelt, A. Kovacs, J. Fischbacher, P. Matthes, E. Kirk, P. Wohlhüter, L. J. Heyderman, M. Albrecht, and T. Schrefl. „Switching field distribution of exchange coupled ferri-/ferromagnetic composite bit patterned media“. In: *Journal of Applied Physics* 120.9 (Sept. 2016), p. 093904. DOI: [10.1063/1.4962213](https://doi.org/10.1063/1.4962213). arXiv: [1606.01874](https://arxiv.org/abs/1606.01874).
- [13] R. Windl, F. Bruckner, C. Abert, C. Huber, C. Vogler, T. Huber, H. Oezelt, and D. Suess. „Passive wireless strain measurement based upon the Villari effect and giant magnetoresistance“. In: *Applied Physics Letters* 109.25 (Dec. 2016), p. 253502. DOI: [10.1063/1.4972399](https://doi.org/10.1063/1.4972399).
- [14] H. Oezelt, A. Kovacs, F. Reichel, J. Fischbacher, S. Bance, M. Gusenbauer, C. Schubert, M. Albrecht, and T. Schrefl. „Micromagnetic simulation of exchange coupled ferri-/ferromagnetic heterostructures“. In: *Journal of Magnetism and Magnetic Materials* 381 (May 2015), pp. 28–33. DOI: [10.1016/j.jmmm.2014.12.045](https://doi.org/10.1016/j.jmmm.2014.12.045).
- [15] H. Oezelt, A. Kovacs, P. Wohlhüter, E. Kirk, D. Nissen, P. Matthes, L. J. Heyderman, M. Albrecht, and T. Schrefl. „Micromagnetic simulation of exchange coupled ferri-/ferromagnetic composite in bit patterned media“. In: *Journal of Applied Physics* 117.17 (May 2015), 17E501. DOI: [10.1063/1.4906288](https://doi.org/10.1063/1.4906288). arXiv: [1604.01180](https://arxiv.org/abs/1604.01180).
- [16] S. Bance, H. Oezelt, T. Schrefl, M. Winklhofer, G. Hrkac, G. Zimanyi, O. Gutfleisch, R. F. L. Evans, R. W. Chantrell, T. Shoji, M. Yano, N. Sakuma, a. Kato, and a. Manabe. „High energy product in Battenberg structured magnets“. In: *Applied Physics Letters* 105.19 (Nov. 2014), p. 192401. DOI: [10.1063/1.4897645](https://doi.org/10.1063/1.4897645).
- [17] M. Gusenbauer, H. Nguyen, F. Reichel, L. Exl, S. Bance, J. Fischbacher, H. Özelt, A. Kovacs, M. Brandl, and T. Schrefl. „Guided self-assembly of magnetic beads for biomedical applications“. In: *Physica B: Condensed Matter* 435 (Feb. 2014), pp. 21–24. DOI: [10.1016/j.physb.2013.08.050](https://doi.org/10.1016/j.physb.2013.08.050).
- [18] A. Kovacs, H. Oezelt, S. Bance, J. Fischbacher, M. Gusenbauer, F. Reichel, L. Exl, T. Schrefl, and M. E. Schabes. „Numerical optimization of writer geometries for bit patterned magnetic recording“. In: *Journal of Applied Physics* 115.17 (May 2014), 17B704. DOI: [10.1063/1.4859055](https://doi.org/10.1063/1.4859055). arXiv: [1504.03577](https://arxiv.org/abs/1504.03577).
- [19] J. Fischbacher, S. Bance, L. Exl, M. Gusenbauer, H. Oezelt, F. Reichel, and T. Schrefl. „Enhanced nucleation fields due to dipolar interactions in nanocomposite magnets“. In: *The European Physical Journal B* 86.3 (Mar. 2013), p. 100. DOI: [10.1140/epjb/e2013-30938-1](https://doi.org/10.1140/epjb/e2013-30938-1).
- [20] M. Gusenbauer, H. Özelt, J. Fischbacher, F. Reichel, L. Exl, S. Bance, N. Kataeva, C. Binder, H. Brückl, and T. Schrefl. „Simulation of magnetic active polymers for versatile microfluidic devices“. In: *EPJ Web of Conferences* 40 (Jan. 2013), p. 02001. DOI: [10.1051/epjconf/20134002001](https://doi.org/10.1051/epjconf/20134002001).
- [21] F. Reichel, T. Schrefl, D. Süß, G. Hrkac, D. Praetorius, M. Gusenbauer, S. Bance, H. Özelt, J. Fischbacher, and L. Exl. „Mechanical oscillations of magnetic strips under the influence of external field“. In: *EPJ Web of Conferences* 40 (Jan. 2013), p. 13004. DOI: [10.1051/epjconf/20134013004](https://doi.org/10.1051/epjconf/20134013004).
- [22] M. Gusenbauer, A. Kovacs, F. Reichel, L. Exl, S. Bance, H. Özelt, and T. Schrefl. „Self-organizing magnetic beads for biomedical applications“. In: *Journal of Magnetism and Magnetic Materials* 324.6 (Mar. 2012), pp. 977–982. DOI: [10.1016/j.jmmm.2011.09.034](https://doi.org/10.1016/j.jmmm.2011.09.034). arXiv: [1110.0983v1](https://arxiv.org/abs/1110.0983v1).
- [23] T. Schrefl, T. Shoji, M. Winklhofer, H. Oezelt, M. Yano, and G. Zimanyi. „First order reversal curve studies of permanent magnets“. In: *Journal of Applied Physics* 111.7 (2012), 07A728. DOI: [10.1063/1.3678434](https://doi.org/10.1063/1.3678434).

